AMELOTIN AND KALLIKREIN-4 IN ENAMEL MATURATION

by

Stephanie Marie Núñez

A dissertation submitted in partial fulfillment
of the requirements for the degree of
Doctor of Philosophy
(Oral Health Sciences)
in the University of Michigan
2014

Doctoral Committee:

Professor James P. Simmer, Chair
Professor Scott E. Barolo
Professor Renny T. Franceschi
Professor Paul Krebsbach

DEDICATION

To my best friend, Andrew Strickland; my parents, Oliver and Wanda Carter; and to my mentor, Dr. Mark Pinsky.

ACKNOWLEDGEMENTS

The road in this dual D.D.S./Ph.D. program has been long, so I would like to thank all of the individuals who aided and supported me throughout my doctoral training:

Dr. Jan Hu and Dr. James Simmer served as my thesis advisors for 5 years. Their support, advice, and direction have been essential to the completion of this thesis and my growth as a scientist. For this I am very grateful.

I am grateful to the members of my committee: Dr. Paul Krebsbach, Dr. Renny Franceschi, and Dr. Scott Barolo. Their scientific insight and advice helped to better shape and color the final dissertation.

Dr. Bernhard Ganss kindly provided us with the *Amtn*-knockout/*LacZ*-knockin mice that made this project possible.

Dr. Charles Smith was an invaluable resource on all things pertaining to enamel development and experimental techniques.

Present and past members of Dr. Hu and Dr. Simmer's laboratory have been an indispensable and crucial support system for me during the completion of this program

and thesis: Dr. Yuan-Yuan Hu for her teaching, patience, and support; Dr. Yasuo Yamakoshi for being my first teacher when I entered the laboratory; Amelia Richardson for her assistance with histology and tissue processing; Bryan Reid and Soumya Pal for support with the animal colony; Andrew Samann for moral support; Dr. Shih-Kai Wang for his encouragement and for being a great classmate, office-mate, and friend; and finally Dr. Enamul Kabir, Rachel Milkovich, Rangsiyakorn Lertlam, Dr. Yuhe Lu, Dr. Yonghee Chun, Fumiko Yamakoshi, Dr. Hsun-Liang Chan, and Dr. Jie Yang for experimental support and promoting a spirited work environment that fostered intellectual progress.

The staff of the Microscopy and Imaging Laboratory core was an immense help to me for the electron microscopy and immunogold localization portion of my thesis. A special thank you to Dorothy Sorensen for training me in the immunogold protocol and the transmission electron microscope; Bruce Donohoe and Dr. Krystyna Pasyk for their assistance with thin sectioning; Jeff Harrison for training me on the scanning electron microscope; and finally Chris Edwards, Shelley Almburg, and Sasha Meshinchi for sharing their knowledge and advice.

I would also like to thank the following:

James Schmitz and Dr. Roberto Fajardo at the University of Texas, San Antonio micro-CT core assisted with the micro-CT portion of this study.

Dr. Carlos Gonzáles-Cabezas and Susan Flannagan for generously teaching me and allowing me to use their microhardness testing machine.

All past and present students from the Oral Health Sciences Ph.D. program for their friendship, company, and moral support. MOHSSA has only gotten better over time.

I am very grateful to the past and present staff of the Oral Health Sciences Research Office including Patricia Schultz, Manette London, Charlene Erickson, Kimberly Smith, Sarah Ellerholz, and Misty Gravelin, for their administrative support and kindness.

I would also like to thank faculty and staff of the Biologic and Materials Sciences Department for their support.

Dr. Rossi Irobalieva, Dr. Stephanie Munz, Dr. Andrew Clark, Dr. Andrew Dill, Dr. Mark Oldakowski, Dr. Ross Nelson, Dr. Kathryn Ritchie, Dr. Aaron Osga, Dr. Jennifer Broers, Dr. Christina Scanlon, Dr. Thomas Eyster, Amy Baek, Caitlin Holman, Sonu Mishra, and Aparna Vadlamani for their friendship and for always keeping my head in the clouds and feet on the ground.

Dr. Dennis Nelson and Luanne Nelson for being my second family during my time in Michigan.

Finally I would like to thank Andrew Strickland; my parents, Oliver and Wanda Carter; and my mentor and friend, Dr. Mark Pinsky. During all of the tough times in this

program you supported me, believed in me, and encouraged me to stick it out a little bit longer. I would not have completed this journey without you.

PREFACE

This thesis includes significant work of Drs. Jan Hu, James Simmer, Bernhard Ganss, Yuan-Yuan Hu, and James Schmitz.

Description of my contribution to the work presented in this thesis:

I wrote all of the chapters in this thesis. Drs. Jan Hu and James Simmer contributed to experimental design and thesis writing.

I wrote Chapter 1 where I summarized the hypothesis, specific aims, and background information that was relevant to the project.

Chapter 2 describes the mouse models that were used. Dr. Jan Hu obtained the approval for the Institutional Animal Care and Use Committee (IACUC) protocol at the University of Michigan that was used in this work. *Amtn*-null transgenic mice were obtained from Dr. Bernhard Ganss. Characterization of the *Klk4*-knockout/*LacZ*-knockin mice was previously published (Simmer et al. (2009), J Biol Chem, *284*, 19110-21). *Amtn*/*Klk4*- null and *Amtn*/*Klk4*-heterozygous mice were produced by me through the breeding scheme described in this chapter. Sequencing data was generated at the University of Michigan DNA Sequencing Core.

Chapter 3 describes the scanning electron microscopy that was used to study enamel ultrastructural features. I obtained all of the images presented.

In Chapter 4, mandibles were sent to the University of Texas, San Antonio micro-CT core where they were scanned and analyzed by James Schmitz and Dr. Roberto Fajardo. They were able to provide the high mineral density phantoms that were required to obtain quantitative enamel mineral density measurements. The MIP data was then compiled and further analyzed by me with ImageJ in our laboratory.

I performed all of the microhardness indentation experiments described in Chapter 5 using equipment from the laboratory of Dr. Carlos Gonzáles-Cabezas at the University of Michigan, School of Dentistry. The statistical analysis was performed with the assistance of the Center for Statistical Consultation and Research (CSCAR).

The immunogold labeling experiments described in Chapter 6 were performed by me with the assistance of Dorothy Sorensen from the University of Michigan Microscopy and Imaging Laboratory. Embedded samples were faced by me, and thin-sectioned by Bruce Donohoe and Krystyna Pasyk. All images of processed and stained samples were taken by me. Perfusions of the mice were performed by me with the assistance of Dr. Yuan-Yuan Hu, Amelia Richardson, and Sowmya Pal.

I wrote Chapter 7 where I summarized the work performed in this thesis and conclusions that were drawn from the data.

TABLE OF CONTENTS

LIST OF FIGURES

CHAPTER 2

CHAPTER 3

CHAPTER 4

ABSTRACT

AMELOTIN AND KALLIKREIN-4 IN ENAMEL MATURATION

by

Stephanie Marie Núñez

Chair: James P. Simmer

Amelotin (AMTN) and kallikrein 4 (KLK4) are secreted proteins that function during the maturation stage of amelogenesis. Knockout mice have been generated for both, and in both of these mice a *lac*Z reporter was knocked in at the translation initiation site. KLK4 has been well-characterized and is a secreted serine protease that cleaves enamel proteins, which facilitates their removal from the extracellular matrix. AMTN is specifically secreted by maturation stage ameloblasts, but its function is unknown. The objectives of this study were to characterize wild-type, *Amtn*$^{-/-}$, *Klk4*$^{-/-}$, *Amtn*$^{+/-}$*Klk4*$^{+/-}$, and *Amtn*$^{-/-}$*Klk4*$^{-/-}$ mice to gain insights into the function of AMTN during enamel formation. *Amtn*$^{-/-}$ and *Klk4*$^{-/-}$ mice were crossed to generate double heterozygotes (*Amtn*$^{+/-}$*Klk4*$^{+/-}$), which were crossed to generate double null (*Amtn*$^{-/-}$*Klk4*$^{-/-}$) mice. The *Amtn lac*Z reporter

was too weak in histochemical analyses to confirm specific *Amtn* expression. RT-PCR analyses determined that the weakness of the *lac*Z signal was due to deletion of the modified exon 2 during splicing. *Amtn*-null mice exhibited chalky-white incisors that chipped when maintained on a standard hard chow diet. No phenotype of any kind was ever detected in the double heterozygous mice. As the *Klk4*-null enamel phenotype is much more severe than that of the *Amtn*-null, in most (but not all) subsequent studies of enamel structure, the $Klk4^{-/-}$ and $Amtn^{-/-}Klk4^{-/-}$ mice were indistinguishable.

Our studies were largely conducted on cross-sections of the mandibular incisors at the level of the alveolar crest, which is ideal for several reasons: the enamel is completely formed, has not yet erupted into the oral cavity (where it can be altered) and this level can be precisely and reproducibly sampled in all mice. SEM, BEI, and μCT analyses confirmed that AMTN and KLK4 play no role during the secretory stage of amelogenesis. The enamel in all 5 genotypes had the same thickness and volume, and rod decussation pattern. Although BEI and μCT analyses could not detect any differences in mineral density between the WT and $Amtn^{-/-}$ mice, or between the $Klk4^{-/-}$ and $Amtn^{-/-}Klk4^{-/-}$ (which suggested a minimal role for AMTN in enamel maturation), μCT analyses detected a significant delay in the onset of enamel maturation in $Amtn^{-/-}$ mice, while the microhardness study proved that the outer enamel of the $Amtn^{-/-}$ mice is not as hard as that of the wild-type, and that the outer enamel of the *Amtn*/*Klk4* double null mice is not as hard as that of the *Klk4* single null. These findings demonstrated that

AMTN is necessary to achieve the final hardness of the outer enamel layer and that AMTN's contribution to enamel hardness is independent of KLK4. The results of our TEM immunogold analyses were consistent with this interpretation: there are no significant differences in the amount of residual amelogenin in the outer enamel between the WT and *Amtn*$^{-/-}$ mice, or between the *Klk4*$^{-/-}$ and *Amtn*$^{-/-}$*Klk4*$^{-/-}$. AMTN does not seem to play a role in the reabsorption of enamel proteins. We conclude that KLK4 and AMTN are both essential for optimal enamel maturation, but they likely function in separate pathways.

CHAPTER 1

INTRODUCTION

PROBLEM STATEMENT

Dental enamel is a specialized mineralized tissue that covers the crowns of teeth and gives them the durability needed to support mastication throughout life. Enamel is the hardest structure in the vertebrate body. Teeth form by developmental processes similar to those that guide the formation of other ectodermal organs. Dental enamel formation, or amelogenesis, is part of this developmental program and is accomplished by a specialized layer of epithelial cells. Failure of this process in humans leads to the disease amelogenesis imperfecta, or AI (Simmer and Hu, 2001), which is a group of inherited conditions that affect the clinical appearance and structure of the enamel layer (Witkop, 1957). This is both a problem for proper oral health and maintenance of balanced nutrition, and is a cosmetic issue that leads to problems in social acceptance as the child enters a school environment. Therefore, the goal of my research is to understand the basic mechanisms of enamel formation at a molecular level. Specifically, I am interested in understanding the function of a protein called amelotin (AMTN) that is expressed in the later stages of tooth development.

Amelogenesis is achieved by ameloblasts, whose life cycle is typically divided into two main stages. The first half is called the secretory stage where ameloblasts are actively secreting proteins into the extracellular enamel matrix (Hu et al., 2007). This process is highly regulated and is required for proper organization of mineral crystallites into thin ribbons that lengthen until the final thickness of enamel is reached. The second stage of amelogenesis is maturation, where this protein matrix is almost entirely removed and reabsorbed by ameloblasts, allowing the mineral crystallites to widen and thicken until the enamel layer reaches I ts final hardness (Hu et al., 2007).

The protein AMTN and the protease KLK4 are both specifically expressed and secreted by maturation stage ameloblasts (Moffatt et al., 2006b; Simmer et al., 2009). During the maturation stage of enamel development, removal of the proteins is enhanced by KLK4 digestion, particularly in the deeper layers of enamel. When KLK4 is missing, the erupted enamel is chalky-white, soft, and cheese-like in consistency, resulting in rapid attrition and fracture following eruption into the oral cavity (Simmer et al., 2009). As shown in this thesis, the absence of AMTN leads to superficial enamel that is chalky-white in appearance, but the enamel layer does not fracture off as easily as it does when KLK4 is missing. However, when AMTN is missing, enamel maturation is delayed and the outer enamel layer does not fully harden.

GENERAL HYPOTHESIS

Enamel proteins must be removed by ameloblasts during the maturation stage of amelogenesis. KLK4 digestion appears to assist in the cleavage and removal of enamel proteins in the deeper layers back to the surface for endocytosis, while amelotin appears to be required for allowing the surface enamel to fully harden. *We hypothesize that AMTN and KLK4 serve complementary but different functions during the maturation stage of amelogenesis that are both required for the entire enamel layer to fully harden.* Two specific aims were proposed to test this hypothesis.

SPECIFIC AIMS

SA1. Characterize enamel structural changes when KLK4 and/or AMTN are absent.

SA2. Determine if KLK4 and AMTN are both necessary for the full removal of enamel proteins.

To achieve these aims we bred *Klk4*-null and *Amtn*-null mice to obtain double heterozygous and double null mice and characterized the enamel formed by mice of 5 different genotypes: wild-type (WT; $Amtn^{+/+}Klk4^{+/+}$), amelotin null ($Amtn^{-/-}$), kallikrein 4 null ($Klk4^{-/-}$), amelotin and kallikrein 4 double heterozygous ($Amtn^{+/-}Klk4^{+/-}$), and amelotin and kallikrein 4 double null ($Amtn^{-/-}Klk4^{-/-}$). The techniques used to

characterize these mice included morphometric evaluation under a dissecting microscope, histochemistry, RT-PCR, backscatter electron imaging (BEI), scanning electron microscopy (SEM), micro computed tomography (μCT), microhardness testing, and transmission electron microscopy with immunogold labeling.

BACKGROUND AND SIGNIFICANCE

The process of enamel formation, or amelogenesis, results in the hardest mineralized tissue in the vertebrate body consisting of 95% calcium hydroxyapatite [$Ca_{10}(PO_4)_6(OH)_2$] by weight with the remaining proportion consisting of protein and water (Weatherell, 1975; Young and Spooner, 1970). Enamel crystallites are organized into interlocking bundles called rods, each rod being the product of a single ameloblast, the cell type responsible for enamel formation (Warshawsky and Nanci, 1982). This structural organization along with its high mineral content is what allows enamel to withstand extreme conditions such as large mechanical forces, temperature changes, and pH variations. In humans, however, this tissue is unable to repair itself since the ameloblasts are lost very soon after the tooth erupts (Smith and Nanci, 1995).

Amelogenesis is divided into multiple, highly regulated steps and is carried out by the epithelial derived ameloblasts. The entire process can be thought of as a balance between the deposition of mineral ions and the secretion of extracellular protein matrix

which organizes the mineral into hydroxyapatite crystallites, and the subsequent degradation and endocytosis of this protein matrix, ultimately allowing the enamel layer to reach its final hardness (Lacruz et al., 2013; Smith, 1998; Smith and Nanci, 1995). Amelogenesis begins with the secretion of a mineralization front consisting of a protein matrix that is responsible for laying down thin ribbons of crystallite (Simmer et al., 2012). The protein matrix is subsequently degraded by proteases and resorbed by ameloblasts to allow space for these crystallites to widen and thicken until they interlock with each other (Smith, 1998). This results in a unique, hard tissue structure that is integral in communication, mastication, and self-defense and is intended to last the lifetime of the organism.

Amelogenesis

Tooth development begins with a highly regulated sequence of interactions between the oral epithelium and the underlying mesenchyme resulting in an enamel organ (Ten Cate, 1959, 1996; Thesleff et al., 1995). The inner enamel organ epithelium eventually differentiates into ameloblasts, which are attached to a basement membrane under which the dentin matrix is deposited by odontoblasts. This basement membrane disintegrates as ameloblasts become polarize by developing projections called Tomes' processes that signify the initiation of secretory stage (Smith, 1998). The secretion and deposition of protein matrix at a mineralization front is critical for producing enamel

crystallites. This protein matrix is primarily composed of amelogenin (AMELX) which accounts for most of the matrix (Fincham et al., 1999), while the remaining secretory stage matrix is composed of ameloblastin (AMBN), enamelin (ENAM), and the protease matrix metalloproteinase 20 (MMP20) which immediately begins to degrade the matrix during this stage (Bartlett, 2013; Chun et al., 2010; Gasse et al., 2012; Hu et al., 2007; Hu et al., 2014; Simmer et al., 2012). These cleavage products accumulate in the enamel layer and are partly resorbed by ameloblasts at this time. Once the enamel crystallites have reached their final length, the Tomes' processes retract and ameloblasts begin to modulate between a smooth and ruffle ended morphology (Josephsen and Fejerskov, 1977), which marks their entrance into the maturation stage. At this time a basal lamina re-forms, different than the one present prior to the secretory stage, and with it is associated the protein amelotin (AMTN) (Ida-Yonemochi et al., 2005; Nanci et al., 1993; Sahlberg et al., 1998; Takano, 1979). During the maturation stage ameloblasts also secrete the protease kallikrein 4 (KLK4), which degrades the enamel matrix (Simmer et al., 2009). This process allows the enamel layer to further harden by increasing the overall mineral content and thus the final strength of the enamel layer of the tooth.

Maturation Stage

The maturation stage of amelogenesis is where final calcification and mineralization of the enamel layer occurs prior to eruption (Smith, 1998; Smith and Nanci, 1995). This

rapid volumetric expansion is mechanistically carried out by supersaturating the enamel fluid with calcium and phosphate ions to favor the deposition of mineral, provided that the surrounding extracellular protein matrix is adequately removed to free up the needed space (Lacruz et al., 2013; Lacruz et al., 2012; Nanci A, 1992; Smith, 1998). This stage is critical for achievement of adequate hardness to prevent the enamel layer from fracturing or shearing off from the underlying dentin as too high a protein content in the final product will yield in a significantly weaker structure. Fully matured enamel is composed almost entirely of the mineral hydroxyapatite crystals which are organized into rods, each of which is presumed to have been produced by a single ameloblast (Simmer et al., 2010; Simmer et al., 2012). In the spaces between rods, mineral crystals are organized into interrod enamel. Unique to rodent enamel, these rods decussate, or rather are interlinked in a cross-hatch pattern that also serves as a trail of the path traveled by each ameloblast (Kallenbach, 1973). The almost pure mineral content and final crystal organization together are what give enamel its unique strength.

The most unique aspect of the maturation stage is the cyclical and rapid morphological change in ameloblasts between what is referred to as "ruffle-ended ameloblasts" (RA) and "smooth-ended ameloblasts" (SA) (Josephsen and Fejerskov, 1977; Lacruz et al., 2013; Smith, 1998). SAs are impermeable to ion movement across the basal pole due to the presence of tight junctions, while RA tight junctions are located at

the apical pole (Reith and Boyde, 1981; Smith, 1998; Smith et al., 1987). The alternation between these two cell types happens rapidly, on the order of hours (Smith et al., 1987). This dynamic and rapid change allows for bi-directional diffusion of mineral ions into the enamel layer, and matrix peptides and amino acids out of the enamel layer (Josephsen et al., 2010; Lacruz et al., 2013; Smith, 1998). In this stage the ameloblasts do not have any significant protein synthesizing organelles such as Golgi and rough ER (Smith, 1998) but do contain a significant number of energy-providing mitochondria (Hubbard, 2000) supporting the idea that at this stage the primary function of these cells is to actively transport and shuttle ions and molecules back and forth rather than any significant synthesis of new molecules. Of importance is the active transport of calcium at this stage, a typically cytotoxic ion beyond concentrations of 0.2 μmol/L (Hubbard, 2000). Recent studies suggest that this ion is transported by a method termed "calcium transcytosis" (Hubbard et al., 2011) and helps to account for the inordinately high number of calcium binding proteins that are produced by ameloblasts.

A variety of proteins are expressed during the maturation stage of amelogenesis. Some are involved in calcium transcellular transport, such as STIM1, ORAI1, or SLC24A4 (Berna-Erro et al., 2012; Wang et al., 2014a). Others are required for magnesium removal such as CNNM4 (Luder et al., 2013) or protein matrix removal such as KLK4 (Simmer et al., 2009). More recently discovered proteins such as WDR72,

ODAM, and AMTN are still being studied to determine their exact function during the maturation stage (Holcroft and Ganss, 2011; Lee et al., 2010; Moffatt et al., 2006a).

KLK4 is a serine protease that is expressed in ameloblasts beginning in the transition stage as the basal lamina is beginning to reform, and continuing into the maturation stage (Hu et al., 2000a; Simmer et al., 1998; Simmer et al., 2009). It is part of a larger family of fifteen kallikrein genes that are encoded on human chromosome 19q13.3-q13.4 (Lu et al., 2008). Its function in the maturation stage of amelogenesis is primarily to degrade the extracellular matrix laid down during the secretory stage to allow enamel crystallites to widen and thicken (Smith, 1998). Its main substrate is amelogenin, which composes most of the extracellular enamel matrix (Fincham et al., 1999; Ryu et al., 2002), but it has also been shown to cleave enamelin remnants that are resistant to further MMP20 degradation (Yamakoshi et al., 2006) and is generally recognized to have broad target specificity (Lu et al., 2008). In the mouse, pig, and human Klk4 is composed of six exons, five of which are coding (exon 1 is non-coding) (Hu et al., 2000b) and in mouse and pig, KLK4 as three asparagine residues in the proper context for glycosylation (Ryu et al., 2002), however, recombinant protein without these glycosylations seems to retain activity (Yoon et al., 2007). In humans, defects in this gene result in autosomal recessive amelogenesis imperfect, resulting in hypomineralized enamel that is pigmented and wears down quickly, emphasizing the importance of KLK4 for enamel maturation (Hart et al., 2004; Wang et al., 2013).

In an effort to elucidate the ameloblast secretome, and thus other potential candidate proteins involved in amelogenesis, a signal-trap peptide technique was used to identify two novel proteins that were subsequently named amelotin (AMTN) and ODAM (previously known as Apin) (Moffatt et al., 2006a).

Amelotin (AMTN)

The protein AMTN, is a member of the secretory calcium binding phospho-protein (SCPP) family, a group pf proteins that stabilize solubilized calcium and phosphate ions and participate in their deposition into crystal structures (Kawasaki, 2013; Kawasaki and Weiss, 2008; Nishio et al., 2010). This group arose out of tandem gene duplications of the common ancestor SPARC-L1, and is classified based on amino acid composition (Kawasaki, 2013; Kawasaki et al., 2004). Evidence suggests that this likely occurred prior to mammalian line divergence around 310 million years ago (Sire et al., 2007). The SCPP genes share several common biochemical and structural characteristics as a group. They all contain a signal peptide which indicates that they are secreted, contain one or more Ser-X-Glu residue motifs, exon 1 and part of exon 2 contain the 5'-untranslated region, and exon 2 typically contains the signal peptide (Kawasaki et al., 2007; Kawasaki and Weiss, 2003, 2006). These features allow this group to interact with calcium, making these proteins ideal for mineralization.

The human *Amtn* gene is 12 kb in length and consists of 9 exons, and of these, exon 1 is non-coding, exon 2 encodes the highly conserved signal peptide that is 16 residues in length (Gasse et al., 2012), and exon 7 encodes a phosphorylated serine residue (Dos Santos Neves et al., 2012; Kawasaki, 2013; Moffatt et al., 2006b). It is conserved across 44 different species of mammals and lizard, but it does not appear to be present in chickens, fish, or amphibians (Kawasaki, 2011). Of the 209 residues contained in human AMTN, variation in the gene is greatest in the c-terminal region where the stop codon is located, and is mostly due to insertions or deletions in exon 8 (Gasse et al., 2012). It contains two conserved motifs of unknown function in exons 4 and 6 and conserved phosphorylation sites encoded by exon 7, as well as highly conserved intron sequences bordering exons (Gasse et al., 2012). The AMTN protein has two conserved serine phosphorylation sites (SSEE motif) in positions #115-118, which is recognized by Golgi casein kinase (Ishikawa et al., 2012; Tagliabracci et al., 2012). It is also possibly post-translationally modified with O-linked oligosaccharides (Dos Santos Neves et al., 2012; Moffatt et al., 2006b). In rat, AMTN has three alternative transcripts, the first and longest being 212 residues while transcript 2 (203 residues) is missing exon 7 (containing the phosphorylation sites at Ser115 and Ser116) and transcript 3 (111 residues) is missing exons 3-7 (Moffatt et al., 2006b).

Expression of AMTN begins in the postsecretory transition stage and continues late into the maturation stage (Moffatt et al., 2006b). Expression has also been observed

in the junctional epithelium that attaches to the tooth (Nishio et al., 2013), but not odontoblasts, pulp cells, or osteoblasts (Iwasaki et al., 2005; Moffatt et al., 2006b; Trueb et al., 2007). Specifically, immunolabeling was detected in the enamel matrix close to the basal lamina in the transition stage and it becomes stronger over the basal lamina of the maturation stage (Dos Santos Neves et al., 2012; Somogyi-Ganss et al., 2012). Using immunofluorescence, AMTN was specifically localized to the basal lamina of maturation stage ameloblasts and the internal basal lamina of the junctional epithelium (Moffatt et al., 2006b).

Structurally, the AMTN protein is similar to AMBN and ENAM (Kawasaki and Weiss, 2006). Sequence alignment of AMTN (Sire et al., 2007) indicates that three main regions are conserved within mammals. The first is the N-terminal region, which contains the signal peptide and plays a role in localizing the protein extracellularly. Secondly is the IPLT motif in exon 4 which may indicate that O-linked glycosylation of threonine is also critical (Sire et al., 2007). The final one is a conserved SSEEL motif that is a proposed CK2 serine phosphorylation site according to a previous study (Moffatt et al., 2006b). *Amtn* has been found in several different mammalian species but is absent from fish, birds, and amphibians suggesting that over time it has evolved to perform tooth specific functions (Kawasaki, 2013).

Given that AMTN contains a signal peptide, it is a secreted protein and current hypotheses suggest that it may be involved in cellular adhesion or regulation of ion and

peptide transport across the basal lamina during enamel maturation (Somogyi-Ganss et al., 2012). When the AMTN protein was transiently transfected into HEK-293 cells it was detected only in the conditioned media and not in cell extracts. This protein migrated at 37 kDa, which was greater than its predicted 21.8 kDa size. The recombinant version of the protein, however, migrated around 21.2 kDa, suggesting that AMTN is post-translationally modified in some way (Moffatt et al., 2006b). Immunolocalization experiments showed Golgi-like labeling in ameloblasts undergoing post-secretory transition. This labeling quickly disappeared and became localized in a discrete line at the interface between the enamel layer and ameloblasts during the maturation stage. Interestingly, there was no labeling at all in the enamel layer itself (Moffatt et al., 2006b). A recent study, however, showed through immunogold labeling that in the early maturation stage AMTN is seen infiltrating into the superficial enamel layer before localizing discretely to the basal lamina in the later maturation stage (Somogyi-Ganss et al., 2012).

Maturation Stage Basal Lamina

The basal lamina found in the early stages of amelogenesis is unique in that it is degraded prior to secretion by ameloblasts, and then reformed during the transition stage just before maturation by these same cells into a similar structure but with a different composition (Hu et al., 2007; Kallenbach, 1971). In the presecretory phase, this

basal lamina, which is similar to that in skin, is primarily composed of type-IV collagen, laminin 332, nidogen, and heparan sulfate proteglycan and serves as a barrier between preameloblasts and the dental pulp (Kawasaki, 2013; Kogaya et al., 1990; Nagai et al., 2001; Yoshiba et al., 1998). The basal lamina is broken down before the ameloblasts extend their Tomes' processes and enter the secretory stage, but it is subsequently reformed as ameloblasts enter the transition stage just prior to the maturation stage (Hu et al., 2007; Kawasaki, 2013). In contrast to the presecretory basal lamina, the maturation stage basal lamina is unique. It is highly glycosylated and contains laminin 332 while localization experiments have shown that type-IV collagen is not a main component (Al Kawas and Warshawsky, 2008; Nanci et al., 1993; Sahlberg et al., 1998). At this point the ameloblasts form a firm attachment to the basal lamina through hemidesmosomes and enamel crystals appear to integrate with the partially mineralized lamina densa (Kawasaki, 2013; Nanci et al., 1993; Takano, 1979). Basement membranes typically play important roles in cellular attachment, molecular filtration barriers, and signaling between cells and underlying matrix (Nanci et al., 1993) so it is possible that this maturation stage basal lamina is serving to keep ameloblasts closely associated with the underlying maturing enamel. Keeping in mind that during the maturation stage there are many dynamic changes occurring including protein loss and mineral deposition, the basal lamina may also be heavily influencing the diffusion of materials between ameloblasts and the enamel layer.

Amelogenesis Imperfecta

Understanding all of the components required for enamel formation to proceed correctly is critical for being able to understand what happens in humans when this process fails, which leads to a condition known as amelogenesis imperfect (AI). It is a genetically heterogeneous group of diseases that all ultimately result in an aberration of a normally tightly regulated process (Bartlett, 2013; Hu et al., 2007; Rao and Witkop, 1971; Witkop, 1957, 1988). Clinically, teeth are yellowish-brown in color; may be pitted or grooved; are more susceptible to caries, wear, and breaking; and have wide spacing between them (Witkop, 1957, 1988). Aside from the esthetic problems that this presents, patients are often in pain and require multiple invasive dental procedures at great expense. This group of patients often has difficulty maintaining adequate hygiene and psychologically perceive themselves as having a lower quality of life (Coffield et al., 2005).

The defective enamel affects both primary and permanent dentitions and reported phenotypes are highly variable depending on the involved gene, location and type of mutation. AI has been classified into four main categories: hypoplastic, hypocalcified, hypomaturation, and hypomaturation-hypoplastic with taurodontism (Witkop, 1957, 1988). These differences in enamel malformation are believed to reflect the timing at which the defect occurred in amelogenesis. Inheritance patterns range from X-linked, autosomal dominant, and autosomal recessive producing a total of 14

subtypes of AI with a combined prevalence of about 1:14,000 in the United States (Witkop, 1957, 1988).

Studies involving mutational analyses of candidate genes have revealed causal mutations in AMELX (Lagerstrom et al., 1991), ENAM (Rajpar et al., 2001), AMBN (Poulter et al., 2014c), MMP20 (Kim et al., 2005), FAM83H (Kim et al., 2008), ITGB6 (Poulter et al., 2014a; Wang et al., 2014b), C4orf24 (Parry et al., 2012), KLK4 (Hart et al., 2004; Wang et al., 2013), WDR72 (El-Sayed et al., 2009), SLC24A4 (Parry et al., 2013), COL17A1 (McGrath et al., 1996), and LAMB3 (Kim et al., 2013; Poulter et al., 2014b). However, in many of the known cases of AI the causative genetic defect remains unknown, which emphasizes how much unknown information remains to be discovered about the process of amelogenesis.

Summary

Amelogenesis produces the hardest known mineralized tissue, composed of over 95% mineral (Deakins M, 1941). This process is divided into two main stages, secretory and maturation, where a variety of proteins are secreted with precise timing and location to orchestrate the complex process of enamel formation. In the secretory stage an extracellular matrix is secreted that helps to organize the enamel crystallites until the full thickness of enamel is reached. This protein matrix is subsequently degraded during the maturation stage to allow these mineral crystallites to widen and thicken.

This study focuses on the maturation stage proteins AMTN and KLK4, which are both expressed by maturation stage ameloblasts (Moffatt et al., 2006b; Simmer et al., 2009). While KLK4 is responsible for cleaving the protein matrix, the exact function of AMTN is still unclear. The goal of the studies that are described in this thesis was to further elucidate the role of AMTN in amelogenesis. These studies primarily used a series of knockout mouse models to answer these questions and further improve our understanding of amelogenesis as a whole.

REFERENCES

Al Kawas, S., and Warshawsky, H. (2008). Ultrastructure and composition of basement membrane separating mature ameloblasts from enamel. Arch Oral Biol *53*, 310-317.

Bartlett, J.D. (2013). Dental Enamel Development: Proteinases and Their Enamel Matrix Substrates. ISRN Dent *2013*, 684607.

Berna-Erro, A., Woodard, G.E., and Rosado, J.A. (2012). Orais and STIMs: physiological mechanisms and disease. J Cell Mol Med *16*, 407-424.

Chun, Y.H., Lu, Y., Hu, Y., Krebsbach, P.H., Yamada, Y., Hu, J.C., and Simmer, J.P. (2010). Transgenic rescue of enamel phenotype in Ambn null mice. J Dent Res *89*, 1414-1420.

Coffield, K.D., Phillips, C., Brady, M., Roberts, M.W., Strauss, R.P., and Wright, J.T. (2005). The psychosocial impact of developmental dental defects in people with hereditary amelogenesis imperfecta. J Am Dent Assoc *136*, 620-630.

Deakins M, V.J. (1941). Amount of organic matter in enamel from several types of human teeth. J Dent Res *20*, 117-121.

Dos Santos Neves, J., Wazen, R.M., Kuroda, S., Francis Zalzal, S., Moffatt, P., and Nanci, A. (2012). Odontogenic ameloblast-associated and amelotin are novel basal lamina components. Histochem Cell Biol *137*, 329-338.

El-Sayed, W., Parry, D.A., Shore, R.C., Ahmed, M., Jafri, H., Rashid, Y., Al-Bahlani, S., Al Harasi, S., Kirkham, J., Inglehearn, C.F., *et al.* (2009). Mutations in the beta propeller WDR72 cause autosomal-recessive hypomaturation amelogenesis imperfecta. Am J Hum Genet *85*, 699-705.

Fincham, A.G., Moradian-Oldak, J., and Simmer, J.P. (1999). The structural biology of the developing dental enamel matrix. J Struct Biol *126*, 270-299.

Gasse, B., Silvent, J., and Sire, J.Y. (2012). Evolutionary analysis suggests that AMTN is enamel-specific and a candidate for AI. J Dent Res *91*, 1085-1089.

Hart, P.S., Hart, T.C., Michalec, M.D., Ryu, O.H., Simmons, D., Hong, S., and Wright, J.T. (2004). Mutation in kallikrein 4 causes autosomal recessive hypomaturation amelogenesis imperfecta. J Med Genet *41*, 545-549.

Holcroft, J., and Ganss, B. (2011). Identification of amelotin- and ODAM-interacting enamel matrix proteins using the yeast two-hybrid system. Eur J Oral Sci *119 Suppl 1*, 301-306.

Hu, J.C., Chun, Y.H., Al Hazzazzi, T., and Simmer, J.P. (2007). Enamel formation and amelogenesis imperfecta. Cells Tissues Organs *186*, 78-85.

Hu, J.C., Hu, Y., Lu, Y., Smith, C.E., Lertlam, R., Wright, J.T., Suggs, C., McKee, M.D., Beniash, E., Kabir, M.E., *et al.* (2014). Enamelin is critical for ameloblast integrity and enamel ultrastructure formation. PLoS One *9*, e89303.

Hu, J.C., Ryu, O.H., Chen, J.J., Uchida, T., Wakida, K., Murakami, C., Jiang, H., Qian, Q., Zhang, C., Ottmers, V., *et al.* (2000a). Localization of EMSP1 expression during tooth formation and cloning of mouse cDNA. J Dent Res *79*, 70-76.

Hu, J.C., Zhang, C., Sun, X., Yang, Y., Cao, X., Ryu, O., and Simmer, J.P. (2000b). Characterization of the mouse and human PRSS17 genes, their relationship to other serine proteases, and the expression of PRSS17 in developing mouse incisors. Gene *251*, 1-8.

Hubbard, M.J. (2000). Calcium transport across the dental enamel epithelium. Crit Rev Oral Biol Med *11*, 437-466.

Hubbard, M.J., McHugh, N.J., and Mangum, J.E. (2011). Exclusion of all three calbindins from a calcium-ferry role in rat enamel cells. Eur J Oral Sci *119 Suppl 1*, 112-119.

Ida-Yonemochi, H., Ohshiro, K., Swelam, W., Metwaly, H., and Saku, T. (2005). Perlecan, a basement membrane-type heparan sulfate proteoglycan, in the enamel organ: its intraepithelial localization in the stellate reticulum. J Histochem Cytochem *53*, 763-772.

Ishikawa, H.O., Xu, A., Ogura, E., Manning, G., and Irvine, K.D. (2012). The Raine syndrome protein FAM20C is a Golgi kinase that phosphorylates bio-mineralization proteins. PLoS One *7*, e42988.

Iwasaki, K., Bajenova, E., Somogyi-Ganss, E., Miller, M., Nguyen, V., Nourkeyhani, H., Gao, Y., Wendel, M., and Ganss, B. (2005). Amelotin--a Novel Secreted, Ameloblast-specific Protein. J Dent Res *84*, 1127-1132.

Josephsen, K., and Fejerskov, O. (1977). Ameloblast modulation in the maturation zone of the rat incisor enamel organ. A light and electron microscopic study. J Anat *124*, 45-70.

Josephsen, K., Takano, Y., Frische, S., Praetorius, J., Nielsen, S., Aoba, T., and Fejerskov, O. (2010). Ion transporters in secretory and cyclically modulating ameloblasts: a new hypothesis for cellular control of preeruptive enamel maturation. Am J Physiol Cell Physiol *299*, C1299-1307.

Kallenbach, E. (1971). Electron microscopy of the differentiating rat incisor ameloblast. J Ultrastruct Res *35*, 508-531.

Kallenbach, E. (1973). The fine structure of Tomes' process of rat incisor ameloblasts and its relationship to the elaboration of enamel. Tissue Cell *5*, 501-524.

Kawasaki, K. (2011). The SCPP gene family and the complexity of hard tissues in vertebrates. Cells Tissues Organs *194*, 108-112.

Kawasaki, K. (2013). Odontogenic ameloblast-associated protein (ODAM) and amelotin: Major players in hypermineralization of enamel and enameloid. J Oral Biosci *55*, 80-85.

Kawasaki, K., Buchanan, A.V., and Weiss, K.M. (2007). Gene duplication and the evolution of vertebrate skeletal mineralization. Cells Tissues Organs *186*, 7-24.

Kawasaki, K., Suzuki, T., and Weiss, K.M. (2004). Genetic basis for the evolution of vertebrate mineralized tissue. Proc Natl Acad Sci U S A *101*, 11356-11361.

Kawasaki, K., and Weiss, K.M. (2003). Mineralized tissue and vertebrate evolution: the secretory calcium-binding phosphoprotein gene cluster. Proc Natl Acad Sci U S A *100*, 4060-4065.

Kawasaki, K., and Weiss, K.M. (2006). Evolutionary genetics of vertebrate tissue mineralization: the origin and evolution of the secretory calcium-binding phosphoprotein family. J Exp Zool B Mol Dev Evol *306*, 295-316.

Kawasaki, K., and Weiss, K.M. (2008). SCPP gene evolution and the dental mineralization continuum. J Dent Res *87*, 520-531.

Kim, J.W., Lee, S.K., Lee, Z.H., Park, J.C., Lee, K.E., Lee, M.H., Park, J.T., Seo, B.M., Hu, J.C., and Simmer, J.P. (2008). FAM83H mutations in families with autosomal-dominant hypocalcified amelogenesis imperfecta. Am J Hum Genet *82*, 489-494.

Kim, J.W., Seymen, F., Lee, K.E., Ko, J., Yildirim, M., Tuna, E.B., Gencay, K., Shin, T.J., Kyun, H.K., Simmer, J.P., *et al.* (2013). LAMB3 mutations causing autosomal-dominant amelogenesis imperfecta. J Dent Res *92*, 899-904.

Kim, J.W., Simmer, J.P., Hart, T.C., Hart, P.S., Ramaswami, M.D., Bartlett, J.D., and Hu, J.C. (2005). MMP-20 mutation in autosomal recessive pigmented hypomaturation amelogenesis imperfecta. J Med Genet *42*, 271-275.

Kogaya, Y., Kim, S., and Akisaka, T. (1990). Changes in ultrastructural distribution of dental basement membrane heparan sulfate during early mouse tooth development. J Biol Buccale *18*, 109-115.

Lacruz, R.S., Smith, C.E., Kurtz, I., Hubbard, M.J., and Paine, M.L. (2013). New paradigms on the transport functions of maturation-stage ameloblasts. J Dent Res *92*, 122-129.

Lacruz, R.S., Smith, C.E., Moffatt, P., Chang, E.H., Bromage, T.G., Bringas, P., Jr., Nanci, A., Baniwal, S.K., Zabner, J., Welsh, M.J., *et al.* (2012). Requirements for ion and solute transport, and pH regulation during enamel maturation. J Cell Physiol *227*, 1776-1785.

Lagerstrom, M., Dahl, N., Nakahori, Y., Nakagome, Y., Backman, B., Landegren, U., and Pettersson, U. (1991). A deletion in the amelogenin gene (AMG) causes X-linked amelogenesis imperfecta (AIH1). Genomics *10*, 971-975.

Lee, S.K., Seymen, F., Lee, K.E., Kang, H.Y., Yildirim, M., Tuna, E.B., Gencay, K., Hwang, Y.H., Nam, K.H., De La Garza, R.J., *et al.* (2010). Novel WDR72 mutation and cytoplasmic localization. J Dent Res *89*, 1378-1382.

Lu, Y., Papagerakis, P., Yamakoshi, Y., Hu, J.C., Bartlett, J.D., and Simmer, J.P. (2008). Functions of KLK4 and MMP-20 in dental enamel formation. Biol Chem *389*, 695-700.

Luder, H.U., Gerth-Kahlert, C., Ostertag-Benzinger, S., and Schorderet, D.F. (2013). Dental phenotype in Jalili syndrome due to a c.1312 dupC homozygous mutation in the CNNM4 gene. PLoS One *8*, e78529.

McGrath, J.A., Gatalica, B., Li, K., Dunnill, M.G., McMillan, J.R., Christiano, A.M., Eady, R.A., and Uitto, J. (1996). Compound heterozygosity for a dominant glycine substitution and a recessive internal duplication mutation in the type XVII collagen gene results in junctional epidermolysis bullosa and abnormal dentition. Am J Pathol *148*, 1787-1796.

Moffatt, P., Smith, C.E., Sooknanan, R., St-Arnaud, R., and Nanci, A. (2006a). Identification of secreted and membrane proteins in the rat incisor enamel organ using a signal-trap screening approach. Eur J Oral Sci *114 Suppl 1*, 139-146; discussion 164-135, 380-131.

Moffatt, P., Smith, C.E., St-Arnaud, R., Simmons, D., Wright, J.T., and Nanci, A. (2006b). Cloning of rat amelotin and localization of the protein to the basal lamina of maturation stage ameloblasts and junctional epithelium. Biochem J *399*, 37-46.

Nagai, N., Nakano, K., Sado, Y., Naito, I., Gunduz, M., Tsujigiwa, H., Nagatsuka, H., Ninomiya, Y., and Siar, C.H. (2001). Localization of type IV collagen a 1 to a 6 chains in basement membrane during mouse molar germ development. Int J Dev Biol *45*, 827-831.

Nanci A, S.C. (1992). Development and calcification of enamel. In Calcification in biological systems, E. Bonucci, ed. (Boca Raton, FL, CRC Press), pp. 313-343.

Nanci, A., Zalzal, S., and Kogaya, Y. (1993). Cytochemical characterization of basement membranes in the enamel organ of the rat incisor. Histochemistry *99*, 321-331.

Nishio, C., Wazen, R., Kuroda, S., Moffatt, P., and Nanci, A. (2010). Expression pattern of odontogenic ameloblast-associated and amelotin during formation and regeneration of the junctional epithelium. Eur Cell Mater *20*, 393-402.

Nishio, C., Wazen, R., Moffatt, P., and Nanci, A. (2013). Expression of odontogenic ameloblast-associated and amelotin proteins in the junctional epithelium. Periodontol 2000 *63*, 59-66.

Parry, D.A., Brookes, S.J., Logan, C.V., Poulter, J.A., El-Sayed, W., Al-Bahlani, S., Al Harasi, S., Sayed, J., Raif el, M., Shore, R.C., *et al.* (2012). Mutations in C4orf26, encoding a peptide with in vitro hydroxyapatite crystal nucleation and growth activity, cause amelogenesis imperfecta. Am J Hum Genet *91*, 565-571.

Parry, D.A., Poulter, J.A., Logan, C.V., Brookes, S.J., Jafri, H., Ferguson, C.H., Anwari, B.M., Rashid, Y., Zhao, H., Johnson, C.A., *et al.* (2013). Identification of mutations in SLC24A4, encoding a potassium-dependent sodium/calcium exchanger, as a cause of amelogenesis imperfecta. Am J Hum Genet *92*, 307-312.

Poulter, J.A., Brookes, S.J., Shore, R.C., Smith, C.E., Abi Farraj, L., Kirkham, J., Inglehearn, C.F., and Mighell, A.J. (2014a). A missense mutation in ITGB6 causes pitted hypomineralized amelogenesis imperfecta. Hum Mol Genet *23*, 2189-2197.

Poulter, J.A., El-Sayed, W., Shore, R.C., Kirkham, J., Inglehearn, C.F., and Mighell, A.J. (2014b). Whole-exome sequencing, without prior linkage, identifies a mutation in LAMB3 as a cause of dominant hypoplastic amelogenesis imperfecta. Eur J Hum Genet *22*, 132-135.

Poulter, J.A., Murillo, G., Brookes, S.J., Smith, C.E., Parry, D.A., Silva, S., Kirkham, J., Inglehearn, C.F., and Mighell, A.J. (2014c). Deletion of ameloblastin exon 6 is associated with amelogenesis imperfecta. Hum Mol Genet.

Rajpar, M.H., Harley, K., Laing, C., Davies, R.M., and Dixon, M.J. (2001). Mutation of the gene encoding the enamel-specific protein, enamelin, causes autosomal-dominant amelogenesis imperfecta. Hum Mol Genet *10*, 1673-1677.

Rao, S., and Witkop, C.J., Jr. (1971). Inherited defects in tooth structure. Birth Defects Orig Artic Ser *7*, 153-184.

Reith, E.J., and Boyde, A. (1981). Autoradiographic evidence of cyclical entry of calcium into maturing enamel of the rat incisor tooth. Arch Oral Biol *26*, 983-987.

Ryu, O., Hu, J.C., Yamakoshi, Y., Villemain, J.L., Cao, X., Zhang, C., Bartlett, J.D., and Simmer, J.P. (2002). Porcine kallikrein-4 activation, glycosylation, activity, and expression in prokaryotic and eukaryotic hosts. Eur J Oral Sci *110*, 358-365.

Sahlberg, C., Hormia, M., Airenne, T., and Thesleff, I. (1998). Laminin gamma2 expression is developmentally regulated during murine tooth morphogenesis and is intense in ameloblasts. J Dent Res *77*, 1589-1596.

Simmer, J.P., Fukae, M., Tanabe, T., Yamakoshi, Y., Uchida, T., Xue, J., Margolis, H.C., Shimizu, M., DeHart, B.C., Hu, C.C., *et al.* (1998). Purification, characterization, and cloning of enamel matrix serine proteinase 1. J Dent Res *77*, 377-386.

Simmer, J.P., and Hu, J.C. (2001). Dental enamel formation and its impact on clinical dentistry. J Dent Educ *65*, 896-905.

Simmer, J.P., Hu, Y., Lertlam, R., Yamakoshi, Y., and Hu, J.C. (2009). Hypomaturation enamel defects in Klk4 knockout/LacZ knockin mice. J Biol Chem *284*, 19110-19121.

Simmer, J.P., Papagerakis, P., Smith, C.E., Fisher, D.C., Rountrey, A.N., Zheng, L., and Hu, J.C. (2010). Regulation of dental enamel shape and hardness. J Dent Res *89*, 1024-1038.

Simmer, J.P., Richardson, A.S., Hu, Y.Y., Smith, C.E., and Ching-Chun Hu, J. (2012). A post-classical theory of enamel biomineralization... and why we need one. Int J Oral Sci *4*, 129-134.

Sire, J.Y., Davit-Beal, T., Delgado, S., and Gu, X. (2007). The origin and evolution of enamel mineralization genes. Cells Tissues Organs *186*, 25-48.

Smith, C.E. (1998). Cellular and chemical events during enamel maturation. Crit Rev Oral Biol Med *9*, 128-161.

Smith, C.E., McKee, M.D., and Nanci, A. (1987). Cyclic induction and rapid movement of sequential waves of new smooth-ended ameloblast modulation bands in rat incisors as visualized by polychrome fluorescent labeling and GBHA-staining of maturing enamel. Adv Dent Res *1*, 162-175.

Smith, C.E., and Nanci, A. (1995). Overview of morphological changes in enamel organ cells associated with major events in amelogenesis. Int J Dev Biol *39*, 153-161.

Somogyi-Ganss, E., Nakayama, Y., Iwasaki, K., Nakano, Y., Stolf, D., McKee, M.D., and Ganss, B. (2012). Comparative temporospatial expression profiling of murine amelotin protein during amelogenesis. Cells Tissues Organs *195*, 535-549.

Tagliabracci, V.S., Engel, J.L., Wen, J., Wiley, S.E., Worby, C.A., Kinch, L.N., Xiao, J., Grishin, N.V., and Dixon, J.E. (2012). Secreted kinase phosphorylates extracellular proteins that regulate biomineralization. Science *336*, 1150-1153.

Takano, Y. (1979). Cytochemical studies of ameloblasts and the surface layer of enamel of the rat incisor at the maturation stage. Arch Histol Jpn *42*, 11-32.

Ten Cate, A.R. (1959). The histochemistry of human tooth development. Proc Nutr Soc *18*, 65-70.

Ten Cate, A.R. (1996). The role of epithelium in the development, structure and function of the tissues of tooth support. Oral Dis *2*, 55-62.

Thesleff, I., Vaahtokari, A., and Partanen, A.M. (1995). Regulation of organogenesis. Common molecular mechanisms regulating the development of teeth and other organs. Int J Dev Biol *39*, 35-50.

Trueb, B., Taeschler, S., Schild, C., and Lang, N.P. (2007). Expression of phosphoproteins and amelotin in teeth. Int J Mol Med *19*, 49-54.

Wang, S., Choi, M., Richardson, A.S., Reid, B.M., Seymen, F., Yildirim, M., Tuna, E., Gencay, K., Simmer, J.P., and Hu, J.C. (2014a). STIM1 and SLC24A4 Are Critical for Enamel Maturation. J Dent Res.

Wang, S.K., Choi, M., Richardson, A.S., Reid, B.M., Lin, B.P., Wang, S.J., Kim, J.W., Simmer, J.P., and Hu, J.C. (2014b). ITGB6 loss-of-function mutations cause autosomal recessive amelogenesis imperfecta. Hum Mol Genet *23*, 2157-2163.

Wang, S.K., Hu, Y., Simmer, J.P., Seymen, F., Estrella, N.M., Pal, S., Reid, B.M., Yildirim, M., Bayram, M., Bartlett, J.D., *et al.* (2013). Novel KLK4 and MMP20 mutations discovered by whole-exome sequencing. J Dent Res *92*, 266-271.

Warshawsky, H., and Nanci, A. (1982). Stereo electron microscopy of enamel crystallites. J Dent Res *Spec No*, 1504-1514.

Weatherell, J.A. (1975). Composition of dental enamel. Br Med Bull *31*, 115-119.

Witkop, C.J. (1957). Hereditary defects in enamel and dentin. Acta Genet Stat Med *7*, 236-239.

Witkop, C.J., Jr. (1988). Amelogenesis imperfecta, dentinogenesis imperfecta and dentin dysplasia revisited: problems in classification. J Oral Pathol *17*, 547-553.

Yamakoshi, Y., Hu, J.C., Fukae, M., Yamakoshi, F., and Simmer, J.P. (2006). How do enamelysin and kallikrein 4 process the 32-kDa enamelin? Eur J Oral Sci *114 Suppl 1*, 45-51; discussion 93-45, 379-380.

Yoon, H., Laxmikanthan, G., Lee, J., Blaber, S.I., Rodriguez, A., Kogot, J.M., Scarisbrick, I.A., and Blaber, M. (2007). Activation profiles and regulatory cascades of the human kallikrein-related peptidases. J Biol Chem *282*, 31852-31864.

Yoshiba, N., Yoshiba, K., Aberdam, D., Meneguzzi, G., Perrin-Schmitt, F., Stoetzel, C., Ruch, J.V., and Lesot, H. (1998). Expression and localization of laminin-5 subunits in the mouse incisor. Cell Tissue Res *292*, 143-149.

Young, R.A., and Spooner, S. (1970). Neutron difraction studies of human tooth enamel. Arch Oral Biol *15*, 47-63.

CHAPTER 2

MOUSE MODELS

ABSTRACT

Amtn-null and *Klk4*-null mice were bred together to obtain *Amtn*/*Klk4*-heterozygous and *Amtn*/*Klk4* double null mice to determine if the absence of both AMTN and KLK4 during mouse development produces a more severe enamel phenotype than when only one of these proteins is absent. Both of these null mice (*Klk4* and *Amtn*) have a *lac*Z coding region inserted (knocked in) precisely at their translation initiation sites. Characterization of the enamel phenotype focused on the continuously growing mandibular incisors, which were investigated by morphological observations and for knockin gene expression, as determined by *lacZ* histochemistry and RT-PCR/DNA sequencing analyses. Morphologically, the *Amtn*-null mouse mandibular incisor enamel had a chalky appearance and occasionally exhibited chipping at the incisal edge. The enamel formed by the *Amtn*/*Klk4*-heterozygous mice was indistinguishable from that of wild-type mice, while the *Amtn*/*Klk4*-null mouse enamel was indistinguishable from that of the *Klk4*-null mice, being chalky-white and exhibiting extensive attrition of the incisal edge. Histologically, *lacZ* expression in the *Amtn* null was surprisingly weak. RT-PCR and DNA sequence analyses demonstrated that the *lac*Z exon was being deleted

during RNA splicing of the *Amtn* knockin transcripts, making accurate temporal and spatial characterization of *Amtn* expression by histochemical studies impractical.

INTRODUCTION

Rodents have been established as an ideal model for the study of tooth development. Since mouse incisors grow continuously, it is possible to observe all of the stages of amelogenesis in a single incisor (Smith et al., 1987; Smith and Nanci, 1989). Enamel is only present on the facial aspect of the incisors (Smith, 1998; Smith et al., 1987), but the different stages of enamel formation can be precisely and reproducibly localized along the length of the incisor using anatomical landmarks on the hemimandible (Fig. 2.1).

The locations of the different stages of amelogenesis along the length of the continuously growing incisor are mapped according to 1 mm increments, starting from the apical loop (Smith et al., 2011a). The secretory stage of amelogenesis begins about 1 mm from the apical loop and continues for 2 mm before transitioning into the maturation stage, which reproducibly initiates between the mesial root of the second molar and the distal root of the first molar (Fig. 2.1). In this study, the mandibular incisor was studied due to ease of access and frequent usage in the literature of enamel formation. The main area of interest for this study was 8 mm from the apical loop, which is in late maturation, near eruption, allowing us to study fully developed enamel that has not yet been damaged during masticatory function.

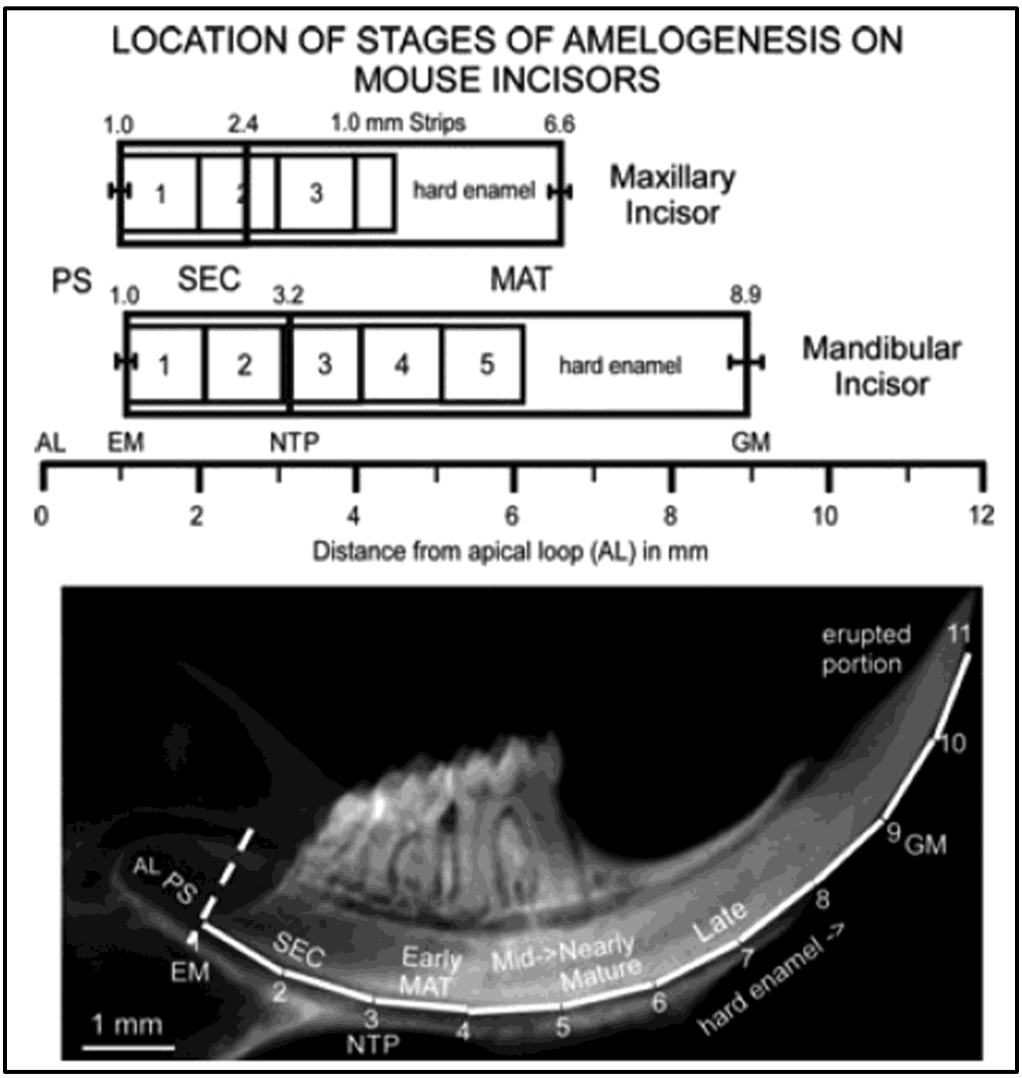

Fig. 2.1. Schematic drawing of the location of stages of amelogenesis and sites for enamel strip dissections on maxillary and mandibular mouse incisors, and radiograph of a mandibular incisor enlarged to a similar scale as the schematic drawing. In normal wild-type mice, three, and sometimes four, 1-mm-long strips of developing enamel can generally be dissected from maxillary incisors across the length of the tooth from the start of the secretory stage (EM, SEC) to about the midpoint of the maturation stage (MAT), where the enamel becomes so hard that it physically damages the scalpel blades used to partition the enamel layer into strips. On mandibular incisors, usually two strips can be obtained from the secretory stage and three strips from the maturation stage before the enamel is too hard to dissect by hand. Because the average strip number per series is not an integer on maxillary incisors (3.5 strips per series per tooth) unlike mandibular incisors (5.0 strips per series per tooth), data for the most incisally positioned strip on maxillary incisors tend to have higher variation than comparable strips on mandibular incisors. In the radiograph below the schematic drawing, the dotted line indicates the boundary between the presecretory stage (PS) and the beginning of the secretory stage (SEC) on the mandibular incisor. The numbered white lines correspond to imaginary strips spaced at 1-mm intervals. AL, apical loop; EM, the point marking the start of enamel matrix formation; GM, gingival margin where the erupted portion of the incisor starts; MAT, maturation stage; NTP, 'no Tome's processes' visible on ameloblasts; PS, presecretory stage. Adapted with permission from (Smith et al., 2011a).

The focus of this project is the maturation stage of amelogenesis where the proteins AMTN and KLK4 are secreted by ameloblasts (Moffatt et al., 2006; Simmer et al., 2009; Somogyi-Ganss et al., 2012). KLK4 is a secreted serine protease that is necessary for enamel to reach its final hardness by degrading extracellular enamel proteins and thereby facilitating their removal (by ameloblasts) from the developing enamel. The removal of enamel proteins vacates space between the enamel crystallites, which allows them to grow in width and thickness until they contact adjacent crystallites and interlock (Simmer et al., 2011b; Smith et al., 2011b). AMTN is a secreted protein that is primarily associated with the basal lamina (Dos Santos Neves et al., 2012; Nishio et al., 2010). We bred the *Amtn*-null with *Klk4*-null mice to obtain an *Amtn*/*Klk4*-double null mouse. We expected that if KLK4 and AMTN served independent functions during the maturation stage, that the enamel malformations in the double null mice would be additive and therefore more severe than in the single nulls.

MATERIALS AND METHODS

Animal Protocol

All procedures involving animals were reviewed and approved by the Institutional Animal Care and Use Committees (IACUC) at the University of Michigan. Wild-type (WT), *Amtn*-null, *Klk4*-null, *Amtn*/*Klk4*-heterozygous, and *Amtn*/*Klk4*-null mice were

maintained on diet gel chow, and on 12-hour light/dark cycles. Genotyping of mice was done by tail biopsy using the Qiagen DNeasy blood and tissue kit (cat. 69506, Venlo, Netherlands) following manufacturer directions. Mouse photographs were taken using a Nikon DXM1200 camera on a Nikon Eclipse E600 dissecting microscope (Mitsubishi Group, Tokyo, Japan).

Klk4 Targeting Construct and Genotyping

The targeting construct for the *Klk4*-null mouse was previously described (Simmer et al., 2009) (Fig 2.2). Mice were generated on a C57BL/6 background. Briefly, the construct was designed to insert a NLS-*lacZ* (ß-galactosidase) reporter containing a mouse nuclear localization signal (NLS) replacing the entire mouse *Klk4* coding sequence starting with the initiation codon in exon 2 and ending downstream of the last coding exon (exon 6). Mice were genotyped using two primer pairs. To detect the wild-type *Klk4* gene, we used primers that annealed to intron 3 (5′-AACCTAAGGGACAGGGCAGT) and exon 5 (5′-TGAGGTGGTACACAGGGTCA; 550-bp amplicon). The *Klk4* knockin (null) gene was detected with a primer pair that annealed within the NLS-*lac*Z sequence: (5′-TGCCTCCAACCAGATAGGTC and 5′-GACAGTATCGGCCTCAGGAA; 595-bp amplicon). PCR conditions were as follows: 94 °C/5 min, followed by cycling for 35 times at 94 °C/30sec, 58 °C/30sec, 74 °C/60 sec and final elongation at 72 °C/7 min. Wild-

type mice showed the presence of a single *Klk4* band, *Klk4*-heterozygous mice showed a *Klk4* and a *Klk4-lacZ* band, and *Klk4*-null mice showed a single *Klk4-lacZ* band.

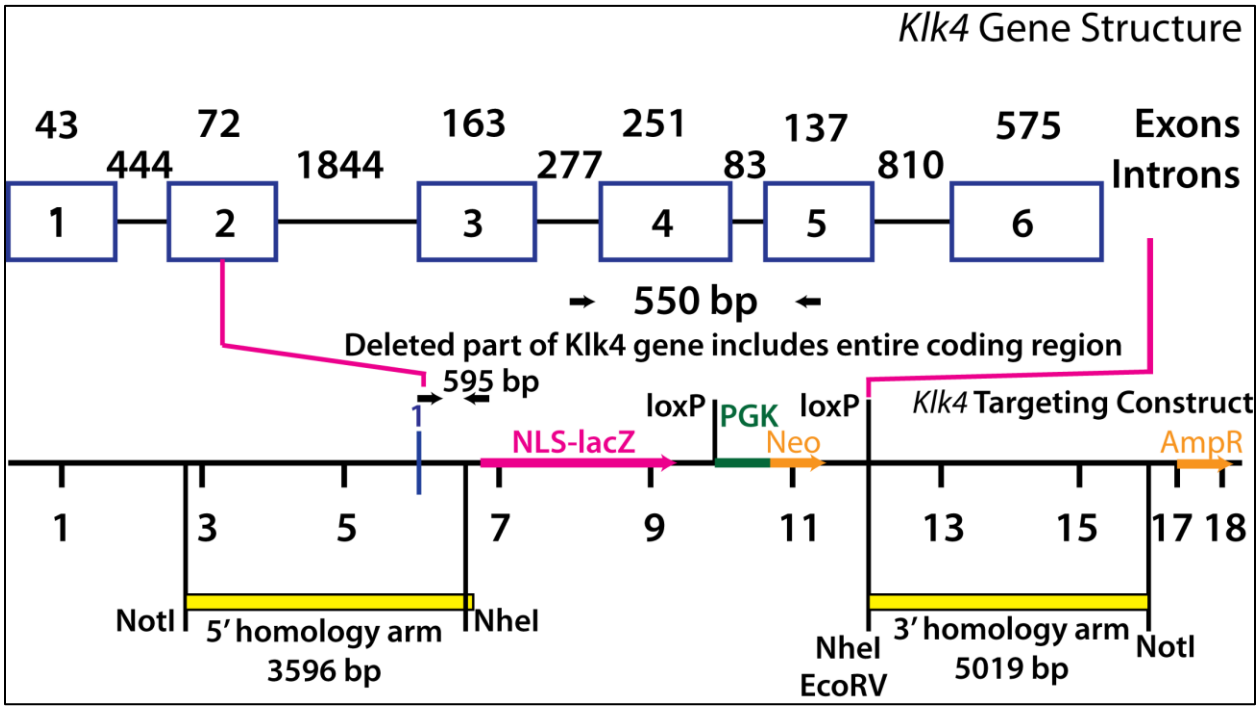

Fig 2.2. Gene targeting strategy for the Klk4 mouse. Depiction of the mouse *Klk4* gene and the targeting construct. Numbered boxes indicate *Klk4* exons (2 through 6 are coding). The number of nucleotides is shown above each exon and intron. The targeting construct was designed to replace the *Klk4* coding region with NLS-*lacZ* so that the *Klk4* promoter would drive reporter expression. The 5'-homology arm ended in exon 2 at the *Klk4* translation initiation codon. The 3'-homology arm started downstream of exon 6, so that the entire *Klk4* coding region was deleted. Downstream of the reporter gene was the selection gene (PGK-Neo) bracketed by loxP recombination signals that was later deleted by mating with mice expressing Cre recombinase. Black arrowsmark the PCR primer annealing sites to amplify the wild-type *Klk4* (550 bp) and the *lacZ* transgene (595 bp) sequences. Adapted with permission from (Simmer et al., 2009).

Amtn Targeting Construct and Genotyping

Amtn-null mice generated on a C57BL/6 background were received from Dr. Bernhard Ganss from the University of Toronto (Toronto, Canada). The *Amtn* knockout has a *lacZ* (β-galactosidase) reporter and a downsteam neomycin (Neo) selection marker inserted

at the *Amtn* translation initiation site in exon 2. This insert is 4617 bp in length. It replaces the 54 bp of *Amtn* exon 2 coding sequence and 37 bp (out of 1675 bp) at the 5′ end of intron 2. The structure of the *Amtn* gene was adapted from a previous study (Moffatt et al., 2006) and is included with permission (Fig. 2.3).

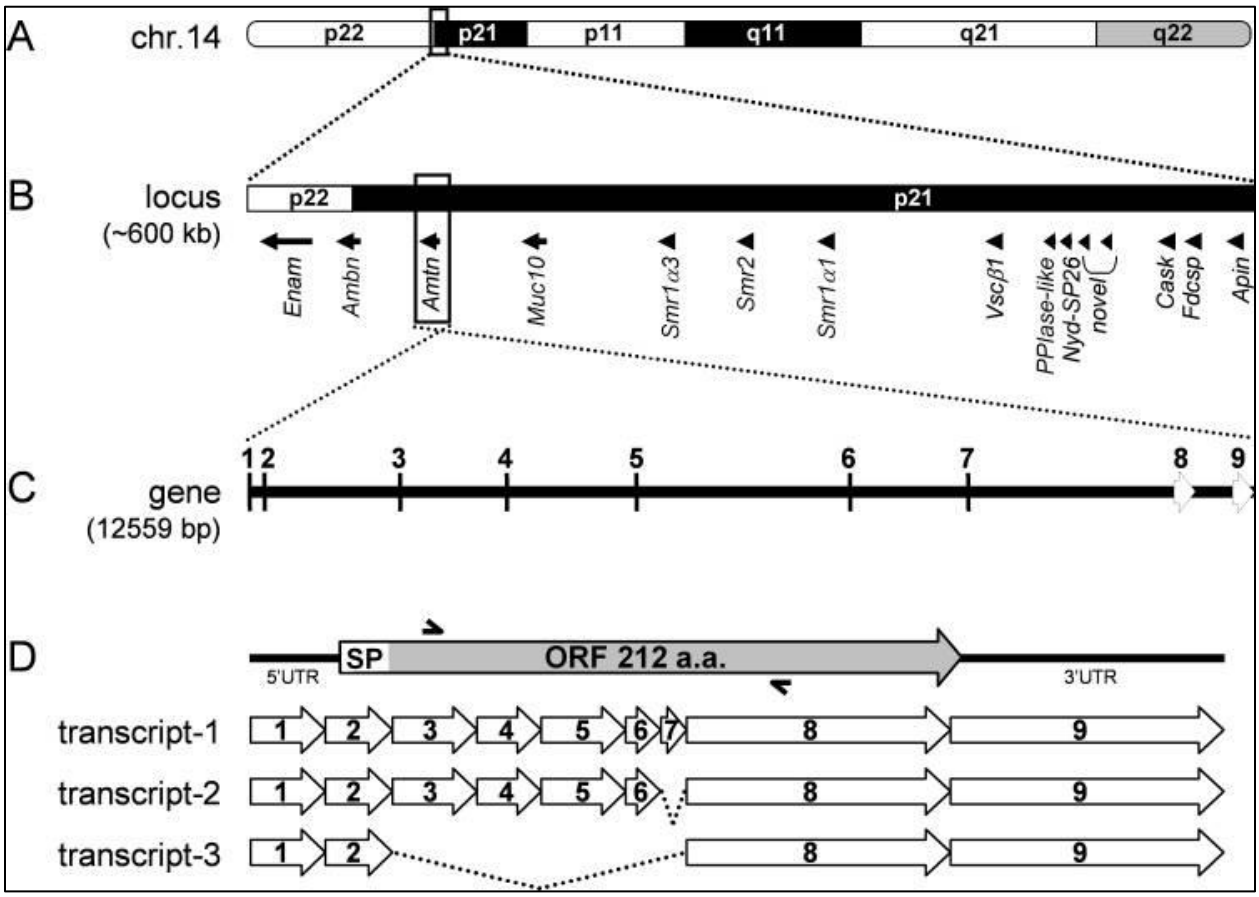

Fig. 2.3. Schematic representation of the location and structure of the rat *Amtn* gene and its derived transcripts. The rat *Amtn* gene is located on chromosome 14 (**A**) flanked by the enamel-specific genes *Ambn* and *Enam*, and the salivary gland *mucin 10* (*Muc10*) (**B**). The 600 kb locus containing *Amtn* is rich in genes encoding secreted proteins such as the *submandibular glands androgen regulated* genes (*Smr*) and at the other extremity *casein kappa* (*Cask*), *follicular dendritic cells secreted peptide* (*Fdcsp*) and *APin* (**B**). The *Amtn* gene is composed of nine exons covering roughly 12 kb (**C**). The three different transcripts identified are depicted with the matching exons location (**D**). Semi-arrowheads above and below the longest cDNA (**D**) indicate location of the primers used for RT–PCR. ORF, open reading frame; SP, signal peptide. 5′UTR, 5′ untranslated region. Adapted with permission from (Moffatt et al., 2006).

Two primer pairs were used for genotyping. To detect the *Amtn* wild-type gene, the 5′ primer annealed to *Amtn* exon 1 (5′-GTGGAGAAGTCATCTGGATTTCG), which is found on both the wild-type and *Amtn* knockin genes, and was paired with a primer that annealed to the 3′ end of exon 2 (5′-ACTGGTAATGACTGGGCTGAT; 226-bp amplicon), which is only found on the *Amtn* wild-type gene. To detect the *Amtn* knockout/*lac*Z knockin gene, the 5′ primer (5′-ATTGCTGAAGAGCTTGGCGGCG) annealed to the *Neo* cassette downstream of the lacZ knockin, while the 3′ primer (5′-CACTCTGTCCCTCAGGGCTGCTA; 466-bp amplicon) annealed within *Amtn* intron 2. PCR conditions were as follows: 94 °C/5 min, followed by cycling for 35 times at 94 °C/30 sec, 58 °C/ 30 sec, 72 °C/60 sec and final elongation at 72 °C/7 min. Wild-type mice showed the presence of a single *Amtn* band, *Amtn*-heterozygous mice showed an *Amtn* and an *Amtn-lacZ* band, and *Amtn*-null mice showed a single *Amtn-lacZ* band. A typical result is shown in Fig. 2.4.

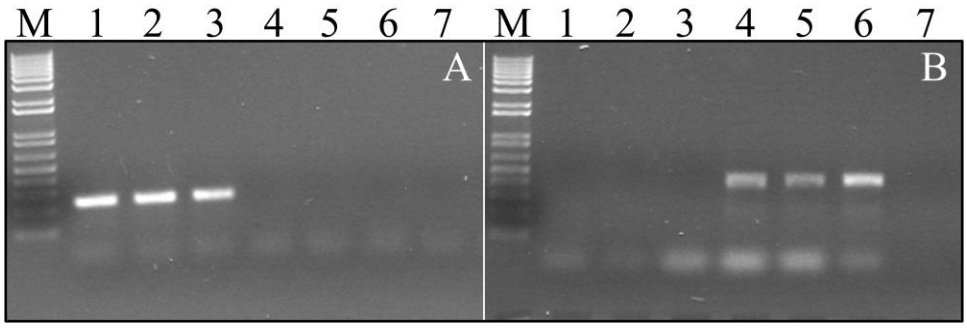

Fig. 2.4. Genotyping for *Amtn*-null mice. Lanes 1 through lanes 3 are PCR amplifications using tail biopsies from wild-type mice (*Amtn*$^{+/+}$) as template, and lanes 4 through lanes 6 are PCR amplification products of tail biopsies from *Amtn*-null (*Amtn*$^{-/-}$) mice as template. Lane 7 is a negative (no DNA) control. ***A:*** Primers specific for the *Amtn* wild-type gene show the expected the 226-bp PCR amplification product. ***B:*** Primers specific for the *Amtn*-null gene show the expected the 466-bp PCR amplification product.

Breeding Strategy

To generate *Amtn*/*Klk4*-null mice, *Amtn*-null mice were bred with *Klk4*-nulls to generate *Amtn*/*Klk4*-heterozygous litters. This cage was also used to maintain a supply of heterozygous control mice. The double heterozygous littermates were then bred with each other to obtain *Amtn*/*Klk4*-null mice, which were expected to appear with a frequency of 1/16. Pups were genotyped by tail biopsy for *Amtn* and *Klk4* as described above. Once male and female *Amtn*/*Klk4*-null mice were obtained, double null breeding pairs were used to establish the double null colony.

β-Galactosidase Expression Assay

Mouse heads were collected from postnatal days 5 (secretory stage), 11 (maturation stage), and 14 (late maturation stage), sectioned in half, and fixed in 4% paraformaldehyde (PFA) overnight at 4˚C. The following morning, heads were washed in phosphate-buffered saline (PBS, 137 mM NaCl, 10 mM phosphate, 2.7 mM KCl, pH 7.4) (3 x 30 minutes). Mouse heads were then transferred to 4.13% EDTA, pH 7.4 at 4 ˚C with constant agitation for decalcification (D5 – 8 days, D11- 21 days, D14 – 30 days) with a change of fresh solution every 2-3 days. Decalcified tissues were washed in PBS (3 x 30 minutes) and embedded in Tissue-Tek® O.C.T. Compound (ProSciTech, Queensland, Australia). Blocks were cryosectioned at 10-μm thickness, post-fixed for 5 minutes in 0.5% glutaraldehyde, washed in PBS (3 x 5 minutes), and incubated for 5

hours in freshly prepared X-gal staining buffer, pH 8.0, containing 1 mg/mL X-gal, 100 mM HEPES, 5 mM potassium ferricyanide, 5 mM potassium ferrocyanide, 1 mM $MgCl_2$, 2% Triton X-100, and 1 mM dithiothreitol as described previously (Simmer et al., 2009). Tissue sections were rinsed in PBS and counterstained with hematoxylin. Images were taken using a Nikon Eclipse TE 300 microscope (Mitsubishi Group, Tokyo, Japan), Nikon DXM1200 camera (Mitsubishi Group, Tokyo, Japan), and Act1 imaging software (Mager Scientific, Dexter, MI).

RT-PCR and DNA Sequencing Analyses

RNA was extracted from the first molars of 11-day old pups using Qiagen RNeasy mini kit (cat. 74106, Qiagen, Venlo, Netherlands) and analyzed with Superscript III One-Step RT-PCR system with Platinum Taq (Invitrogen, Grand Island, NY). Reactions of 50 uL containing about 200 ng of RNA were set up following manufacturer instructions. *Amtn* gene-specific primers were designed using Primer 3 on the Web (http://frodo.wi.mit.edu/primer3/). The forward primer annealed to *Amtn* exon 1 (5'-GTGGAGAAGTCATCTGGATTTCG-3'), exon 2 (5'-GGATCAGCCCAGTCATTACC-3'), or exon 3 (5'-AGCAGCTTAACCCTGCTTCG-3'), and was paired with a common reverse primer that annealed to *Amtn* exon 8 (5'-TCTGCACATCTGGTTTAGTGC-3'). The predicted product sizes of these amplifications using the wild-type *Amtn* cDNA as template were: exon 1 to exon 8, 522-bp; exon 2 to exon 8, 424-bp; and exon 3 to exon 8,

402-bp. Control reactions were conducted using *Gapdh* gene-specific primers (forward 5′-ACTCCACTCACGGCAAATTC-3′ and reverse 5′-CACATTGGGGGTAGGAACAC-3′) as a loading control. RT-PCR conditions were as follows: 55 °C/30 min, 94 °C/2 min, followed by cycling for 35 times at 94 °C/30 sec, 58 °C/30 sec, 68 °C/30 sec and final elongation at 68 °C/5 min. PCR reactions were resolved on 1% agarose gels and stained with ethidium bromide. DNA bands were removed from the gel with a scalpel, and DNA was extracted using the QIAquick gel extraction kit (cat. 28706, Qiagen, Venlo, Netherlands). Samples were then sent to the University of Michigan, DNA sequencing core for analysis.

RESULTS

Klk4$^{-/-}$ and *Amtn*$^{-/-}$ were successfully bred to generate double heterozygous (*Klk4*$^{+/-}$*Amtn*$^{+/-}$) and double null (*Klk4*$^{+/+}$*Amtn*$^{+/+}$) mice. The first step in the characterization of these mice was to inspect and photograph the incisors at low magnification using a dissecting microscope (Fig. 2.5). In addition, the mandibles were removed and split at the mental symphysis. The hemimandibles were cleaned of soft tissue, and inspected and photographed under a dissecting microscope (Fig. 2.6). These simple studies provided valuable information about the gross appearance of the enamel. First and foremost they provided our first evidence of an enamel phenotype in

the *Amtn* null mice. It also became evident that the *Amtn* null enamel phenotype was mild relative to that of the *Klk4* nulls.

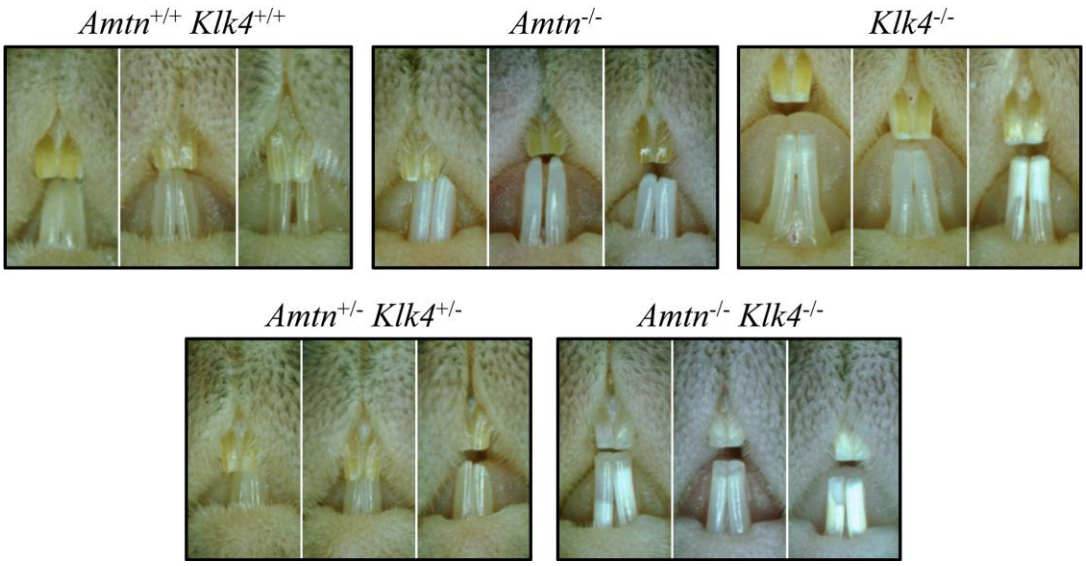

Fig. 2.5. The incisor phenotype. Photographs of perfused mice showing gross morphological phenotypes of the mandibular incisors. All mice pictured are 7-weeks old. Wild-type (*Amtn*$^{+/+}$*Klk4*$^{+/+}$) and *Amtn*/*Klk4*-heterozygous mice (*Amtn*$^{+/-}$*Klk4*$^{+/-}$) are similar in appearance. *Amtn*-null (*Amtn*$^{-/-}$) mice are chalky and occasionally a chip at the incisal edge. *Klk4*-null (*Klk4*$^{-/-}$) and *Amtn*/*Klk4* double null (*Amtn*$^{-/-}$ *Klk4*$^{-/-}$) incisors are chalky-white and show severe wear and chipping at their incisal edges.

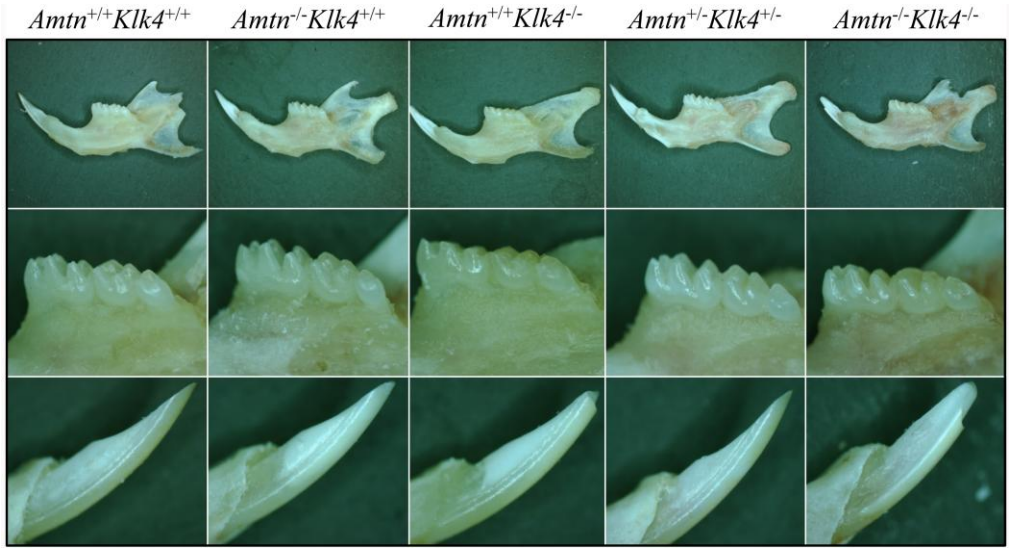

Fig. 2.6. Hemimandibles, molars and incisors from 7-week old mice. ***Top:*** Hemimandibles; ***Middle:*** mandibular molars; ***Bottom:*** mandibular incisors. *Amtn*-null mice have chalky incisors that sometimes break at the incisal edge, especially on a hard diet. The enamel made by *Amtn*/*Klk4*-heterozygous mice lack a discernible enamel phenotype and is similar to wild-type. *Klk4*-null and *Amtn*/*Klk4*-null double null mouse incisors are chalky-white and undergo rapid attrition. The molars of these mice also undergo rapid attrition.

Wild-type mice have incisors with a yellowish pigmentation due to the incorporated iron, which makes up about 0.03% of the enamel by weight (Pindborg, 1953; Wen and Paine, 2013). *Amtn*-null mice have chalkier incisors that occasionally chip, but usually stay intact when the mice are maintained on a soft diet. *Klk4*-null mice also have chalky-white incisors, but these incisors undergo rapid and severe enamel attrition after they erupt into function. The molars of all 5 genotypes $Amtn^{+/+}Klk4^{+/+}$, $Amtn^{+/+}Klk4^{-/-}$, $Amtn^{-/-}Klk4^{+/+}$, $Amtn^{+/-}Klk4^{+/-}$, and $Amtn^{-/-}Klk4^{-/-}$ mice have normal form prior to eruption (data not shown). As the final thickness and volume of the enamel layer is established in the early (secretory) stage, amelogenesis during the secretory stage appears to have proceeded normally. This is consistent with the known expression patterns of *Klk4* and *Amtn*. To provide additional data on the temporal and spatial patterns of these genes during amelogenesis, we took advantage of the lacZ knockin features of these mice by performing histochemistry on maxillary molars at various stages of development (Fig. 2.7).

NLS-*lacZ* expression in *Klk4*-null mice has been previously described (Simmer et al., 2009). We found that *lacZ* expresses weakly in the *Amtn*-null mouse. AMTN has been established as a maturation stage protein (Moffatt et al., 2006; Somogyi-Ganss et al., 2012). We found expression of the *Amtn-LacZ* reporter, particularly in 14-day old pups to be very weak to non-existent, particularly compared to the *Klk4-LacZ* reporter, which is strongly expressed in the maturation stage in day 11 and day 14 molars. Due to

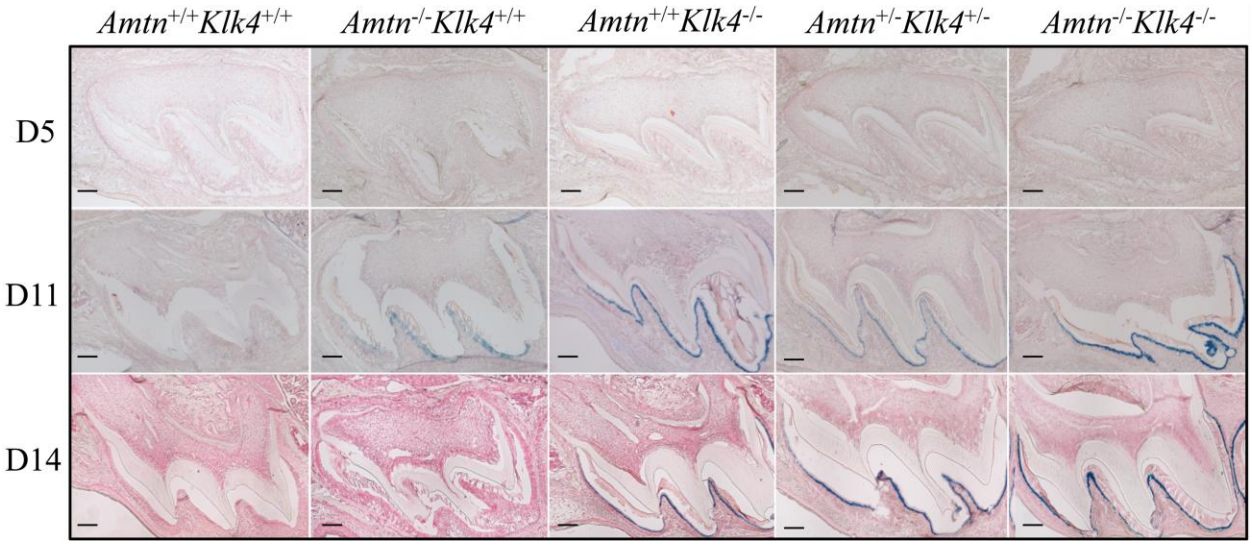

Fig. 2.7. *Lac*Z Histostaining. Ameloblasts in Day 5 (D5) maxillary first molars are in the secretory stage of amelogenesis. No *lac*Z staining was observed in any of the genotypes. Ameloblasts in Day 11 (D11) maxillary first molars are in the maturation stage. Positive *lac*Z staining specifically in ameloblasts was observed in all molars except the wild-type mice. Day 14 (D14) maxillary first molars are completing crown formation just prior to eruption. (Bars = 100 μm).

this low expression, the *Amtn-lacZ* reporter is not ideal for characterizing the temporal and spatial pattern of *Amtn* expression in this knockout mouse model. *LacZ* expressed in both the *Amtn*/*Klk4*-heterozygous and the *Amtn*/*Klk4*-null mice in the maturation stage but due to the low expression of the *Amtn-LacZ* reporter, most of this labeling is likely due to the *Klk4-lacZ* reporter.

Due to the low *lac*Z expression in the *Amtn* null mouse, we conducted RT-PCR to better characterize expression of the Amtn knockout/lacZ knockin gene (Fig. 2.8.A and 2.8.B). RNA was extracted from Day 11 maxillary first molars, converted to cDNA, and amplified with 3 different primers pairs. The same (exon 8) reverse primer located in exon 8 was used in all reactions. When a forward primer that annealed in exon 1 was used, the *Amtn*-null mice showed a smaller band than the age-matched wild-type pup

(Fig. 2.8.A, panel A). This band disappeared entirely when a forward primer in exon 2 was used (Fig. 2.8.A, panel B). The band reappeared when the forward primer was placed in exon 3, except now the band in the *Amtn*-null pups was the same size as that of the wild-type pup (Fig. 2.8.A, panel C). *Gapdh* control showed similar expression in the *Amtn*-null samples (Fig. 2.8.B.).

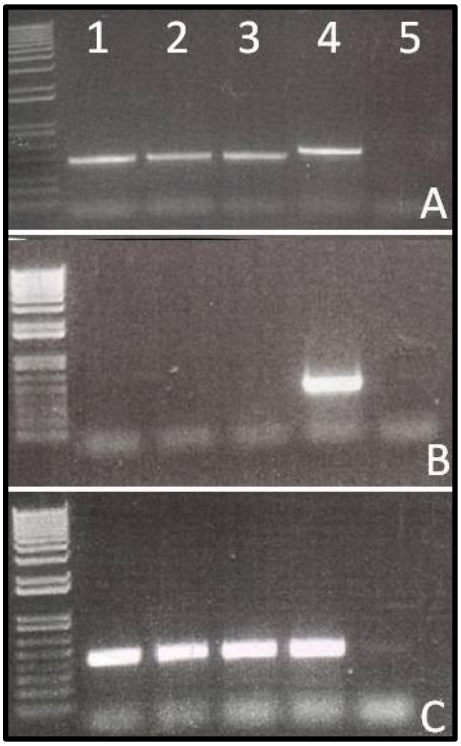

Fig. 2.8.A. RT-PCR Results. Columns 1-3 are from 11-day old *Amtn*-null pups. Column 4 is from an 11-day old wild-type pup. Column 5 is the negative control. (A) Forward primer was in exon 1, reverse primer in exon 8. The bands from *Amtn*-null pups were smaller than the wild-type pup. (B) Forward primer in exon 2, reverse primer in exon 8. No bands were found for any of the *Amtn*-null pups (C) Forward primer in exon 3, reverse primer in exon 8. Bands from *Amtn*-null and wild-type pups were now the same size.

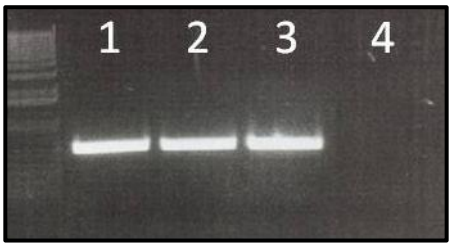

Fig. 2.8.B. RT-PCR GAPDH loading control. Lanes 1 through 3 are from Day 11 *Amtn*-null mice. Lane 4 is the negative control.

To further explain these results, we sequenced the bands obtained in Fig. 2.8.A. (Fig. 2.9). With the sequencing results, we found that in the *Amtn*-null mouse, exon 2 containing the *lac*Z reporter and ATG start codon is being spliced out, which explains the weak appearance of *lac*Z in the first molar.

Fig. 2.9. Sequencing of exon 1 to 8 RT-PCR bands. RT-PCR bands amplified from Day 11 *Amtn*-null and wild-type maxillary first molars were characterized by DNA sequencing. In the *Amtn*-null mouse, the exon containing *lac*Z is being spliced out, including the ATG start codon. No other in-frame ATG codons are found until exon 6, suggesting that no AMTN protein is being produced in this mouse.

DISCUSSION

Wild-type mice have enamel on the facial of their incisors with yellow pigmentation (Wen and Paine, 2013). Compared to the wild-type mice, the defect in the *Amtn*-null mice appears to be minor on gross morphological examination (Fig. 2.5 and 2.6). While there is some chalky discoloration of the mandibular incisors, the incisors generally appear intact and functional, possibly because the pellets used for the mice are softer. This seems to suggest that AMTN might be having an effect on the outer portion of the enamel, given that there doesn't seem to be any major changes affecting structural integrity of the enamel layer in the *Amtn*-null mice.

The most severe phenotype was observed in the *Klk4*-null and *Amtn*/*Klk4*-null mice, which showed very chalky-white incisors with significant chipping at the incisal edge, as described previously (Simmer et al., 2009; Simmer et al., 2011a). These mice had to be maintained on soft chow to ensure adequate nutrition. It is likely that the bulk of the phenotype observed in the *Amtn*/*Klk4*-null mice is due to the absence of KLK4, given the mild phenotype observed in *Amtn*-null mice. *Amtn*/*Klk4*-heterozygous mice appeared similar to wild-type mice. This suggests that defects resulting from the missing AMTN and KLK4 proteins are transmitted recessively.

Previously, AMTN has been established as a transition and maturation stage protein (Iwasaki et al., 2005; Moffatt et al., 2006). We wanted to refine its temporospatial expression in mouse first molars. However, due to the poor *lacZ* expression in the

Amtn-null mouse, β-galactosidase was not a good reporter for studying timing and localization of *Amtn* in this mouse model.

To get a better understanding of *Amtn* gene expression in this mouse in the maturation stage, we conducted RT-PCR analysis using forward primers for exons 1, 2, and 3 with a reverse primer in exon 8 using RNA obtained from day 11 mouse molars that are in the maturation stage. While there was no observed transcript when the forward primer in exon 2 was used, there was a detectable transcript with a forward primer in exon 1 that was smaller than that of the wild-type transcript. A transcript of the same size as the wild-type was also observed when the forward primer in exon 3 was used.

The band in day-11 *Amtn*-null mice when the forward primer in exon 1 was used was excised and prepared for sequencing along with a comparable wild-type sample. The sequencing results showed that exon 2 was spliced out during RNA processing of the transcript, including the ATG start codon (Fig. 2.9) and the *lacZ* coding sequence. This explained why *lacZ* expression in this mouse was so weak at time points where strong expression would be expected (Fig. 2.7). Analysis of the AMTN amino acid sequence outside of exon 2 revealed only 2 in-frame ATG start codons, in exons 6 and 8, so it was very unlikely that any AMTN protein was being translated from the *Amtn*-null transcript that had deleted exon 2 during RNA splicing.

In summary, we received the *Amtn* mice from Dr. Ganss and bred them with *Klk4* null mice. We examined and compared the molar and incisor morphologically from mice with 5 genotypes: $Amtn^{+/+}Klk4^{+/+}$, $Amtn^{+/+}Klk4^{-/-}$, $Amtn^{-/-}Klk4^{+/+}$, $Amtn^{+/-}Klk4^{+/-}$, and $Amtn^{-/-}Klk4^{-/-}$. The $Amtn^{-/-}$ mice showed a mild enamel phenotype that was most evident in the mandibular incisor, which was chalky and tended to chip. *Lac*Z histostaining was weak in the $Amtn^{-/-}$ mice, but confirmed expression of *Amtn* in maturation stage ameloblasts. RT-PCR analyses confirmed that a *lac*Z gene and downstream *Neo* cassette had been successfully inserted into *Amtn* at the translation initiation site, thus preventing normal expression of *Amtn*. We also determined that, apparently due transcription of the knockin gene was not terminating at the intended polyadenylation sites and proceeded to downstream, which allowed the *lac*Z knockin to be deleted during RNA splicing and diminished its sensitivity as a marker for *Amtn* expression. There are only 2 downstream in-frame ATG codons in *Amtn*, (in exons 6 and 8), which is consistent with communications from Dr. Ganss that no AMTN protein can be detected in the *Amtn* null mice.

REFERENCES

Dos Santos Neves, J., Wazen, R.M., Kuroda, S., Francis Zalzal, S., Moffatt, P., and Nanci, A. (2012). Odontogenic ameloblast-associated and amelotin are novel basal lamina components. Histochem Cell Biol *137*, 329-338.

Iwasaki, K., Bajenova, E., Somogyi-Ganss, E., Miller, M., Nguyen, V., Nourkeyhani, H., Gao, Y., Wendel, M., and Ganss, B. (2005). Amelotin--a Novel Secreted, Ameloblast-specific Protein. J Dent Res *84*, 1127-1132.

Moffatt, P., Smith, C.E., St-Arnaud, R., Simmons, D., Wright, J.T., and Nanci, A. (2006). Cloning of rat amelotin and localization of the protein to the basal lamina of maturation stage ameloblasts and junctional epithelium. Biochem J *399*, 37-46.

Nishio, C., Wazen, R., Kuroda, S., Moffatt, P., and Nanci, A. (2010). Expression pattern of odontogenic ameloblast-associated and amelotin during formation and regeneration of the junctional epithelium. Eur Cell Mater *20*, 393-402.

Pindborg, J.J. (1953). The pigmentation of the rat incisor as an index of metabolic disturbances. Oral Surg Oral Med Oral Pathol *6*, 780-789.

Simmer, J.P., Hu, Y., Lertlam, R., Yamakoshi, Y., and Hu, J.C. (2009). Hypomaturation enamel defects in Klk4 knockout/LacZ knockin mice. J Biol Chem *284*, 19110-19121.

Simmer, J.P., Hu, Y., Richardson, A.S., Bartlett, J.D., and Hu, J.C. (2011a). Why does enamel in Klk4-null mice break above the dentino-enamel junction? Cells Tissues Organs *194*, 211-215.

Simmer, J.P., Richardson, A.S., Smith, C.E., Hu, Y., and Hu, J.C. (2011b). Expression of kallikrein-related peptidase 4 in dental and non-dental tissues. Eur J Oral Sci *119 Suppl 1*, 226-233.

Smith, C.E. (1998). Cellular and chemical events during enamel maturation. Crit Rev Oral Biol Med *9*, 128-161.

Smith, C.E., Hu, Y., Richardson, A.S., Bartlett, J.D., Hu, J.C., and Simmer, J.P. (2011a). Relationships between protein and mineral during enamel development in normal and genetically altered mice. Eur J Oral Sci *119 Suppl 1*, 125-135.

Smith, C.E., McKee, M.D., and Nanci, A. (1987). Cyclic induction and rapid movement of sequential waves of new smooth-ended ameloblast modulation bands in rat incisors as visualized by polychrome fluorescent labeling and GBHA-staining of maturing enamel. Adv Dent Res *1*, 162-175.

Smith, C.E., and Nanci, A. (1989). A method for sampling the stages of amelogenesis on mandibular rat incisors using the molars as a reference for dissection. Anat Rec *225*, 257-266.

Smith, C.E., Richardson, A.S., Hu, Y., Bartlett, J.D., Hu, J.C., and Simmer, J.P. (2011b). Effect of kallikrein 4 loss on enamel mineralization: comparison with mice lacking matrix metalloproteinase 20. J Biol Chem *286*, 18149-18160.

Somogyi-Ganss, E., Nakayama, Y., Iwasaki, K., Nakano, Y., Stolf, D., McKee, M.D., and Ganss, B. (2012). Comparative temporospatial expression profiling of murine amelotin protein during amelogenesis. Cells Tissues Organs *195*, 535-549.

Wen, X., and Paine, M.L. (2013). Iron deposition and ferritin heavy chain (Fth) localization in rodent teeth. BMC Res Notes *6*, 1.

CHAPTER 3

SCANNING AND BACKSCATTER ELECTRON MICROSCOPY

ABSTRACT

Ultrastructural analyses of mandibular incisors were conducted using scanning electron microscopy (SEM) and backscatter electron microscopy (BEI) to assess the thickness of the enamel layer, the decussation pattern of enamel rods, and enamel mineral density. Hemimandibles (n=3 per group) from *Amtn*$^{+/+}$*Klk4*$^{+/+}$, *Amtn*$^{+/+}$*Klk4*$^{-/-}$, *Amtn*$^{-/-}$*Klk4*$^{+/+}$, *Amtn*$^{+/-}$*Klk4*$^{+/-}$, and *Amtn*$^{-/-}$*Klk4*$^{-/-}$ mice were fractured through the mandibular incisors at the level of the alveolar crest and imaged by SEM, or embedded in resin, sectioned at the alveolar crest, and imaged by BEI. SEM fracture images at the alveolar crest showed that mice of all genotypes made enamel of full thickness and normal rod decussation. The enamel layers of *Amtn*$^{+/+}$*Klk4*$^{-/-}$ and *Amtn*$^{-/-}$*Klk4*$^{-/-}$ mice tended to shear off near the DEJ. The degree of enamel mineralization as determined by BEI was virtually identical in the *Amtn*$^{+/+}$*Klk4*$^{+/+}$, *Amtn*$^{-/-}$*Klk4*$^{+/+}$, *Amtn*$^{+/-}$*Klk4*$^{+/-}$ mice. In contrast, the degree of enamel mineralization in the *Amtn*$^{+/+}$*Klk4*$^{-/-}$ and *Amtn*$^{-/-}$*Klk4*$^{-/-}$ null animals was greatly reduced and decreased with depth. Enamel thickness was similar for all genotypes. These results demonstrate that enamel formation in the secretory stage is unaffected in the mutant mice, and that the observed enamel defects occur during the maturation stage.

INTRODUCTION

To understand how the absence of specific enamel proteins affects the formation of enamel, a variety of imaging techniques can be employed to study structural changes in the enamel layer. In this chapter, two such imaging techniques were used to study the thickness of the enamel layer, the decussation pattern formed by the enamel rods, and the mineral density of the samples. Such results can be used to determine at which point in amelogenesis the missing protein might normally be involved.

As noted in Chapter 1, amelogenesis proceeds in two principle stages: secretory and maturation stage (Smith, 1998; Smith and Nanci, 1989). During the secretory stage, the entire thickness of the enamel layer is established, as is the decussation pattern of enamel rods, so absence of a protein that serves an important, non-redundant function during the secretory stage is expected to cause the enamel layer to be thinner than normal and have an aberrant decussation pattern of enamel rods. During the maturation stage the enamel layer reaches its final mineral density (Smith and Nanci, 1995), so if a protein is normally involved in this stage, but is missing, a hypomineralized enamel layer will likely result. Therefore, enamel imaging can be used to help guide the answers to the question of how and when a protein might be involved in amelogenesis and has been previously employed to do so (Hu et al., 2011; Shin et al., 2014; Simmer et al., 2011).

The two techniques used in this chapter are scanning electron microscopy (SEM) and backscatter electron imaging (BEI). The SEM scope detects electrons that directly bounce off of the sample to obtain a three dimensional image and requires that the sample be coated with a conductive element such as gold-palladium (Sousa and Kruhlak, 2013). This prevents the accumulation of static charges created by the electron beam, which would interfere with obtaining a high quality image. BEI, on the other hand, takes advantage of backscattered electrons that are elastically deflected off a polished and carbon coated sample from the main electron beam and sensed by a backscatter detector placed near the beam source (Dingley, 2004; Sousa and Kruhlak, 2013). Therefore, larger atoms in the sample will deflect more electrons which are then detected by the sensor creating a grayscale image ranging from white for higher atomic density to black for lower atomic density (Dingley, 2004). In mineralized tissue samples, bright white areas tend to contain large amounts of calcium. Therefore, fully mineralized enamel generally appears white, dentin and bone are variations of gray, and resin is dark gray to black in the image. BEI has previously been used in the enamel field to study in high detail the amount of mineral present in the enamel layer across different strains of mice (Hu et al., 2011; Shin et al., 2014). The images obtained with BEI can be pseudo-colorized using ImageJ (version 1.48, http://imagej.nih.gov/ij/), the free image analysis program offered by NIH. The colors can be assigned based on gray value and the resulting image serves as an easy way to visualize changes in mineral

density across the enamel layer. This was done in previous studies to more clearly show changes in enamel resulting from knocking out a variety of genes encode enamel-specific proteins (Hu et al., 2011; Shin et al., 2014; Smith et al., 2011). The methods used for fractured incisors were modeled from previous studies (Simmer et al., 2009).

There are a few potential sources of error with these techniques, particularly with BEI. It is critical for BEI images that a sample be very well polished. Any areas of roughness will appear darker in the image and appear hypomineralized. This problem was more common with areas of bone and dentin, and thus images in which this occurs cannot be used to adequately analyze relative mineralization since the dentin was used to normalize other readings of the samples. In addition, the dehydration and plastic infiltration required for processing the sample for BEI imaging often leads to cracking of the sample. While a few cracks do not interfere with overall imaging analysis, if the sample shows severe cracking or damage, it becomes difficult to adequately analyze the sample due to the damage. For the SEM fracture images, the main source of artifacts was a smear layer found on the outer enamel created when the fracture was made. To create the fracture, incisors were notched in dentin on the concave portion of the tooth. The two ends of the incisor were then bent outwards, causing the fracture to propagate along the dentin and enamel. This can lead to compression of the outer enamel layer resulting in a smear layer which obscures the enamel crystal pattern, so care is required to ensure that a clean fracture is obtained for better imaging of the sample.

MATERIALS AND METHODS

Scanning Electron Microscopy – Fractured Incisors

7-week old *Amtn*$^{+/+}$*Klk4*$^{+/+}$, *Amtn*$^{+/+}$*Klk4*$^{-/-}$, *Amtn*$^{-/-}$*Klk4*$^{+/+}$, *Amtn*$^{+/-}$*Klk4*$^{+/-}$, and *Amtn*$^{-/-}$*Klk4*$^{-/-}$ mice were anesthetized with isofluorane. The mandibles were removed and split at the mental symphysis, and the soft tissue was removed with a dental scaler. Each hemimandible was dehydrated with a series of graded ethanol (30 min each of 30%, 50%, 70%, 80%, 90%, 100% x 2), air dried, and fractured at the level of the alveolar crest. To create the fracture, incisors were notched in dentin on the concave portion of the tooth. The two ends of the incisor were then bent outwards, causing the fracture to propagate along the dentin and enamel. Fractured incisors were mounted on metallic stubs using conductive carbon tape and sputter coated with an Au-Pd film. Samples were imaged at the University of Michigan Microscopy and Imaging Analysis Laboratory (Ann Arbor, MI, USA) using an Amray EF 1910 Scanning Electron Microscope operating at an accelerating voltage of 5 kV.

Backscatter Electron Microscopy (BEI)

The contralateral hemimandible was cleaned of soft tissue and embedded in Epon resin (EMbed812 cat#14120, Electron Microscopy Sciences, Hatfield, PA) following graded acetone dehydration (30%, 50%, 70%, 80%, 90%, 95%, 100% x 2 for 30 min each). After polymerization at 65 ˚C, the incisors were cut transversely (cross-section) with a model 650 low speed diamond wheel saw (South Bay Technology Inc., San Clemente, CA) at

the level of the crest of the alveolar bone close to where the incisor erupts into the mouth, about 8 mm from the apex of the incisor. The sectioned hemimandibles were then re-embedded in Castolite AC (Eager polymers, Chicago, IL, USA) using 25-mm SteriForm molds (Struers Inc., Westlake, OH) with the cutting plane face down and allowed to harden overnight. The transversely sectioned faces of the mandibular incisors were polished sequentially with a syntron polisher on 400, 800, and 1200 grit waterproof silicon carbide papers followed by 1 μm diamond polishing paste (South Bay Technology Inc., San Clemente, CA). Surfaces were carbon coated for backscatter SEM. The polished surfaces were examined at various magnifications in a CAMECA SX-100 electron microprobe analyzer using the backscatter mode at 15 kV and a calibration wedge to ensure that the range of intensities in each image recorded spanned a similar range of gray level intensities. The calibration wedge was based on a 0-255 pixel shade range where pure white is 255 and pure black is 0. The wild-type enamel was set at 190, dentin and bone at 160, and Epon resin at 40. Pseudo-colored image mapping was done using ImageJ on Tiff images that were normalized to have the same mean gray level intensities for mineralized dentin, given that dentin and bone show no significant changes. For pseudo-colored images, gray levels 1-30 were assigned as black, 31-75 as white, 76-173 as blue, and 174-255 as red. These settings were saved in a look-up table (LUT) as described previously (Shin et al., 2014) and applied to the selected BEI images.

RESULTS

Mandibular incisors were fractured at the level of the alveolar crest to study fully matured enamel structure in an area that had not been damaged by masticatory function. Low magnification images taken at 200X showed that in all genotypes, the full thickness of enamel had been secreted from the DEJ to the enamel surface (Fig. 3.1). Normal rod decussation patterns were also observed in all mice (Fig. 3.2). These observations confirm that the secretory stage proceeds normally in these mice, given that enamel thickness and decussation patterns are established during the secretory stage when the crystals are growing in length (Smith, 1998). Therefore the enamel defects observed in these mice originated during the maturation stage. In *Amtn*$^{-/-}$*Klk4*$^{-/-}$ and *Amtn*$^{+/+}$*Klk4*$^{-/-}$ mice, the enamel layer frequently delaminated from the underlying dentin, similar to findings from previous studies (Simmer et al., 2011).

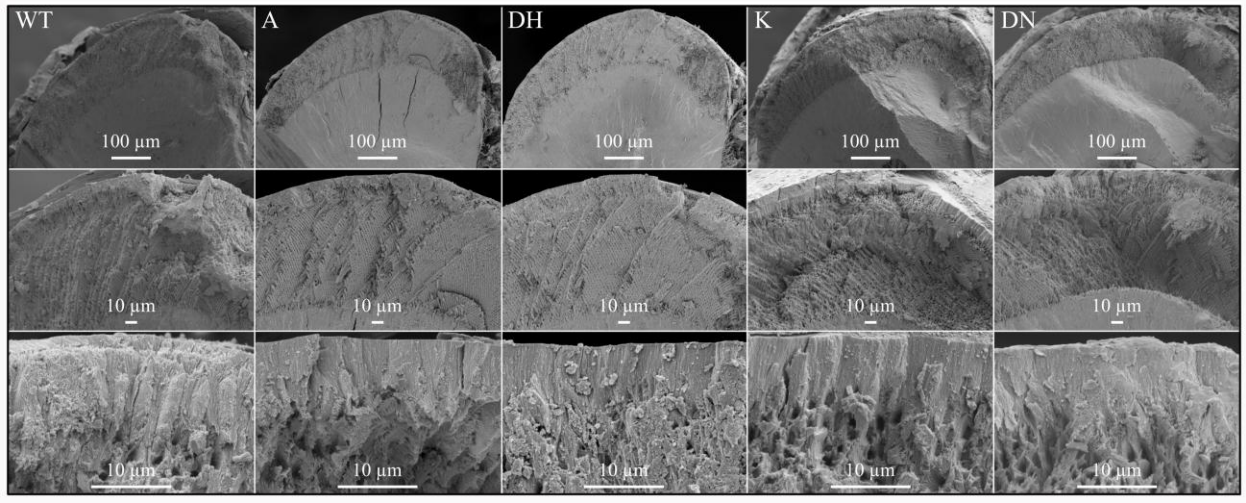

Fig. 3.1. Enamel thickness and rod decussation. Fractured incisors from wild-type (WT), *Amtn*-null (A), *Klk4*-null, and *Amtn*/*Klk4*-null animals were imaged at 200X, 500X, and 4,000X magnification. The enamel thickness at the alveolar crest and decussation of the enamel rods were compared, and all samples were found to have normal thickness and rod decussation.

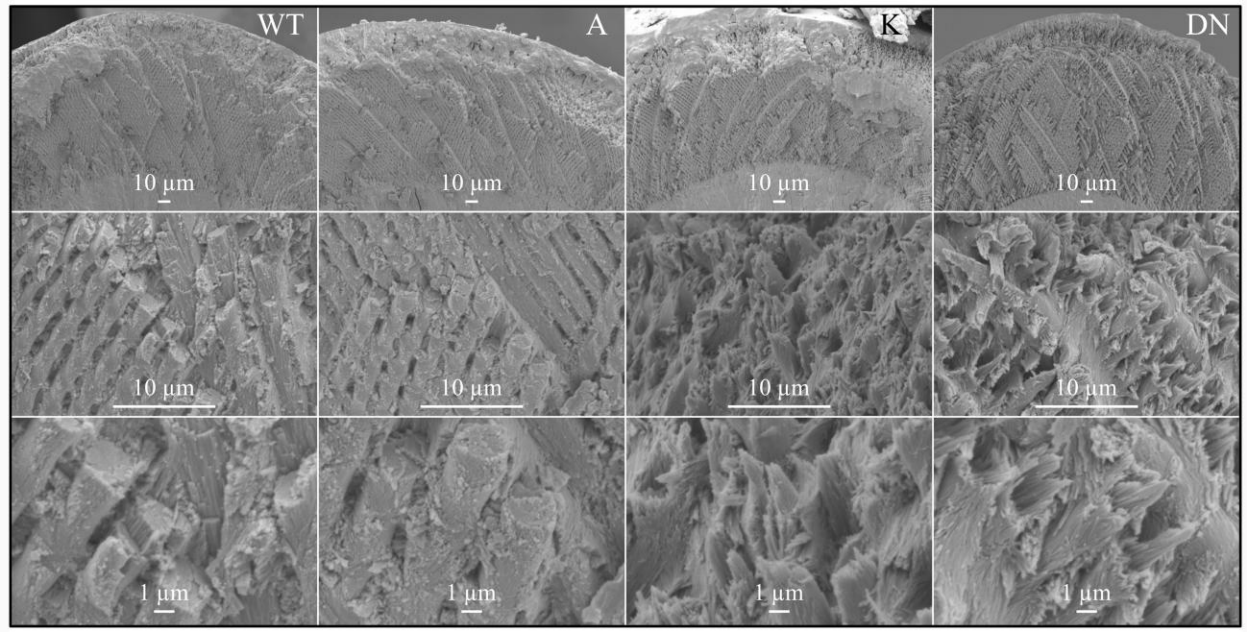

Fig. 3.2. Rod decussation. Fractured incisors from wild-type (WT), *Amtn*-null (A), *Klk4*-null (K), and *Amtn*/*Klk4*-null (DN) animals were imaged at 500X, 4,000X, and 10,000X magnification.. All groups showed a normal decussation pattern and normal enamel thickness. The crystallites in wild-type and *Amtn*-null samples were tightly packed and well organized within each rod. Crystallites in *Klk4*-null and *Amtn*/*Klk4*-null samples, however, were loosely bundled with some of the crystallites falling out of the rod structure and fracturing at irregular angles due to the presence of retained protein matrix.

In wild-type and *Amtn*-null mice, the enamel crystallites are packed tightly into rod and inter-rod enamel, but in the *Klk4*-null and *Amtn*/*Klk4*-null mice the enamel crystallites were loosely bundled and had a tendency to spill out of the enamel similar to previous studies of the *Klk4*-null mouse (Simmer et al., 2009). Imaging at high magnification was unable to detect any apparent difference between wild-type and *Amtn*-null nor the *Klk4*-null and *Amtn*/*Klk4*-null animals.

The principle of backscatter relies on electrons rebounding off atoms of higher atomic number, therefore, the more mineralized the enamel layer, the more calcium is present to deflect these electrons. To characterize the degree of mineralization for each

of the genotypes, we performed BEI. The gray value of the images was adjusted based on the density of dentin, which did not vary between genotypes and had similar hardness in all genotypes (see Chapter 5). ImageJ was used to create a LUT to assign different colors based on five different ranges of gray level intensity (Shin et al., 2014). Based on the LUT used in the analysis, the red represents tissue that was the most highly mineralized while the blue represents tissue that was less mineralized. In this type of imaging, the wild-type, *Amtn*-null, and *Amtn*/*Klk4*-heterozygote mice were similar and indistinguishable from each other. The *Klk4*-null and *Amtn*/*Klk4*-null mice showed significantly decreased mineralization in the enamel layer, as highlighted by the pseudocolored blue pixels (Fig. 3.3).

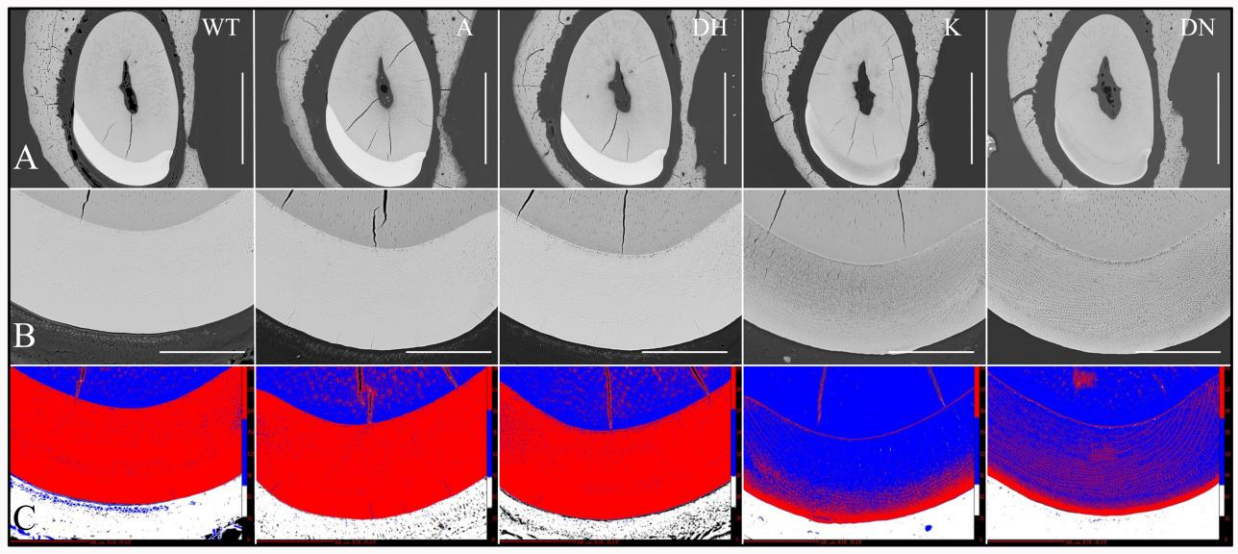

Fig. 3.3. BEI analyses of incisor cross-sections at the level of the alveolar crest. Incisors were sampled about 8 mm from the apex. From left to right are wild-type (WT), *Amtn*-null (A), *Amtn*/*Klk4*-heterozygous (DH), *Klk4*-null (K), *Amtn*/*Klk4*-null (DN). In the black and white sections, white is highly mineralized, black is unmineralized. ***A:*** Incisor cross-sections sampled at the alveolar crest; Bar = 500 μm. ***B:*** Centro-mesial section of the enamel layer; Bar = 100 μm. These images were used to measure enamel thickness. ***C:*** Pseudocolorized images of sections in row B, using ImageJ. Red is above threshold mineralized tissue and blue is below threshold mineralized tissue.

The same BEI images were also used to quantify enamel thickness across samples from all genotypes. The thickest point of enamel at the centro-mesial side of the incisor cross section was used for all images. ImageJ was calibrated using the magnification bar provided by the CAMECA and n=5 images from each genotype were included in the analysis. A line was drawn extending from the outer enamel surface to the DEJ, values were averaged for each genotype, and standard deviations were obtained using SPSS. Data was displayed in Fig. 3.4. No significant difference in enamel thickness was found (*t*-test, $p>0.05$) between any of the genotypes. The average enamel thickness values (in μm) for the five genotypes were: *Amtn*$^{+/+}$*Klk4*$^{+/+}$, 115.02 ± 2.64; *Amtn*$^{+/+}$*Klk4*$^{-/-}$, 113.24 ± 4.85; *Amtn*$^{-/-}$*Klk4*$^{+/+}$, 117.92 ± 2.91; *Amtn*$^{+/-}$*Klk4*$^{+/-}$, 116.42 ± 3.08; *Amtn*$^{-/-}$*Klk4*$^{-/-}$ 112.80 ± 2.81. These findings are consistent with previous observations of AMTN and KLK4 expression specifically by maturation stage ameloblasts (Iwasaki et al., 2005; Moffatt et al., 2006b; Somogyi-Ganss et al., 2012) and enamel thickness being established during the secretory stage of amelogenesis.

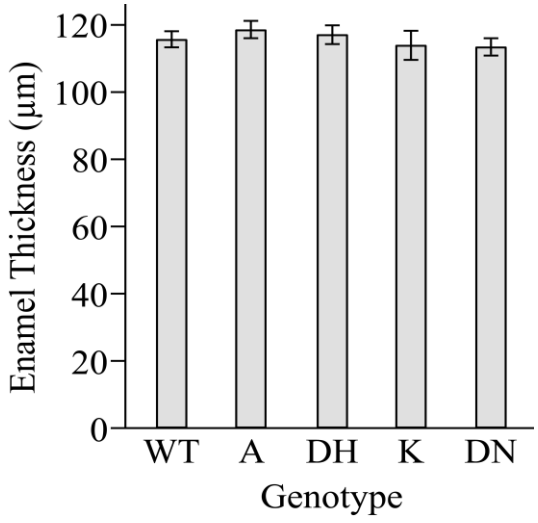

Fig. 3.4. Incisor enamel thickness measurements at alveolar crest from BEI. Thickness measurements were obtained from BEI images taken at the alveolar crest at the widest point at the centro-mesial side of the incisor using ImageJ. Values were averaged and standard deviation was obtained for n=5 animals per genotype. A paired *t*-test revealed no significant difference between any groups ($p>0.05$). Wild-type (WT), *Amtn*-null (A), *Klk4*-null (K), *Amtn*/*Klk4*-hetero-zygote (DH), and *Amtn*/*Klk4*-null (DN).

DISCUSSION

These studies focused on using SEM and BEI to analyze enamel thickness, rod decussation pattern, and relative mineralization among the 5 mouse genotypes. SEM allowed for comparison of ultrastructural details across genotypes through fractured incisors, and BEI allowed for a relative comparison of mineralization in the enamel layer. Enamel was studied at the alveolar crest, prior to eruption so that the enamel was not yet affected by masticatory function.

SEM fracture images were obtained by removing the erupted portion of the incisor to visualize mature enamel by making a notch in the dentin with a rotating disk and bending the two portions of the incisor on either side of the notch. Imaging of the fractured surface showed that the full thickness of enamel was present in all genotypes along with normal rod decussation patterns indicating that the secretory stage of amelogenesis was unaffected. Additionally, enamel in *Klk4*-null and *Amtn*/*Klk4*-null mice tended to fracture near the DEJ. The outer enamel in all genotypes at high magnification appeared similarly organized. Also at high magnification, rod structure in wild-type and *Amtn*-null mice was comparable. If there existed any differences, they could not be differentiated with this type of imaging. Rods were well organized and very compact, and the end of the rods broke off in a smooth plane. In contrast, rod structure in *Klk4*-null and *Amtn*/*Klk4*-null mice was less compact and had a tendency to shear off at odd, rough angles. Individual crystallites could also be observed at this

magnification, given that there exists retained matrix proteins preventing full maturation from occurring. Since the *Klk4*-null enamel could not be distinguished from the *Amtn*/*Klk4*-null enamel, and since the *Amtn*-null enamel was very similar to wild-type enamel, it is likely that the observed maturation defect in the double null animals was primarily due to the lack of KLK4 in the enamel. Since KLK4 and AMTN have been clearly established as maturation stage, ameloblast-specific proteins (Moffatt et al., 2006a; Moffatt et al., 2006b; Simmer et al., 2009), it is not surprising that in the absence of AMTN the secretory stage enamel is likely unaffected, given that the defects observed in null mice are consistent with defects in the maturation stage.

BEI images were used to study the amount of mineralization in the enamel layer among the different genotypes that were studied. Hemi-mandibles from perfused mice were embedded in resin, sectioned at the alveolar crest, and polished for BEI analysis. BEI images were equalized based on gray levels of the dentin layer, given that the dentin was unaffected in the mutant mice and among all genotypes showed similar morphology and hardness (see data in Chapter 5). Enamel mineralization was compared between the five groups of animals. This technique was unable to distinguish between wild-type, *Amtn*-null, and *Amtn*/*Klk4*-heterozygote animals. *Klk4*-null and *Amtn*/*Klk4*-null enamel was significantly less mineralized than that of the previous group but difficult to distinguish between each other. Again, given the similarity of the

wild-type and *Amtn*-null mice, it is likely that defects in the *Amtn*/*Klk4*-null animals are primarily being caused by the lack of KLK4.

Enamel thickness measurements were taken with BEI images as well. The thickest point was measured in the cross sectional images on the centro-mesial side of the incisor from the outer enamel to the DEJ. ImageJ was used to obtain the individual measurements (Fig. 3.4) for n=5 mice per genotype which were used to calculate an average value and standard deviation. Consistent with the fracture images, there was no significant quantitative difference in thickness between genotypes, again suggesting that the secretory stage was unaffected, and that evident enamel defects might have resulted from maturation stage pathology.

In summary, we performed SEM and BEI studies to characterize and compare the enamel of the 5 genotypes. We specifically examined fractured mandibular incisors at the level of the alveolar ridge. At this location, the enamel is virtually done developing and is about to erupt into function. It hasn't, however, yet entered the oral cavity and been disturbed or altered by masticatory forces. The results show that the enamel layers of all 5 genotypes have normal rod decussation patterns. The enamel thickness is also normal (~115 μm). These parameters are fixed during the secretory stage, and are consistent with AMTN and KLK4 being specific for the later, maturation stage of amelogenesis. We were not able to detect any differences in the degree of enamel mineralization between the *Amtn* null and the wild-type mice; however, the

enamel of the *Amtn*$^{-/-}$*Klk4*$^{-/-}$ (double null) appeared to be somewhat less mineralized than the enamel of *Klk4* single null (*Amtn*$^{+/+}$*Klk4*$^{-/-}$) mice.

REFERENCES

Baptista, A., Kato, I.T., Prates, R.A., Suzuki, L.C., Raele, M.P., Freitas, A.Z., and Ribeiro, M.S. Antimicrobial photodynamic therapy as a strategy to arrest enamel demineralization: a short-term study on incipient caries in a rat model. Photochem Photobiol *88*, 584-589.

Dingley, D. (2004). Progressive steps in the development of electron backscatter diffraction and orientation imaging microscopy. J Microsc *213*, 214-224.

Hu, Y., Hu, J.C., Smith, C.E., Bartlett, J.D., and Simmer, J.P. (2011). Kallikrein-related peptidase 4, matrix metalloproteinase 20, and the maturation of murine and porcine enamel. Eur J Oral Sci *119 Suppl 1*, 217-225.

Iwasaki, K., Bajenova, E., Somogyi-Ganss, E., Miller, M., Nguyen, V., Nourkeyhani, H., Gao, Y., Wendel, M., and Ganss, B. (2005). Amelotin--a Novel Secreted, Ameloblast-specific Protein. J Dent Res *84*, 1127-1132.

Moffatt, P., Smith, C.E., Sooknanan, R., St-Arnaud, R., and Nanci, A. (2006a). Identification of secreted and membrane proteins in the rat incisor enamel organ using a signal-trap screening approach. Eur J Oral Sci *114 Suppl 1*, 139-146; discussion 164-135, 380-131.

Moffatt, P., Smith, C.E., St-Arnaud, R., Simmons, D., Wright, J.T., and Nanci, A. (2006b). Cloning of rat amelotin and localization of the protein to the basal lamina of maturation stage ameloblasts and junctional epithelium. Biochem J *399*, 37-46.

Shin, M., Hu, Y., Tye, C.E., Guan, X., Deagle, C.C., Antone, J.V., Smith, C.E., Simmer, J.P., and Bartlett, J.D. (2014). Matrix Metalloproteinase-20 Over-Expression Is Detrimental to Enamel Development: A Mus musculus Model. PLoS One *9*, e86774.

Shoaee, S., Ghasemian, A., Najafi, B., Kasaeian, A., Farzadfar, F., and Hessari, H. National and Sub-national Burden of Oral Diseases in Iran: 1990 - 2013, Study Protocol. Arch Iran Med *17*, 159-168.

Simmer, J.P., Hu, Y., Lertlam, R., Yamakoshi, Y., and Hu, J.C. (2009). Hypomaturation enamel defects in Klk4 knockout/LacZ knockin mice. J Biol Chem *284*, 19110-19121.

Simmer, J.P., Hu, Y., Richardson, A.S., Bartlett, J.D., and Hu, J.C. (2011). Why does enamel in Klk4-null mice break above the dentino-enamel junction? Cells Tissues Organs *194*, 211-215.

Smith, C.E. (1998). Cellular and chemical events during enamel maturation. Crit Rev Oral Biol Med *9*, 128-161.

Smith, C.E., and Nanci, A. (1989). A method for sampling the stages of amelogenesis on mandibular rat incisors using the molars as a reference for dissection. Anat Rec *225*, 257-266.

Smith, C.E., and Nanci, A. (1995). Overview of morphological changes in enamel organ cells associated with major events in amelogenesis. Int J Dev Biol *39*, 153-161.

Smith, C.E., Richardson, A.S., Hu, Y., Bartlett, J.D., Hu, J.C., and Simmer, J.P. (2011). Effect of kallikrein 4 loss on enamel mineralization: comparison with mice lacking matrix metalloproteinase 20. J Biol Chem *286*, 18149-18160.

Somogyi-Ganss, E., Nakayama, Y., Iwasaki, K., Nakano, Y., Stolf, D., McKee, M.D., and Ganss, B. (2012). Comparative temporospatial expression profiling of murine amelotin protein during amelogenesis. Cells Tissues Organs *195*, 535-549.

Sousa, A.A., and Kruhlak, M.J. (2013). Introduction: nanoimaging techniques in biology. Methods Mol Biol *950*, 1-10.

CHAPTER 4

MICRO-COMPUTED TOMOGRAPHY OF MANDIBULAR INCISOR ENAMEL

ABSTRACT

We hypothesized that enamel mineral density at the maturation stage differs between wild-type and *Amtn*-null mice as well as *Klk4*-null and *Amtn*/*Klk4*-null mice. High-resolution micro-computed tomography (micro-CT) was performed on hemimandibles of selected genotypes. A total of 12 mice (3 per genotype) were quantitatively assessed, in the presence of a density standard, to determine if there was a difference in enamel mineral density between selected groups of different genotypes. Micro-CT analysis demonstrated no significant difference of the enamel density of incisor cross sections taken at the maturation stage between wild-type and *Amtn*-null or *Klk4*-null and *Amtn*/*Klk4*-null mice. An important finding was that enamel maturation is delayed in the Amtn-null mice relative to the wild-type.

INTRODUCTION

Micro-CT has been used over the past few decades as a qualitative measure to look at hard tissue morphology without any damage to the sample being studied. The first micro-CT units were developed in the 1980s using bench-top x-ray sources

(Kujoory et al., 1980; Sato et al., 1981) and were established as a qualitative way to study the structure of cancellous bone (Layton et al., 1988; Odgaard et al., 1990; Peyrin et al., 1993). Since then, its capabilities have increased significantly, specifically in resolution and scanning times. The non-destructive analysis of samples of various sizes makes micro-CT useful for the study of biological samples.

Micro-CT relies on measuring the difference in x-ray intensity before and after passing through the sample by taking a series of two dimensional radiographs, or projections, by rotating the sample as a beam is passed through it (Ritman, 2004). This difference in x-ray attenuation as it passes through the sample correlates with the density of the sample (Fajardo et al., 2002) which can then be assigned a measurable gray-scale value. Final resolution of each projection can be controlled by adjusting the number of projections taken, the angular coverage of the projections, and manipulating the voltage and current of the x-ray source (Fajardo et al., 2002; Wise et al., 2013). These individual projections are then compiled, or reconstructed, into a final three dimensional image that can be digitally manipulated (Fajardo et al., 2002; Zou et al., 2011).

With the advent and increased use of known-density mineral standards, it is now also possible to use micro-CT to quantitatively analyze mineral density in tissue samples (Burghardt et al., 2008; Fajardo et al., 2009; Fajardo et al., 2002; Inness et al., 2014). Using a series of known-density mineral phantoms, it is possible to generate a

linear relationship between mineral density and gray levels, since the attenuation of the x-ray beam is affected by the density of the sample (Huang et al., 2007; Zou et al., 2011). This is referred to as a standardized linear attenuation curve (LAC), which allows for each pixel of the sample in question to be assigned a specific gray-scale value and compared to the LAC to precisely obtain the sample's mineral density. Materials for phantoms have ranged from dipotassium hydrogen phosphate (K_2HPO_4) (Nuzzo et al., 2002; Schweizer et al., 2007), to aluminum (Elliott et al., 1998; Nazarian et al., 2008), to even potassium pyrophosphate ($K_2P_4O_7$) (Sanada et al., 1999). More recently, the use of hydroxyapatite resin phantoms have become more routine. A commonly used example is the phantom set manufactured by Scanco Medical that consists of a cylinder with 5 inserts of different densities (0, 200, 400, 500, and 800 mg/cm^3) of hydroxyapatite particles suspended in poly-methyl methacrylate resin to mimic the surrounding soft tissue (Burghardt et al., 2008; Cheng et al., 2000; Chueh et al., 2006; Nuzzo et al., 2002). Similar types of phantoms are made by SkyScan (Bruker SkyScan, Aartselaar, Belgium), where very fine hydroxyapatite powder is embedded in epoxy to produce hydroxyapatite discs with mineral density ranges from 50-750 mg/cm^3 (Zou et al., 2011). One of the main potential sources of calibration error in these phantoms, however, is that many biologic mineralized tissues have densities exceed the range of existing phantoms and thus calibration curves often have to be extrapolated (Bronckers et al., 2013; Burghardt et al., 2008) to estimate the mineral density of test samples, mainly due

to the difficulty of manufacturing homogenous high-density hydroxyapatite-resin mixtures (Zou et al., 2011). Recently, however, the advent of high mineral density phantoms has made it possible to directly obtain these measurements, particularly for high mineral density tissues such as enamel (Huang et al., 2007; Schmitz et al., 2014; Schweizer et al., 2007).

In the enamel field, mineral density has historically been analyzed by micro-dissection (Weidmann et al., 1967) and subsequently by strip dissection and ashing analysis, but these methods are extremely labor intensive, destructive to the samples, and technique sensitive (Robinson et al., 1977; Smith and Nanci, 1989). Ashing of mineral strips involves lifting 1-mm strips along the entire length of the incisor, spanning from the secretory to the maturation stages (Smith and Nanci, 1989). Pooled strips of the same developmental stage are weighed before and after being subjected to extremely high temperatures for specific amounts of time resulting in an ashed sample. The difference in weight is then calculated to derive the mineral and non-mineral content of the samples (Smith et al., 2009). Due to the technique sensitivity of this method, results are difficult to reproduce between investigators. In addition, this method results in destruction of the sample. Recent studies have used phantoms of defined densities in conjunction with micro-CT analysis to demonstrate a less time-consuming alternative that can consistently and quantitatively measure the same aspects without destruction of the sample (Bronckers et al., 2013; Schmitz et al., 2014).

Standard phantoms used in micro-CT are generally of lower density than that of enamel, as stated above. Therefore, the key to quantitatively study enamel by micro-CT is the use of a high mineral density phantom 2.927 g/cm^3 that was higher than the density of enamel found in wild-type samples (2.9 g/cm^3) (Schmitz et al., 2014; Schweizer et al., 2007). Previously, these high-density phantoms were not available due to the difficulty of manufacturing them. The high-density phantom, being primarily made of mineral, requires specialized equipment that can bond the crystals using high heat and pressure (Schweizer et al., 2007). The development of this high density phantom now allows for valid quantitative measurements of high mineral content samples such as enamel (Schmitz et al., 2014). With the use of this high density phantom in conjunction with micro-CT, it has been shown that this method of analysis highly correlates with previous ashing results (Schmitz et al., 2014; Smith et al., 2009) and was able to reproducibly correlate volume, mineral weight, and most importantly, mineral density using micro-CT technology (Schmitz et al., 2014).

MATERIALS AND METHODS

Mice of 4 different genotypes (wild-type, *Amtn*-null, *Klk4*-null, and *Amtn*/*Klk4*-null, n=3 of each) were used for this analysis. Mice were anesthetized with isofluorane and euthanized by intracardiac perfusion using 5% glutaraldehyde in 0.8M sodium cacodylate with 0.05% calcium chloride, pH 7.4. Hemimandibles were removed and

dissected of soft tissue, washed in 1X-PBS, placed in a vial and immersed in 70% ethanol. Samples were scanned in a SkyScan 1172 (Bruker SkyScan, Aartselaar, Belgium) system. Each specimen was positioned inside of the scanning tube with the ramus inferiorly and incisal tip superiorly positioned and supported with agarose. The tube was sealed with Parafilm (American National Can, Greenwich, CT USA). Samples were scanned at 60 kV, 167 uA beam intensity, 0.7° rotation step, 4 frame average, 2000 x 1336 CCD, 700-millisecond exposure and 5-μm voxel size. Scan time was 35 min per entire hemimandible. The images were reconstructed with NRecon (Bruker SkyScan, Aartselaar, Belgium) with a Feldkamp cone-beam algorithm (Rodet et al., 2004). HA phantoms 0.25 and 0.75 g/cm^3 (SkyScan), and 2.927 g/cm^3 (Himed, Bethpage, NY, USA) were used for calibration prior to mineral density analyses.

The scanned area was chosen as the first section where the incisor is fully surrounded by alveolar bone, about 7.5 mm from the apex of the incisor. The volume of interest (VOI) started 10 slices distally from where the enamel is fully enclosed in bone (Fig. 4.1). The VOI continued distally for 1.0 mm (about 200 slices) (Fig 4.2). The enamel tissue was then isolated manually based on density (Fig 4.3). The manual tracing (appearing in red, but turning light blue when laid over high density areas of enamel) followed the DEJ and was then refined to exclude any areas that were not enamel, such as the air space next to the outer enamel surface. Prior to analysis, images were reoriented by aligning the image along the length of the incisor (Fig. 4.4). The incisor

was aligned along its length as straight as possible, given that the incisor tends to curve in two different dimensions (Fig. 4.4, top left). The cross-section of the incisor was also used to align it vertically along the midline of the incisor (Fig. 4.4, bottom left).

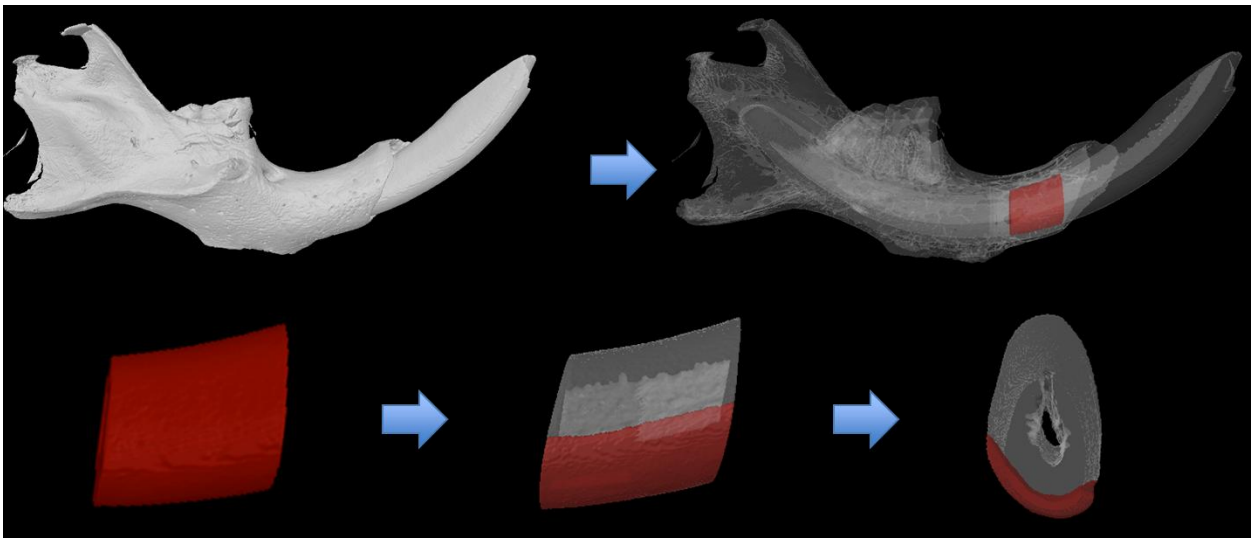

Fig. 4.1. Choosing the Volume of Interest (VOI, red). The scanned area was chosen as the first section where the incisor is fully surrounded by alveolar bone, about 7.5-millimeters from the apex of the incisor. The VOI started 10 slices distally from where the enamel is fully enclosed in bone and continued distally for 1.0 mm (about 200 slices total).

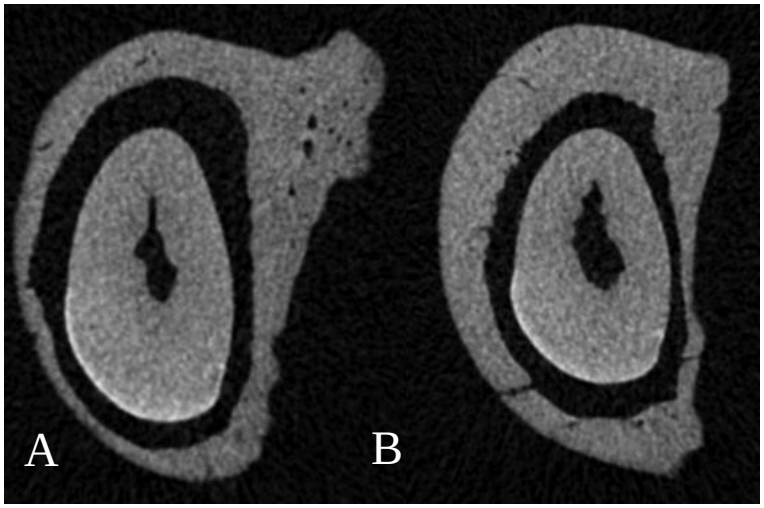

Fig. 4.2. Beginning and end of Volume of Interest (VOI). The scanned area was chosen as the first section where the incisor is fully surrounded by alveolar bone, about 7.5-millimeters from the apex of the incisor (A). The VOI ended about 1.0 mm from the first slice included in the VOI (B).

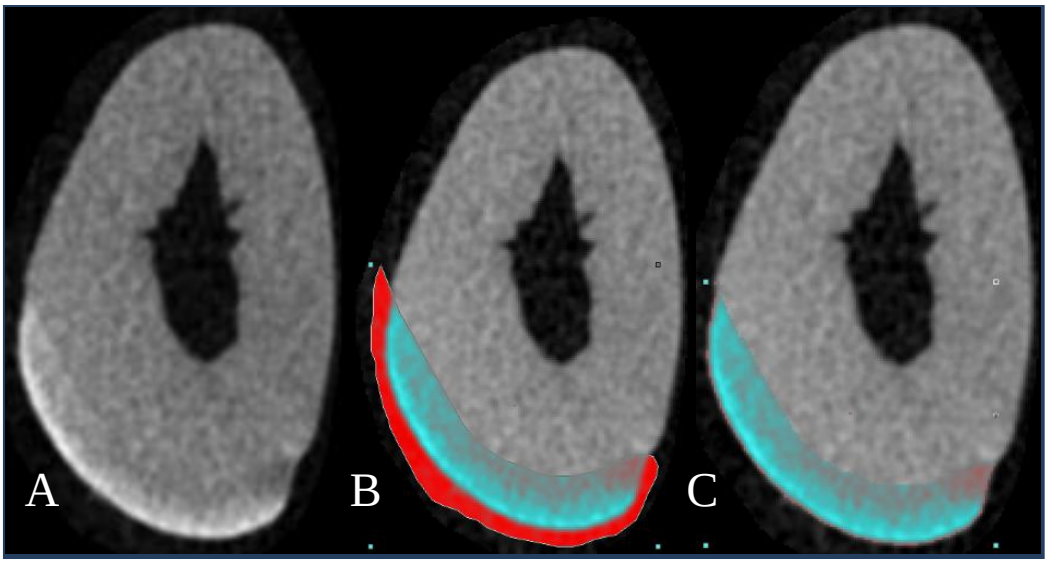

Fig. 4.3. Manual isolation of the enamel layer. ***A:*** Cross sectional image of the mouse incisor. ***B:*** Manual tracing including the entire enamel layer, following the DEJ. The tracing appears red, but when it is laid over enamel it changes to a light blue color. ***C:*** Refined manual tracing excluding any non-enamel areas such as air space.

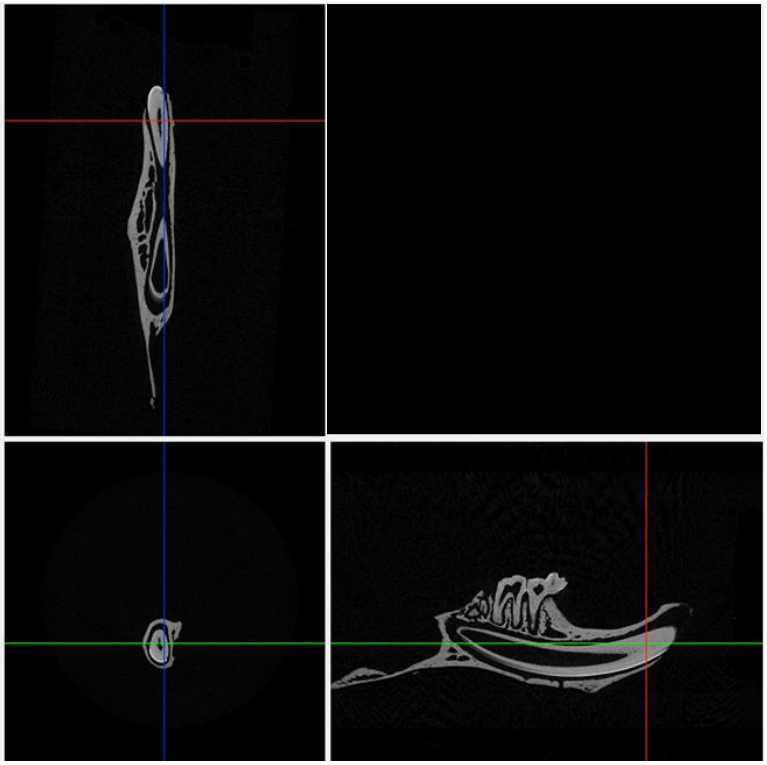

Fig. 4.4. Reorientation of images on the analysis software. Prior to analysis, images were reoriented by aligning the image along the length of the incisor trying to accommodate for the curvature of the incisor in two different dimensions (top, left) and aligning the cross section of the incisor to vertical by using the midline (bottom, left).

Image J Analysis of Maximum Intensity Projections

Maximum intensity projections (MIPs), which are 2D images constructed from the original 3D scan, were obtained for the analyzed mice. A 40x50 pixel box (2000 pixels squared) was placed over the enamel layer, half-way between the mesial root of the second molar and the distal root of the first molar, since this area correlates with the early maturation stage. Average gray value in the yellow box in between the first and second molar was measured using ImageJ (version 1.48, http://imagej.nih.gov/ij/). Those values were averaged for each genotype, and statistically analyzed using a Student's *t*-test.

RESULTS

In this study we used micro-CT to obtain a quantitative analysis of enamel mineral density in wild-type, *Amtn*-null, *Klk4*-null, and *Amtn*/*Klk4*-null mice (n=3 hemi-mandibles per group) by using known-density phantoms to obtain a linear attenuation curve (LAC) that was used to assign mineral density values to the scanned samples based on gray-scale values. The threshold used for morphological analysis was lower than usual studies on enamel. This was because the *Klk4*-null and *Amtn*/*Klk4*-null samples were analyzed first to see if they could be differentiated with this analysis, so

the threshold determined from that experiment was used across all samples for more accurate comparison. This partially explains the observed standard deviations.

The total amount of enamel volume analyzed in all samples was similar (*t*-test, $p>0.05$) (Fig. 4.5). Given that enamel thickness is similar in all animals (Ch. 3), it would be expected that a comparable VOI analyzed for micro-CT would include similar enamel volumes.

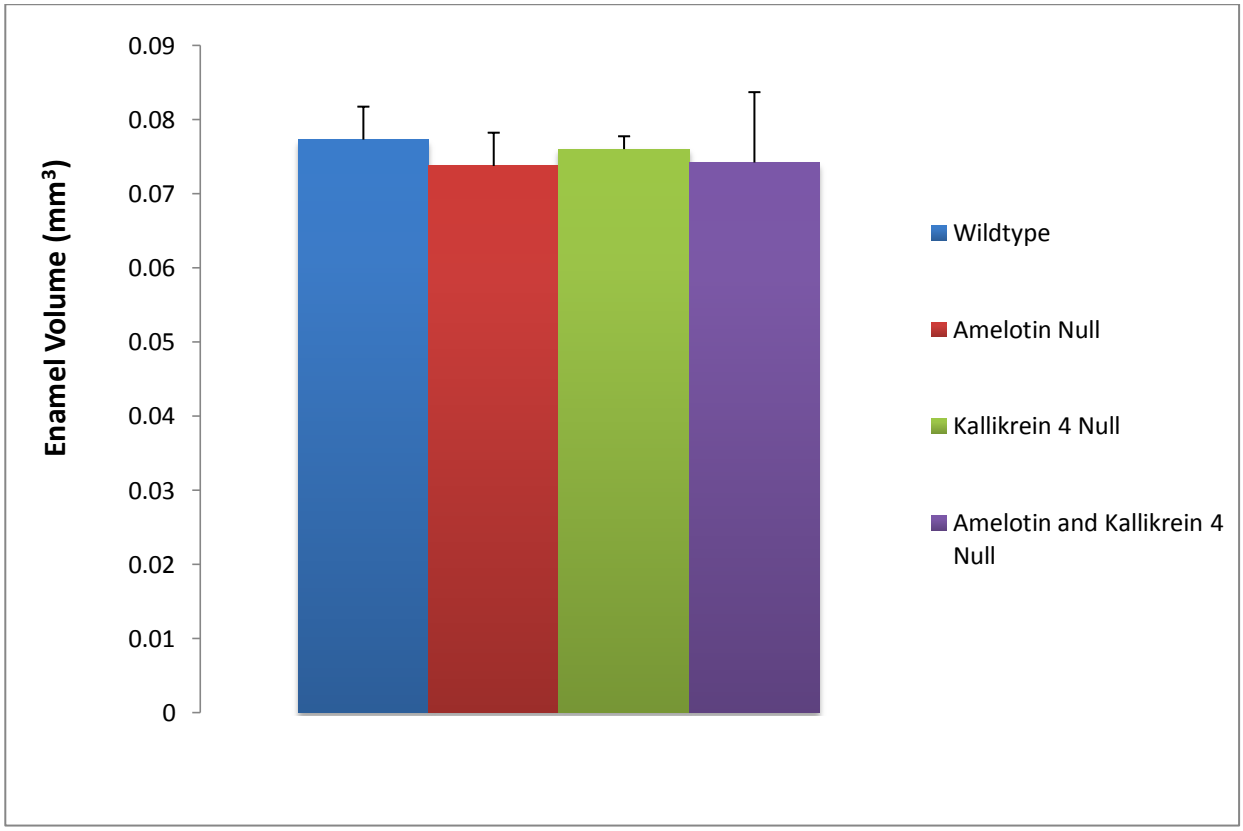

Fig. 4.5. Enamel volume. Enamel volume in the VOI was compared between groups. No significant differences were observed in enamel volume among the genotypes tested (*t*-test, $p>0.05$).

Using the LAC created with the phantoms, it was possible to obtain quantitative values for the enamel mineral density, which was found to be only slightly larger in the wild-type group compared to the *Amtn*-null group. While this difference was not significant, it showed a similar trend to what was found with hardness testing. In addition, the mineral density for the wild-type samples were similar to values found in previous studies (Schmitz et al., 2014) for the same region, with a value of 2.96 g/cm^3 compared to 2.97 g/cm^3 respectively. However, the *Amtn*-null group was similar to the wild-type group with 2.88 g/cm^3 (*t*-test, $p>0.05$).

The enamel mineral density was analyzed both with a 0 pixel peel and a 1 pixel peel, allowing for compensation of partial volume effects. This partial volume effect tends to occur on the periphery of tissues, meaning that these pixels often represent both enamel and air. As expected, the 1-pixel peel increases the density for all samples (Fig. 4.6, bottom). Additionally, a 50-micron "shell" of outer enamel was analyzed to see if there was an increased quantitative difference between groups in the outer 50-microns of the enamel layer (Fig. 4.7). This was found to reduce the overall difference between the wild-type samples and other groups, which can likely be explained by excluding the inner 50-microns of low density enamel adjacent to dentin in the *Klk4*-null and *Amtn*/*Klk4*-null groups.

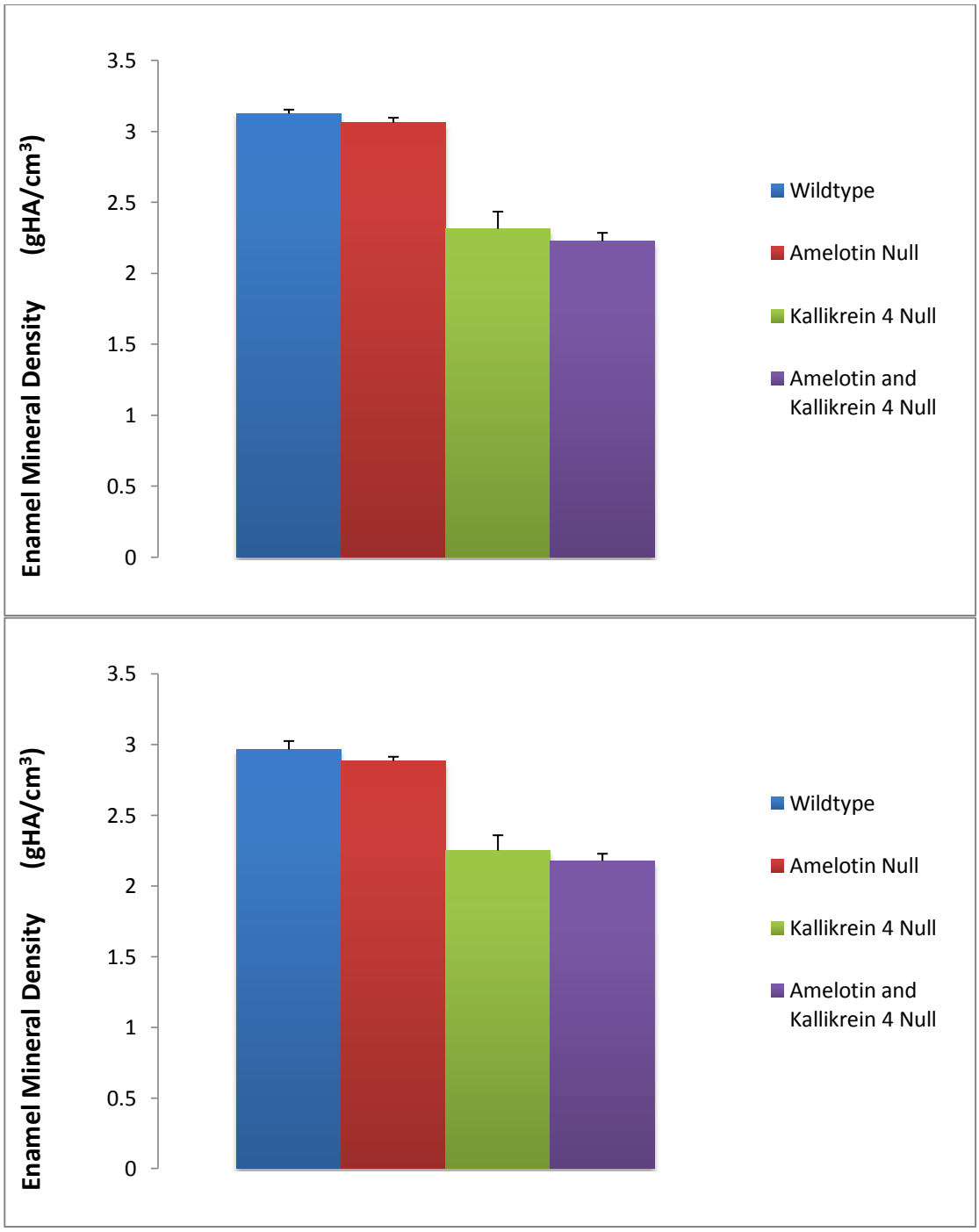

Fig. 4.6. Enamel mineral density using no pixel peel and one pixel peels. No pixel peel (top) and one pixel peel (bottom). The pixel peel was done to compensate for partial volume effects caused by air surrounding the sample that tend to occur at the periphery of tissues. Enamel mineral density was similar for wild-type and *Amtn*-null mice (*t*-test, $p>0.05$). Mineral density was also similar between *Klk4*-null and *Amtn*/*Klk4*-null mice (*t*-test, $p>0.05$), but lower than wild-type and *Amtn*-null (*t*-test, $p<0.05$).

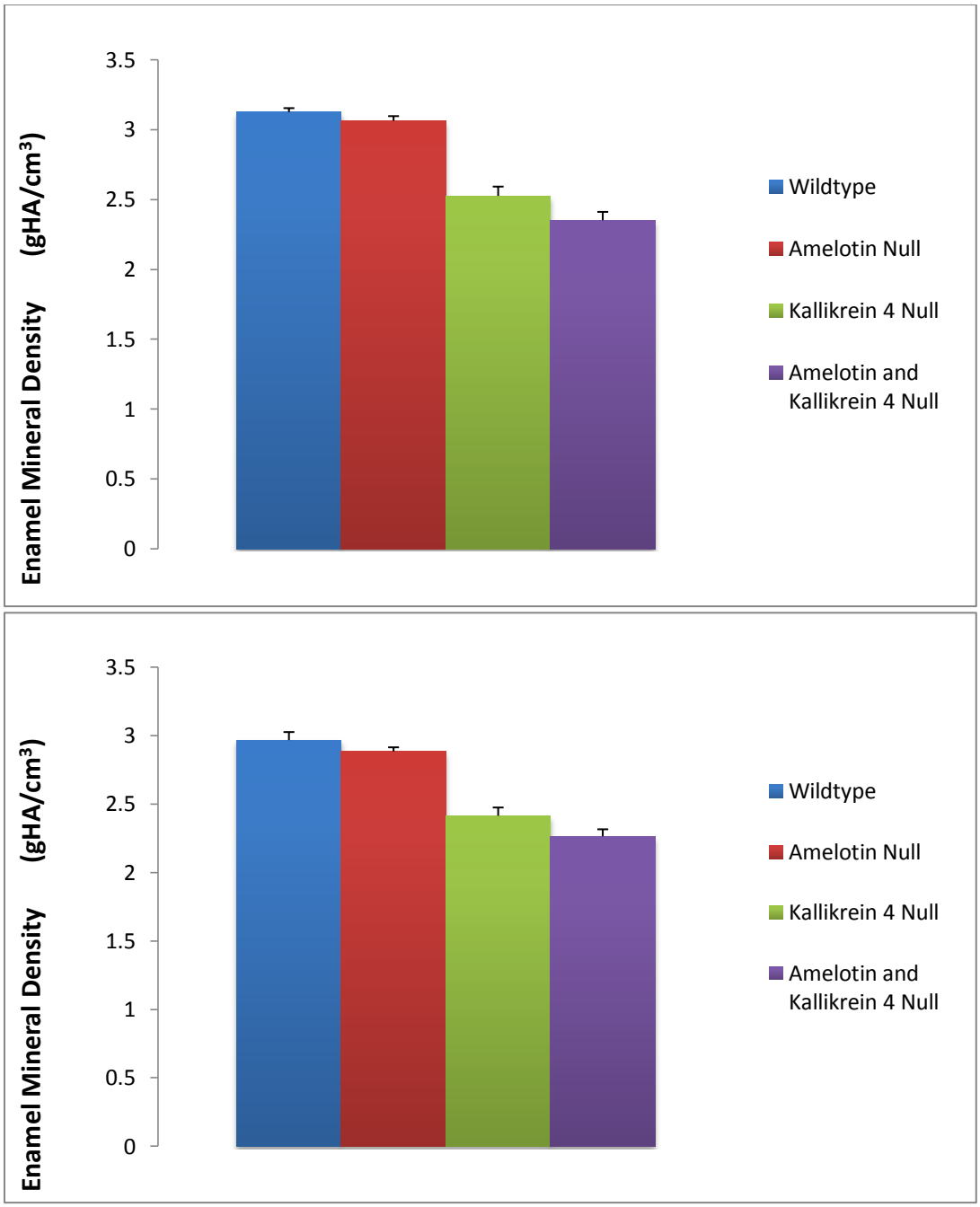

Fig. 4.7. Enamel mineral density using no pixel peel and one pixel peels of 50-micron shell. No pixel peel (top) and one pixel peel (bottom). Only the outer 50-microns of enamel were analyzed, to see if there was a mineralization difference between groups in that region. This analysis decreased the differences found if the entire enamel layer were analyzed.

We also used the maximum intensity projection (MIP) function to compare the enamel density along the length of the incisors in the hemimandibles between different

genotypes (Figs. 4.8 and 4.9). This function allows the visualization of high density structures surrounded by lower density media. In each column of voxels orthogonal to the selected plane, the highest density value found was assigned to that position in the generated image. The resulting image was a two-dimensional image of a three-dimensional structure. The MIP of the wild-type mice showed higher density enamel visible just distal to the first molar, coincident with the early maturation stage. In the *Amtn*-null mice, higher density enamel does not become visible until just mesial to the distal root of the first molar (Fig. 4.8).

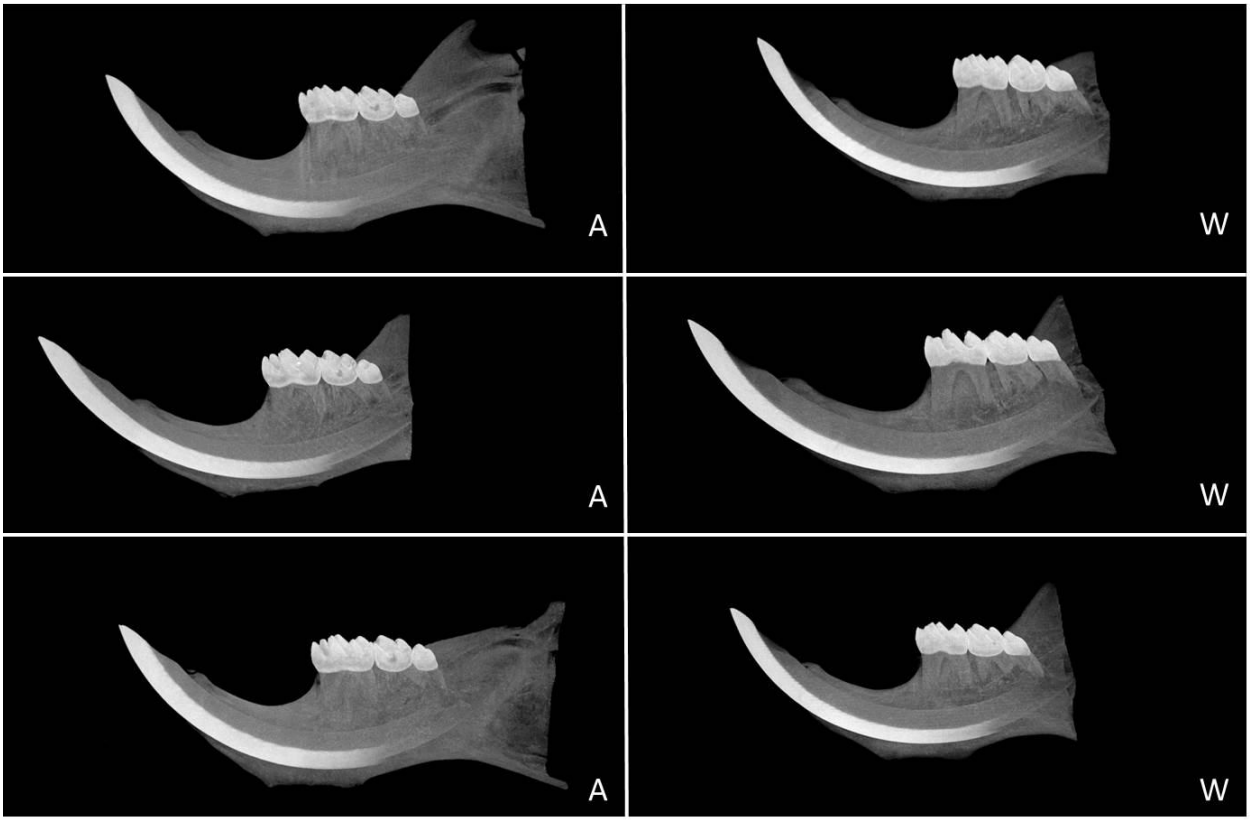

Fig. 4.8. Maximum intensity projections for *Amtn*-null and wild-type hemimandibles. The left column shows the three *Amtn*-null mice, and the right column shows the three wild-type mice that were visualized. In the wild-type mice, higher density enamel can be observed just distal to the first molar, where the early maturation stage begins. In the *Amtn*-null mice, higher density enamel does not begin until just mesial to the distal root of the first molar.

To better quantify this, a 40x50 pixel box was placed half-way between the distal root of the first molar and the mesial root of the second molar, an area that correlates with the early maturation stage (Fig. 4.9). The average gray value of this box was obtained using ImageJ, averaged for each group, and statistically analyzed using a Student's *t*-test (Fig. 4.10). The average gray value correlates directly with the enamel mineral density. When this value is compared with that of the wild-type, there is significantly lower gray scale value observed in the *Amtn*-null mouse (*t*-test, $p<0.02$).

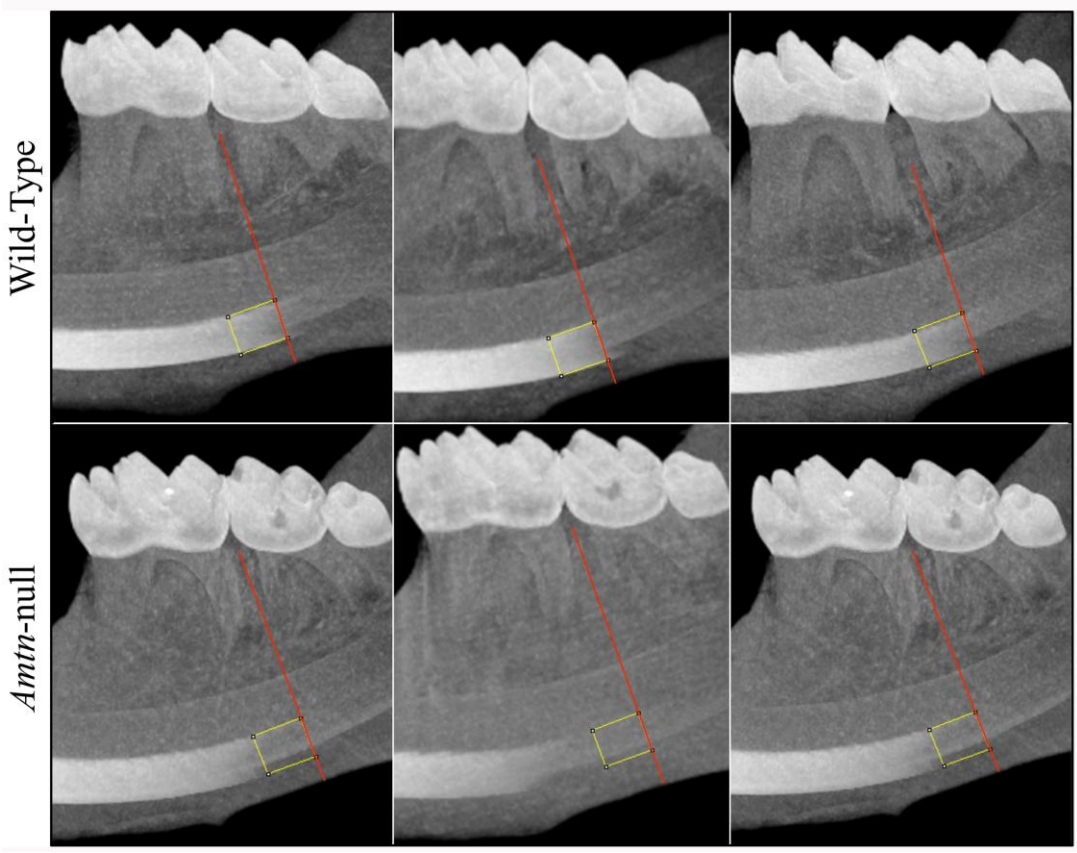

Fig. 4.9. Delay of maturation in *Amtn*$^{-/-}$ mice relative to the wild-type. These are zoomed-in images of maximum intensity projections for wild-type (top) and *Amtn*-null (bottom) hemimandibles. A 40x50 pixel box (2000 pixels squared) was placed over the enamel, half-way between the mesial root of the second molar and the distal root of the first molar. Average gray value in the yellow box in between the first and second molar was measured using ImageJ (red line indicates the location between the molars). This area correlates with the early maturation stage. Overall, a higher gray-scale value, which correlates with higher enamel density, was observed in the wild-type when compared to the *Amtn*-null mice.

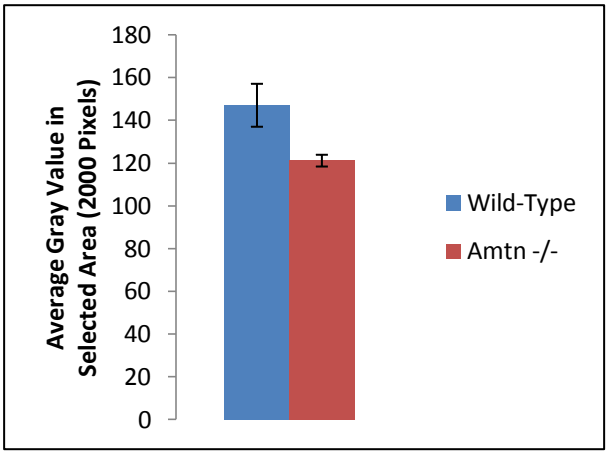

Fig. 4.10. Average gray-scale value in early maturation in wild-type and *Amtn*-null mice. When the gray-scale was measured in a 40x50 box (2000 pixels squared) placed halfway between the distal root of the first molar and the mesial root of the second molar (Fig. 4.9), the enamel mineral density was significantly less for the *Amtn*-null mouse than the wild-type mouse (*t*-test, $p<0.02$). This location is coincident with the onset of early maturation.

In *Klk4*-null mice, there is greater variation in the location where higher density enamel becomes visible, while in the *Amtn*/*Klk4*-null mice, higher density enamel consistently becomes visible mesial to the mesial root of the first molar (Fig. 4.11).

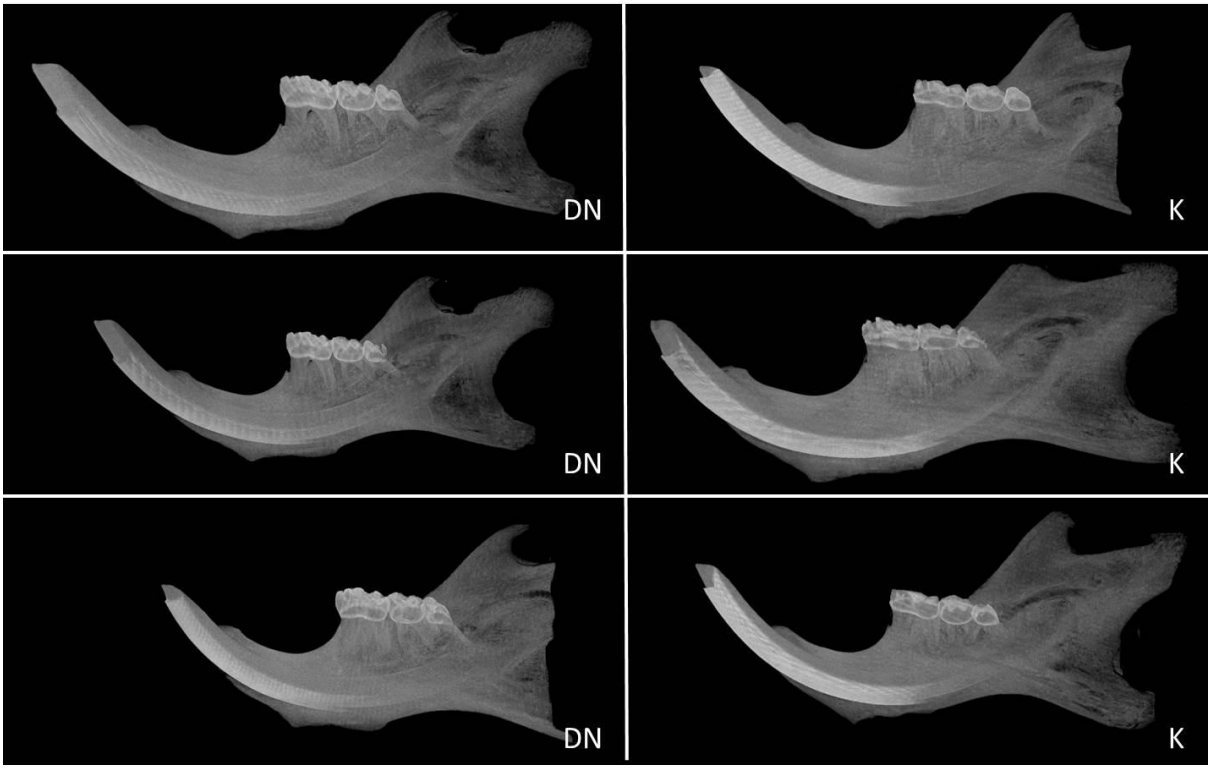

Fig. 4.11. Maximum intensity projections for *Amtn*/*Klk4*-null and Klk4-null hemimandibles. The left column shows the three *Amtn*/*Klk4*-null mice, and the right column shows the three *Klk4*-null mice that were visualized. In the *Klk4*-null mice, there is greater variation in the location at which higher density enamel starts to become visible. However, in the *Amtn*/*Klk4*-null mice, higher density enamel consistently becomes visible mesial to the mesial root of the first molar.

DISCUSSION

The accepted standard in quantifying enamel mineral content has been ashing microdissected strips of enamel from rodent incisors (Smith and Nanci, 1989; Weidmann et al., 1967). However, due to the large amount of time required, its technique sensitivity and required hand-skills, and the inherent destruction to the sample, a recent study (Schmitz et al., 2014) was able to use a high mineral density phantom to quantify enamel mineral content using micro-CT and correlate values found through tomography to those found using the ashing technique. The experiment described in this chapter sought to use a similar technique to compare the enamel layer of wild-type, *Amtn*-null, *Klk4*-null, and *Amtn*/*Klk4*-null animals in late maturation.

Enamel volume was found to be similar in all four genotypes (Fig 4.5): 0.077mm^3 in wild-type, 0.074mm^3 in *Amtn*-null, 0.076mm^3 in *Klk4*-null, 0.074mm^3 in *Amtn*/*Klk4*-null mice (*t*-test, $p>0.05$). Enamel thickness was found to be similar in all groups (Chapter 3), so it would be expected that a comparable VOI would yield similar enamel volumes as well. This also indicates that a comparable amount of enamel was analyzed in all samples for the chosen VOIs.

Enamel mineral density values of 2.96g/cm^3 for wild-type incisors were similar to those found in a recent study (Schmitz et al., 2014) that also used a high-density phantom of 2.927 g/cm^3, and was slightly higher than another study that extrapolated beyond their highest density phantom of 1.2 g/cm^3 (Bronckers et al., 2013), suggesting

that these values are within the reported range of enamel densities. *Amtn*-null values of 2.88 g/cm^3 were similar to wild-type values (*t*-test, p>0.05), so micro-CT was not sensitive enough to resolve the difference between these two groups or the sample size was not large enough to discern a small difference. However, this is consistent with the BEI findings described in Chapter 3 where wild-type and *Amtn*-null animals were essentially indistinguishable from each other. Similarly, the assay was not sensitive enough to differentiate *Klk4*-null (2.25 g/cm^3) from *Amtn*/*Klk4*-null (2.18 g/cm^3) (*t*-test, p>0.05). When the outer 50 microns of enamel were analyzed, there was less of a difference between groups: wild-type (2.96 g/cm^3), *Amtn*-null (2.88 g/cm^3), *Klk4*-null (2.41 g/cm^3), and *Amtn*/*Klk4*-null (2.26 g/cm^3). This was likely the result of removing the less-dense, inner enamel from the *Klk4*-null and *Amtn*/*Klk4*-null, making the density values appear closer to wild-type and *Amtn*-null mice.

The resolution available with micro-CT is much lower than what can be obtained with BEI. Given the findings presented in Chapter 4, if AMTN is only affecting enamel mineral hardness of the outer 15 microns of the enamel layer, it is not surprising that micro-CT was unable to reveal a difference between groups at the resolutions at which the samples were scanned. In this study, a 5 micron voxel size was used, but the SkyScan machine is capable of scanning at a 1 micron voxel size if a much longer scanning time were used per sample. If AMTN is indeed responsible for the

mineralization of the outer enamel, this difference in the enamel is unlikely to be shown through micro-CT scanning at 5 μm resolution.

Finally, we used the maximum intensity projection (MIP) function to compare the enamel density along the length of the incisors in the hemimandibles between different genotypes (Fig. 4.8 and 4.11). This allows for the two-dimensional visualization of the highest density voxel in the chosen plane of the three-dimensional scan. The MIP of the wild-type mice shows higher density enamel visible just distal to the first molar, coincident with the location of the early maturation stage (Fig. 2.1). In the *Amtn*-null mice, higher density enamel does not become visible until just mesial to the distal root of the first molar (Fig. 4.8), where the mid-maturation stage is typically found. In addition, when gray scale values in this region are compared (Fig. 4.9 and 4.10), which correlate directly with enamel mineral density, the *Amtn*-null mouse shows a significantly lower gray value when compared to the wild-type (*t*-test, $p<0.02$). A possible explanation for this could be that the lack of AMTN delays the beginning of the maturation stage. In the *Klk4*-null mice, there is greater variation in the location at which higher density enamel starts to become visible. However, in the *Amtn*/*Klk4*-null mice, higher density enamel consistently becomes visible mesial to the mesial root of the first molar (Fig. 4.9). Again, this might potentially be explained if the absence of AMTN did result in a delay of enamel maturation. A future study could resolve this question by selecting VOIs that include the transition between secretion and

maturation, coincident with the mesial root of the second molar (Fig. 2.1) and continue through the alveolar crest just prior to eruption. By quantitatively, measuring the changes in density along the length of the incisor, and comparing between genotypes, it might be possible to localize the point at which enamel mineral density spikes. This would allow for a comparative determination of how long it takes for enamel maturation to begin when AMTN and/or KLK4 are missing.

In summary, the μCT analyses determined that enamel volume is the same in all of the genotypes tested, which provides additional evidence that AMTN and KLK4 do not function during the secretory stage of amelogenesis. The μCT analyses confirm the findings of BEI that enamel formed in *Amtn*-null mice is not significantly different in its degree of mineralization immediately prior to eruption. Importantly, the μCT analyses discerned that enamel maturation is delayed in the *Amtn*-null mice.

REFERENCES

Bronckers, A.L., Gueneli, N., Lullmann-Rauch, R., Schneppenheim, J., Moraru, A.P., Himmerkus, N., Bervoets, T.J., Fluhrer, R., Everts, V., Saftig, P., *et al.* (2013). The intramembrane protease SPPL2A is critical for tooth enamel formation. J Bone Miner Res *28*, 1622-1630.

Burghardt, A.J., Kazakia, G.J., Laib, A., and Majumdar, S. (2008). Quantitative assessment of bone tissue mineralization with polychromatic micro-computed tomography. Calcif Tissue Int *83*, 129-138.

Cheng, J.C., Qin, L., Cheung, C.S., Sher, A.H., Lee, K.M., Ng, S.W., and Guo, X. (2000). Generalized low areal and volumetric bone mineral density in adolescent idiopathic scoliosis. J Bone Miner Res *15*, 1587-1595.

Chueh, H.S., Tsai, W.K., Fu, H.M., and Chen, J.C. (2006). Evaluation of the quantitative capability of a home-made cone-beam micro computed tomography system. Comput Med Imaging Graph *30*, 349-355.

Elliott, J.C., Wong, F.S., Anderson, P., Davis, G.R., and Dowker, S.E. (1998). Determination of mineral concentration in dental enamel from X-ray attenuation measurements. Connect Tissue Res *38*, 61-72; discussion 73-69.

Fajardo, R.J., Cory, E., Patel, N.D., Nazarian, A., Laib, A., Manoharan, R.K., Schmitz, J.E., DeSilva, J.M., MacLatchy, L.M., Snyder, B.D., *et al.* (2009). Specimen size and porosity can introduce error into microCT-based tissue mineral density measurements. Bone *44*, 176-184.

Fajardo, R.J., Ryan, T.M., and Kappelman, J. (2002). Assessing the accuracy of high-resolution X-ray computed tomography of primate trabecular bone by comparisons with histological sections. Am J Phys Anthropol *118*, 1-10.

Huang, T.T., Jones, A.S., He, L.H., Darendeliler, M.A., and Swain, M.V. (2007). Characterisation of enamel white spot lesions using X-ray micro-tomography. J Dent *35*, 737-743.

Inness, E.K., Moutrie, V., and Charles, P.H. (2014). The dependence of computed tomography number to relative electron density conversion on phantom geometry and its impact on planned dose. Australas Phys Eng Sci Med.

Kujoory, M.A., Hillman, B.J., and Barrett, H.H. (1980). High-resolution computed tomography of the normal rat nephrogram. Invest Radiol *15*, 148-154.

Layton, M.W., Goldstein, S.A., Goulet, R.W., Feldkamp, L.A., Kubinski, D.J., and Bole, G.G. (1988). Examination of subchondral bone architecture in experimental osteoarthritis by microscopic computed axial tomography. Arthritis Rheum *31*, 1400-1405.

Nazarian, A., Snyder, B.D., Zurakowski, D., and Muller, R. (2008). Quantitative micro-computed tomography: a non-invasive method to assess equivalent bone mineral density. Bone *43*, 302-311.

Nuzzo, S., Peyrin, F., Cloetens, P., Baruchel, J., and Boivin, G. (2002). Quantification of the degree of mineralization of bone in three dimensions using synchrotron radiation microtomography. Med Phys *29*, 2672-2681.

Odgaard, A., Andersen, K., Melsen, F., and Gundersen, H.J. (1990). A direct method for fast three-dimensional serial reconstruction. J Microsc *159*, 335-342.

Peyrin, F., Houssard, J.P., Maurincomme, E., Peix, G., Goutte, R., Laval-Jeantet, A.M., and Amiel, M. (1993). 3D display of high resolution vertebral structure images. Comput Med Imaging Graph *17*, 251-256.

Ritman, E.L. (2004). Micro-computed tomography-current status and developments. Annu Rev Biomed Eng *6*, 185-208.

Robinson, C., Lowe, N.R., and Weatherell, J.A. (1977). Changes in amino-acid composition of developing rat incisor enamel. Calcif Tissue Res *23*, 19-31.

Rodet, T., Noo, F., and Defrise, M. (2004). The cone-beam algorithm of Feldkamp, Davis, and Kress preserves oblique line integrals. Med Phys *31*, 1972-1975.

Sanada, S., Kawahara, K., Yamamoto, T., and Takashima, T. (1999). New tissue substitutes representing cortical bone and adipose tissue in quantitative radiology. Phys Med Biol *44*, N107-112.

Sato, T., Ikeda, O., Yamakoshi, Y., and Tsubouchi, M. (1981). X-ray tomography for microstructural objects. Appl Opt *20*, 3880-3883.

Schmitz, J.E., Teepe, J.D., Hu, Y., Smith, C.E., Fajardo, R.J., and Chun, Y.H. (2014). Estimating mineral changes in enamel formation by ashing/BSE and microCT. J Dent Res *93*, 256-262.

Schweizer, S., Hattendorf, B., Schneider, P., Aeschlimann, B., Gauckler, L., Muller, R., and Gunther, D. (2007). Preparation and characterization of calibration standards for bone density determination by micro-computed tomography. Analyst *132*, 1040-1045.

Smith, C.E., and Nanci, A. (1989). A method for sampling the stages of amelogenesis on mandibular rat incisors using the molars as a reference for dissection. Anat Rec *225*, 257-266.

Smith, C.E., Wazen, R., Hu, Y., Zalzal, S.F., Nanci, A., Simmer, J.P., and Hu, J.C. (2009). Consequences for enamel development and mineralization resulting from loss of function of ameloblastin or enamelin. Eur J Oral Sci *117*, 485-497.

Weidmann, S.M., Weatherell, J.A., and Hamm, S.M. (1967). Variations of enamel density in sections of human teeth. Arch Oral Biol *12*, 85-97.

Wise, L.D., Winkelmann, C.T., Dogdas, B., and Bagchi, A. (2013). Micro-computed tomography imaging and analysis in developmental biology and toxicology. Birth Defects Res C Embryo Today *99*, 71-82.

Zou, W., Hunter, N., and Swain, M.V. (2011). Application of polychromatic microCT for mineral density determination. J Dent Res *90*, 18-30.

CHAPTER 5

MICROHARDNESS TESTING OF MANDIBULAR INCISOR ENAMEL

ABSTRACT

Knoop microindentation was performed on the incisors of six mice for each genotype (Wild-type, *Amtn*-null, *Klk4*-null, *Amtn*/*Klk4*-heterozygote, and *Amtn*/*Klk4*-null) for a total of thirty animals. A single indentation was placed in the outer, middle, and inner enamel as well as the dentin and this was repeated three times per animal for a total of twelve points per incisor. A load of 25 g was used with a 10 s dwell time. Corresponding points were averaged and analyzed by pair-wise *t*-tests. The outer enamel was significantly softer in the amelotin-null compared to the wild-type. The outer enamel was also significantly softer in the *Amtn*/*Klk4* double null compared to the *Klk4* single null. The *Amtn*/*Klk4*-heterozygote showed similar values to the wild-type at all points. Dentin values for all five groups of animals were the same. We conclude that AMTN is important for achieving the final hardness of the outer 15 μm of enamel that it likely serves this function independently of KLK4.

INTRODUCTION

Microhardness testing is commonly used to quantitatively measure enamel hardness and can serve as an indirect measure of mineral loss or gain (Attin, 2006; Collys et al., 1992; Hara et al., 2009; Shin et al., 2014). There are two commonly used tests in the enamel field, namely Knoop and Vicker's. In a Vicker's microhardness test, the indenter is shaped like a diamond in the form of a square-based pyramid. The Vicker's indenter shape was designed so that the resulting indentation could produce geometrically similar impressions, irrespective of the size of the indentation (Smith, 1922). Additionally, the mathematical calculations are simplified since they are independent of the size of the indenter, and the same indenter can be used across different materials irrespective of hardness (Smith, 1922). To obtain a hardness value, both axes of the indent are measured and the applied load over the resulting surface area of the indent is calculated (Arends and ten Bosch, 1992). The length of the axes of the indent correlates inversely with the hardness of the material: the larger the hardness value of the material, the smaller the resulting indentation and vice versa. With a Knoop microhardness test, experiments are performed with a diamond indenter shaped like a rhombic pyramid, and leave an elongated diamond-shaped indent in the sample being measured (Purdell-Lewis et al., 1976). The longest axis is measured and like Vicker's, correlates inversely with the hardness of the material.

In the field of enamel development, microhardness values are usually measured for the incisor enamel (Attin, 2006; Tye et al., 2009). Two recent studies performed nanoindentation on molars, but there is not much additional data for molar enamel hardness in the mouse model (Cheng et al., 2011; Pugach et al., 2013). The advantage to using incisors is partly the ease of choosing a highly reproducible location using surrounding anatomy, and the ability to test enamel at different points in development along the same incisor (see Chapter 2, Fig. 2.1 for a detailed image describing the location of the different stages of amelogenesis along the length of the incisor). In addition, it is possible with incisors to choose very mature enamel that has not yet erupted into function, so that confounding factors such as damage or wear from mastication can be taken out of the analysis. If molars are used, particularly in genotypes that show severe enamel defects, it is best to use post-natal day 15 when the molars are just erupting to allow for analysis of enamel that has not yet been in function (Wise et al., 2002).

It is important to understand that the hardness value is not a physical property of the material, but rather a characteristic. It is a measure of the resistance to indentation based on a set of defined parameters (Arends and ten Bosch, 1992). Microhardness testing also does not measure mineral content directly (Clasen and Ogaard, 1999). For experiments measuring the microhardness of mineralized tissues, points are typically taken in enamel. However, when dentin points are used, they must be read

immediately because after a period of time, points will tend to relax due to its higher organic content so an accurate length measurement cannot be obtained (Clasen and Ogaard, 1999; Herkstroter et al., 1989). Depending on the machine being used, the amount of force can range from 10g-1000g and is held for a defined dwell time, usually ranging from 5-15 seconds. The length (in micrometers) of the longest diagonal of the resulting Knoop indentation is measured by imaging under a microscope. A polished, even surface that is placed perpendicular to the indenter is required to yield a symmetric, readable indent to obtain accurate and reproducible results.

MATERIALS AND METHODS

Incisors were prepared as described in the materials and methods section of chapter 3 for backscatter electron microscopy (BEI). After imaging, samples were polished with 1-micron MicroDi Permanent Diamond Suspension (South Bay Technology Inc., San Clemente, CA) to remove the carbon coating used for BEI and air dried. Six animals of each genotype (Wild-type, *Amtn*-null, *Klk4*-null, *Amtn*/*Klk4*-heterozygote, and *Amtn*/*Klk4*-null) were tested on a microhardness tester (LM247AT, s/n XM0326, Leco Corp.). Microhardness testing was performed with a load of 25 grams for 10 seconds with a Knoop tip to obtain a Knoop Hardness Number (KHN). Measurements were made at 500X magnification to increase precision. Indentations were placed in the outer,

middle, and inner enamel as well as the dentin as a control reading for a total of four indentations per row. This series was performed three times in each animal, for a total of twelve points per animal. Outer enamel is defined as 15 microns from the outer surface of the enamel layer. Inner enamel is defined as within 15-20 microns from DEJ on the enamel side. Middle enamel was defined as halfway between the outer and inner enamel indentation, with a range of 50-60 microns from the outer enamel surface. The dentin indentation was placed 20 microns away from the DEJ on the dentin side. Points that landed in cracks or damaged portion of the enamel or dentin were not read. Statistical significance was determined by pairwise *t*-tests using SPSS analysis software.

RESULTS

Microhardness testing was performed to quantitatively discern any differences in enamel hardness between genotypes. Incisors were prepared as described for BEI analysis. Indentations were placed in the outer, middle, and inner enamel as well as in the dentin as a control point (Fig. 5.1). These points were averaged to obtain an average value for each location per animal. All animals in each group were then averaged together to obtain a single average per genotype per location and these values are summarized in Fig. 5.2. Indentations were placed away from cracks that developed during processing of the mandibles. Any points that were uneven or asymmetric were not read and a new point was placed.

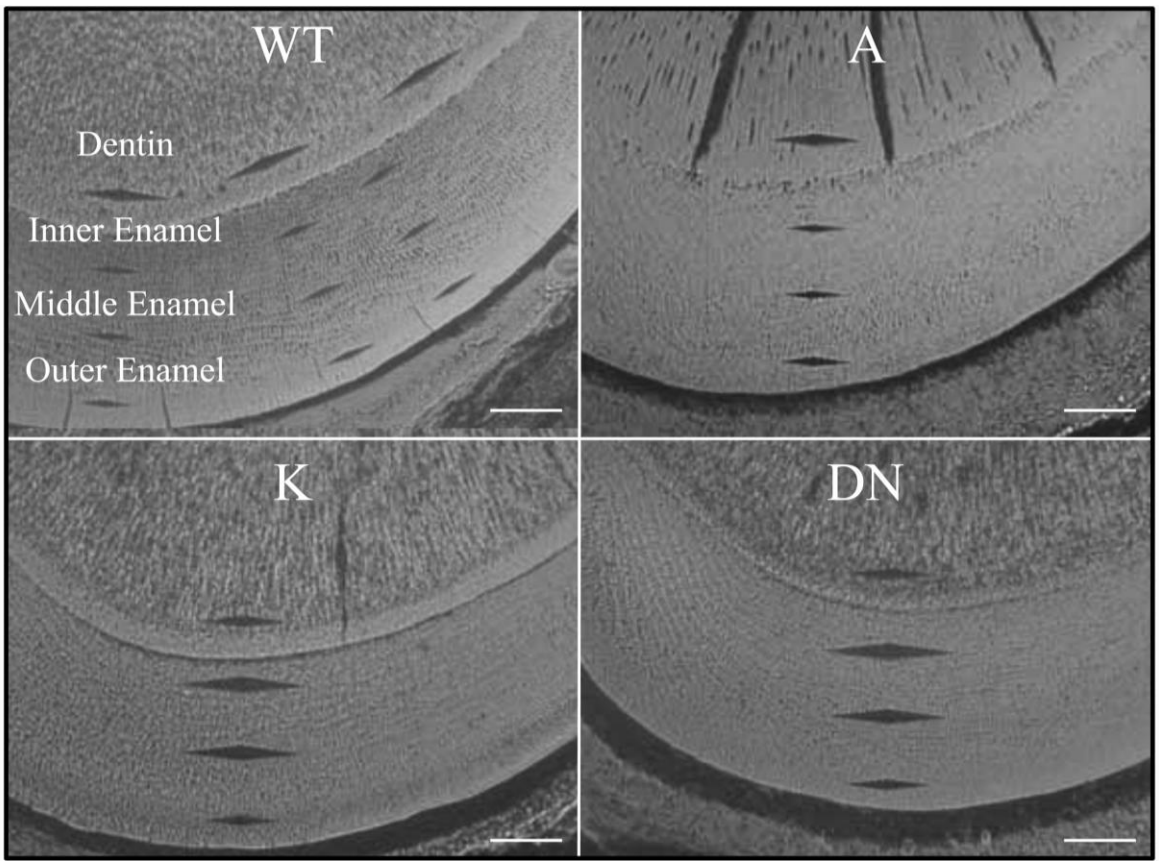

Fig. 5.1. Location of hardness testing indentations. (Magnification 200X) Indentations were made perpendicular to the sample surface and placed in the outer, middle, and inner enamel, as well as in dentin. This series of indentations was made 3 times per incisor as illustrated in the wild-type panel. The size of the indentations inversely correlates with the hardness of the material, so that the larger the indentation, the softer the material. ***Key:*** WT, wild-type; A, *Amtn*-null; K, *Klk4*-null; DN, *Amtn*/*Klk4*-null.Bar = 50 μm.

	WT	DH	A	KLK4	DN
Outer Enamel	327.1 ±19.8	320.9 ±27.8	249.8 ±45.6	201.0 ±26.6	141.4 ±26.8
Middle Enamel	315.8 ±14.9	312.5 ± 12.0	293.3 ±20.9	80.8 ±15.4	75.0 ±9.0
Inner Enamel	270.9 ±13.3	277.7 ±16.6	272.6 ±17.8	62.1 ±17.8	75.3 ±11.1
Dentin	104.5 ±2.8	114.9 ±6.6	106.8 ± 4.0	107.8 ±5.0	113.7 ±6.5

Fig. 5.2. Knoop hardness values. Outer enamel is the 15 μm from the outer surface of the enamel layer. Inner enamel is 15-20 μm from DEJ. Middle enamel is halfway between the outer and inner enamel indentation, with a range of 50-60 μm from the outer enamel surface. The dentin indentation was placed 20 μm away from the DEJ. N=6 animals per genotype. All values are expressed as mean Knoop hardness values ± standard deviation. ***Key:*** WT, wild-type; A, *Amtn*-null; K, *Klk4*-null; DN, *Amtn*/*Klk4*-null.

In the outer enamel, the *Amtn*-null group had a Knoop hardness value of 249.8 ± 45.6, which was significantly smaller compared to the wild-type group value of 327.1 ±

19.8 (*t*-test, p<0.001). Similarly, at that same location the *Amtn*/*Klk4*-null group had a significantly smaller value of 141.4 ± 26.8 than the *Klk4*-null group value of 201.0 ±26.6 (*t*-test, p<0.001) (Figs. 5.3 and 5.4). There was no significant difference at any location between the wild-type group and the *Amtn*/*Klk4*-heterozygote group, likely because defects in *Amtn* are recessive (Fig. 5.5). There was no significant difference at any other location between groups (*t*-test, p>0.05). In addition, all hardness values decreased from the outer enamel to the inner enamel with the exception of the *Amtn*-null group, where the middle enamel had a larger hardness than the outer enamel, further indicating that only the outer enamel hardness was affected by the absence of a functional protein. Therefore, the protein amelotin is important for the outer 15 microns of the enamel layer to reach its final hardness during the maturation stage.

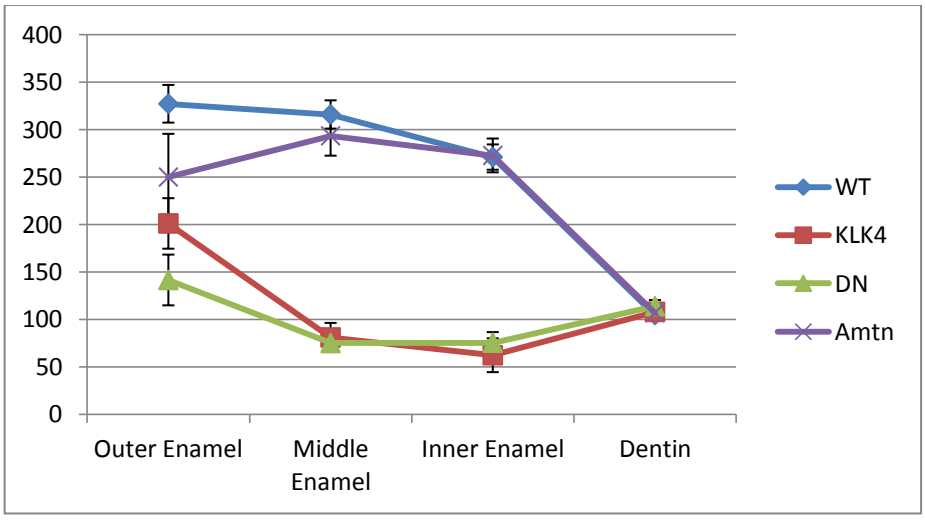

Fig. 5.3. Knoop hardness values in the outer, middle, and inner enamel, and dentin. Only in the outer enamel is there a significant difference in hardness between the wild-type and *Amtn*-null, and also between the *Klk4*-null and *Amtn*/*Klk4*-null. Dentin values are similar for all animals measured. Hardness values decrease from the outer enamel into the DEJ, with the exception of *Amtn*-null animals, where there is an increase in hardness from the outer to middle enamel.

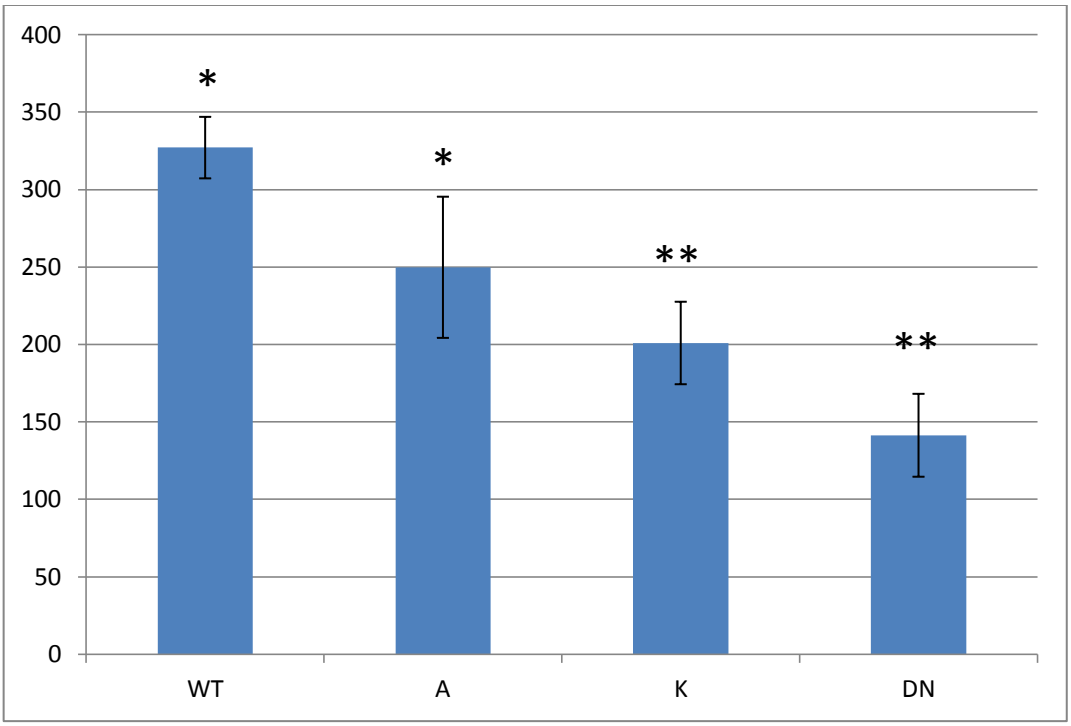

Fig. 5.4. Knoop hardness values in the outer enamel. The *Amtn*-null group showed a significant decrease in outer enamel hardness (*t*-test, $p<0.001$) compared to the wild-type. Similarly, the *Amtn*/*Klk4*-null group showed a significant decrease in outer enamel hardness (*t*-test, $p<0.001$) compared to the *Klk4*-nulls. ***Key:*** WT, wild-type; A, *Amtn*-null; K, *Klk4*-null; DN, *Amtn*/*Klk4*-null.

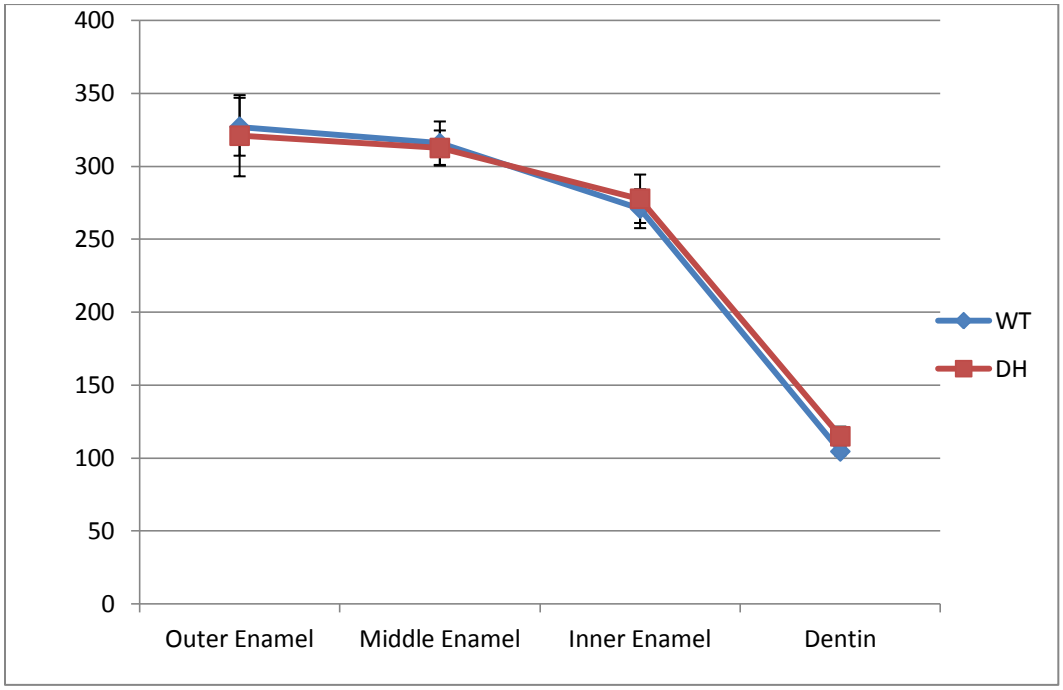

Fig. 5.5. Wild-type and *Amtn*/*Klk4*-heterozygote Knoop hardness values. There is no significant difference at any location between these genotypes (*t*-test, $p>0.05$).

DISCUSSION

The purpose of the maturation stage of amelogenesis is to remove the protein matrix that was necessary for correct deposition of the enamel layer and replace it with mineral to allow it to reach its final hardness before eruption into the oral cavity (Lacruz et al., 2013). When this process proceeds aberrantly, the resulting enamel is soft, cheese-like, and sheers off soon after the tooth erupts.

The proteins KLK4 and AMTN are both expressed during the maturation stage of amelogenesis. KLK4, a secreted serine protease, participates in bulk cleaving of enamel matrix proteins (both amelogenins and non-amelogenins) into smaller polypeptides, which presumably facilitates their reuptake into ameloblasts (Simmer et al., 2009). AMTN, on the other hand, is primarily associated with the basal lamina throughout the maturation stage and at the surface of the junctional epithelium after eruption of the tooth (Moffatt et al., 2006; Nishio et al., 2013).

Many studies have shown that when KLK4 is absent, the resulting enamel is hypomatured and easily shears off during function. However, the role of AMTN in the maturation stage and whether it participates in protein removal (like KLK4) or in other processes is still unclear. To indirectly study this relationship, Knoop microhardness was chosen as a quantitative measure of enamel hardness, which correlates with the amount of retained protein matrix in the enamel layer. In this study, experiments show that lack of AMTN affects the enamel quality in the outer 15 microns of enamel

resulting in a significantly softer mineral compared to when the protein is present. When comparing the *Amtn*-null to the wild-type animal and the *Amtn*/*Klk4*-null to the *Klk4*-null alone, the outer 15 microns of enamel were significantly softer (t-test, $p<0.001$). This suggests that not only is AMTN necessary for achieving the final hardness of the outer enamel, but this important function seems to be entirely independent of KLK4.

In summary, microhardness testing revealed that the outer enamel layer in *Amtn*-null mice is less hard than that of the wild-type, supporting the conclusion that AMTN is required to achieve the final hardness of the outer enamel. Microhardness testing also revealed that the outer enamel of *Amtn*/*Klk4* double null mice is less hard than that of the *Klk4* single null. This suggests that AMTN contributes to the hardening of the outer enamel even in the absence of KLK4, supporting the conclusion that AMTN and KLK4 act independent of each other during enamel maturation.

REFERENCES

Arends, J., and ten Bosch, J.J. (1992). Demineralization and remineralization evaluation techniques. J Dent Res *71 Spec No*, 924-928.

Attin, T. (2006). Methods for assessment of dental erosion. Monogr Oral Sci *20*, 152-172.

Cheng, Z.J., Wang, Q., Wang, X.M., Cui, F.Z., Ge, J., Chen, D., and Tian, L.L. (2011). Enamel distribution, structure and mechanical alterations in col1-caPPR mice molar. Arch Oral Biol *56*, 1020-1026.

Clasen, A.B., and Ogaard, B. (1999). Experimental intra-oral caries models in fluoride research. Acta Odontol Scand *57*, 334-341.

Collys, K., Slop, D., Cleymaet, R., Coomans, D., and Michotte, Y. (1992). Load dependency and reliability of microhardness measurements on acid-etched enamel surfaces. Dent Mater *8*, 332-335.

Hara, A.T., Kelly, S.A., Gonzalez-Cabezas, C., Eckert, G.J., Barlow, A.P., Mason, S.C., and Zero, D.T. (2009). Influence of fluoride availability of dentifrices on eroded enamel remineralization in situ. Caries Res *43*, 57-63.

Herkstroter, F.M., Witjes, M., Ruben, J., and Arends, J. (1989). Time dependency of microhardness indentations in human and bovine dentine compared with human enamel. Caries Res *23*, 342-344.

Lacruz, R.S., Smith, C.E., Kurtz, I., Hubbard, M.J., and Paine, M.L. (2013). New paradigms on the transport functions of maturation-stage ameloblasts. J Dent Res *92*, 122-129.

Moffatt, P., Smith, C.E., St-Arnaud, R., Simmons, D., Wright, J.T., and Nanci, A. (2006). Cloning of rat amelotin and localization of the protein to the basal lamina of maturation stage ameloblasts and junctional epithelium. Biochem J *399*, 37-46.

Nishio, C., Wazen, R., Moffatt, P., and Nanci, A. (2013). Expression of odontogenic ameloblast-associated and amelotin proteins in the junctional epithelium. Periodontol 2000 *63*, 59-66.

Pugach, M.K., Suggs, C., Li, Y., Wright, J.T., Kulkarni, A.B., Bartlett, J.D., and Gibson, C.W. (2013). M180 amelogenin processed by MMP20 is sufficient for decussating murine enamel. J Dent Res *92*, 1118-1122.

Purdell-Lewis, D.J., Groeneveld, A., and Arends, J. (1976). Hardness tests on sound enamel and artificially demineralized white spot lesions. Caries Res *10*, 201-215.

Shin, M., Hu, Y., Tye, C.E., Guan, X., Deagle, C.C., Antone, J.V., Smith, C.E., Simmer, J.P., and Bartlett, J.D. (2014). Matrix Metalloproteinase-20 Over-Expression Is Detrimental to Enamel Development: A Mus musculus Model. PLoS One *9*, e86774.

Simmer, J.P., Hu, Y., Lertlam, R., Yamakoshi, Y., and Hu, J.C. (2009). Hypomaturation enamel defects in Klk4 knockout/LacZ knockin mice. J Biol Chem *284*, 19110-19121.

Smith, R.L., Sandland, G.E. (1922). An Accurate Method of Determining the Hardness of Metals, with Particular Reference to Those of a High Degree of Hardness. Proceedings of the Institution of Mechanical Engineers *I*, 623-641.

Tye, C.E., Pham, C.T., Simmer, J.P., and Bartlett, J.D. (2009). DPPI may activate KLK4 during enamel formation. J Dent Res *88*, 323-327.

Wise, G.E., Frazier-Bowers, S., and D'Souza, R.N. (2002). Cellular, molecular, and genetic determinants of tooth eruption. Crit Rev Oral Biol Med *13*, 323-334.

CHAPTER 6

TRANSMISSION ELECTRON MICROSCOPY

ABSTRACT

Enamel maturation is characterized by the removal of residual enamel protein and replacement of the space formerly occupied by enamel proteins with mineral, through the expansion in width and thickness of thin crystallites deposited during the secretory stage. During the maturation stage, KLK4 contributes to the removal of enamel proteins. How AMTN contributes is unknown. That AMTN does play a role in enamel maturation is supported by observations of chalky enamel that undergoes attrition, delayed onset of enamel maturation, and reduced hardness of the outer enamel layer in the *Amtn*-null incisors. We speculated that there is a difference in the amount of retained protein matrix in the outer enamel during the maturation stage of amelogenesis between the wild-type, *Amtn*-null, *Klk4*-null, *Amtn*/*Klk4*-null, and *Amtn*/*Klk4*-heterozygote mouse incisors. Since the bulk of the secreted enamel matrix is composed of amelogenin, a primary antibody against full-length recombinant protein (rM179) was used on ultrathin sections obtained from the mandibular incisor segments taken at the alveolar crest. The presence of gold-labeled secondary antibody was

quantified to represent the residual amelogenins in the outer enamel in a series of sequential, non-overlapping images. Gold particles were counted in selected areas of enamel and averaged for each genotype. Sections from *AmelX*-null mice were included in this analysis as a negative control to determine background levels of immunolabeling. We observed no difference in labeling in wild-type, *Amtn*-null, and *Amtn*/*Klk4*-heterozygous animals. Additionally, these three groups were similar in labeling density to *AmelX*-null mice. While *Klk4*-null and *Amtn*/*Klk4*-null animals showed more amelogenin labeling, these two groups were similar to each other. We conclude that while KLK4 is required for protein removal during the maturation stage, it is unlikely that AMTN functions in the outer enamel by assisting in the removal of protein.

INTRODUCTION

In chapter 5, it was shown that AMTN is involved in establishing the final hardness of the outer 15 micrometers of enamel since the lack of this protein results in a significantly softer outer enamel layer when measured by Knoop microhardness testing. However, in Chapter 3, when the enamel layer was visualized using BEI to determine differences in mineral density, there was no detectable change in the outer enamel layer when AMTN was absent. Therefore, this aspect of the study focuses on using transmission electron microscopy (TEM) and immunogold labeling to discern if

there is any excess retained protein matrix in the outer enamel layer that might account for the softer outer enamel when AMTN is missing.

Colloidal gold labeling techniques were first introduced in the early 1970's (Faulk and Taylor, 1971) where a primary antibody was directly conjugated to gold to identify salmonella antigens. Indirect labeling using protein A conjugated to gold was introduced a few years later to detect primary immunoglobulin (Roth et al., 1978). These techniques were then applied to thin sections for electron microscopy (Roth et al., 1980) and since then has become the primary method for ultra-structural studies of cellular antigens. Gold particles come in various sizes, but typically range from 1-40nm in size. These varying sizes allow for dual-labeling given that the gold particles can be measured under the microscope to distinguish between different antigens. This technique has been previously used successfully to study protein co-secretory pathways in enamel development (Zalzal et al., 2008), attesting to its power and flexibility.

The challenge with this technique in the mineralized tissue field is that samples are often decalcified for several days to weeks in 4.13% ethylenediaminetetraacetic acid (EDTA) to allow for microtome cutting of ultrathin sections. This extended process requires the tissues to be adequately fixed, without losing the necessary tissue antigenicity for immunolabeling. Several studies have gotten around this problem by using a low concentration of glutaraldehyde, typically around 1%, followed by post-fixation of the sample after decalcification with reduced osmium tetroxide. This fixation

requires an antigen retrieval step by incubating the tissue sections in 5% sodium metaperiodate for one hour (Dos Santos Neves et al., 2012; Nanci et al., 1993; Nanci et al., 1987).

After AMTN was identified as a maturation stage protein, it was localized to the basal lamina through immunogold labeling (Dos Santos Neves et al., 2012; Moffatt et al., 2006; Somogyi-Ganss et al., 2012). Current hypotheses about its function in the maturation stage include mediating the attachment of ameloblasts to the basement membrane (Nishio et al., 2013) and/or promoting the formation of the outer layer of prismless enamel (Lacruz et al., 2012; Somogyi-Ganss et al., 2012). More recently, it has been suggested that AMTN and ODAM, another maturation stage basal lamina protein, together maintain the boundary between the unmineralized and hypermineralizing domains of maturing enamel, serving as the interface for the transfer of degraded matrix proteins and calcium phosphate (Kawasaki, 2013).

Given that amelogenin accounts for most of the secretory stage protein matrix (Simmer and Hu, 2001; Zalzal et al., 2008), and that this matrix is removed and reabsorbed by ameloblasts during the maturation stage (Smith, 1998), we used an antibody against recombinant amelogenin protein to determine if there is a difference in the amount of retained protein matrix in wild-type, *Amtn*-null, *Amtn*/*Klk4*-heterozygote, and *Amtn*/*Klk4*-null animals.

MATERIALS AND METHODS

Antibodies

Mouse recombinant amelogenin antibody (M179, lacking the N-terminal methionine and the Ser^{16}-phosphate group found on the M180 isoform (Simmer et al., 1994) was used. Protein A conjugated to 15 nanometer diameter gold particle (Aurion, Wageningen, Netherlands) was used for secondary labeling.

Sample Preparation for Immunohistochemistry

Mice that were 7-weeks of age (wild-type, *Amtn*-null, *Klk4*-null, *Amtn*/*Klk4*-heterozygous, *Amtn*/*Klk4*-null, and *AmelX*-null) were anesthetized with isofluorane and sacrificed by intracardial perfusion through the left ventricle. Mice were perfused with Ringer's lactate (Abbott Laboratories; Montreal, QC, Canada) followed by a solution of 1% glutaraldehyde, 0.8M sodium cacodylate, and 0.05% calcium chloride, pH 7.4 for 20 min. Hemimandibles were dissected out, soft tissue was removed, and they were incubated in the same fixative at 4 °C for 1 additional hour, washed briefly in 1X-PBS, and then transferred to 4.13% EDTA for decalcification for 30 days (solution was changed every 2-3 days) similar to previous studies (Nanci et al., 1992; Orsini et al., 2001). Hemimandibles were removed from decalcification solution, washed in 1X-PBS three times for 30 min per wash, and post-fixed with potassium-ferrocyanide reduced osmium tetroxide (1% OsO_4, 1.5% KFeCN) (Neiss, 1984). Samples were dehydrated in

graded alcohols (30%, 50%, 70%, 80%, 90%, 100% x 2) for 30 min each and processed for embedding in LR White resin (London Resin Company, Berkshire UK). Using a jeweler's saw, 2 mm width segments of maturation ameloblasts were cut at the alveolar crest, about 8 mm from the apical loop of the incisor (Smith and Nanci, 1989) just prior to eruption. The segment is then glued onto a resin stub and faced for semi-thin sections at 2 micrometer thickness using glass knives on a Reichert Jung Ultracut E ultra-microtome and stained with toluidine blue for initial assessment and orientation. Ultra-thin sections 80-100 nanometer thick were cut with a diamond knife, mounted on Formvar-carbon-coated 200 mesh nickel grids, and processed for post-embedding colloidal gold labeling.

Sample collection for TEM analysis required careful selection to obtain adequate images for analysis. For each genotype, 10-12 animals were initially perfused. Of those perfusions, 8-10 numbers were adequately fixed and were placed in decalcification solution for 30 days with a fresh solution change every 2-3 days. After decalcification, samples were embedded in LR White resin and cured. Resin blocks were cut, mounted, and faced. During facing, blocks with sections showing poor-quality morphologically or significant artifacts from processing were removed. The most common problem observed at this stage was collapse of the residual protein matrix in the *Klk4*-null and *Amtn*/*Klk4*-null samples, likely lost during the month-long decalcification procedure when the enamel mineral content was removed. When these sections were stained with

toluidine blue, it was common to observe small, discontinuous patches of retained protein matrix interspersed throughout the enamel layer. Specifically, only 2 *Amtn*/*Klk4*-null blocks and 1 *Klk4*-null block were adequately fixed and showed an intact enamel protein matrix. Many samples were deemed unsuitable for immunolabeling experiments. The analysis described below used 15 sections from the best-processed sample for each genotype.

Immunohistochemistry

As an antigen-retrieval step, ultrathin sections were first floated on a drop of 5% sodium metaperiodate for 1 h followed by washing in distilled water. Processing for immunolabeling proceeded as follows: grids were floated on a drop of 1X-PBS followed by 0.05M glycine, 1% ovalbumin, and 0.2% BSA-C in PBS (incubation buffer) for blocking non-specific binding. Grids were then transferred to rM179 amelogenin antibody (1:50 dilution in incubation buffer) for 1 h, washed in incubation buffer, and then incubated in Protein A-gold secondary antibody in incubation buffer (1:40 dilution). Finally grids were washed in incubation buffer, followed by 1X-PBS, and a final fixation step of 2% glutaraldehyde in PBS with subsequent washes in PBS and distilled water. Controls consisted of incubation with protein A-gold alone and incubation of sections obtained from amelogenin-null mice. Sections were then stained

with 7% aqueous uranyl acetate and lead citrate and examined in a Philips CM-100 transmission electron microscope (Philips, Amsterdam, Netherlands) operated at 80 kV.

Quantitative analysis of immunolabeling

Sequential, non-overlapping images of the outer enamel surface, just bordering the enamel-ameloblast interface were taken at a magnification of 19,000X, the lowest magnification at which 15 nm gold particles are clearly visible. For each incisor sample, three images were taken in the outer enamel area just bordering the enamel-ameloblast interface. The number of gold particles was calculated and an average labeling density was obtained.

RESULTS

Amelogenin composes the bulk of the secreted enamel matrix in the secretory stage of amelogenesis. Therefore, we used immunogold labeling to detect the presence of amelogenin in the outer region of the maturation stage enamel matrix to determine if there was any retained amelogenin when AMTN was absent. Ultrathin sections were taken from the incisor at the alveolar crest, just prior to eruption (about 8mm from the apical loop of the incisor). At this location ameloblasts are in the very late maturation stage and the enamel has not yet been in masticatory function.

Mature enamel at eruption is over 98% mineral by weight, and less than 2% water and protein (Weatherell, 1975; Young and Spooner, 1970). In wild-type animals, almost all of the protein that was secreted is removed at this developmental stage. In contrast, a significant amount of protein is visible in the *Amtn*/*Klk4*-null mouse (Fig. 6.1). To investigate if the lack of AMTN contributes to retained amelogenin in the outer enamel, a series of images from immunogold labeled slides were taken of the ameloblasts and the outer enamel region, as illustrated in Fig. 6.1.

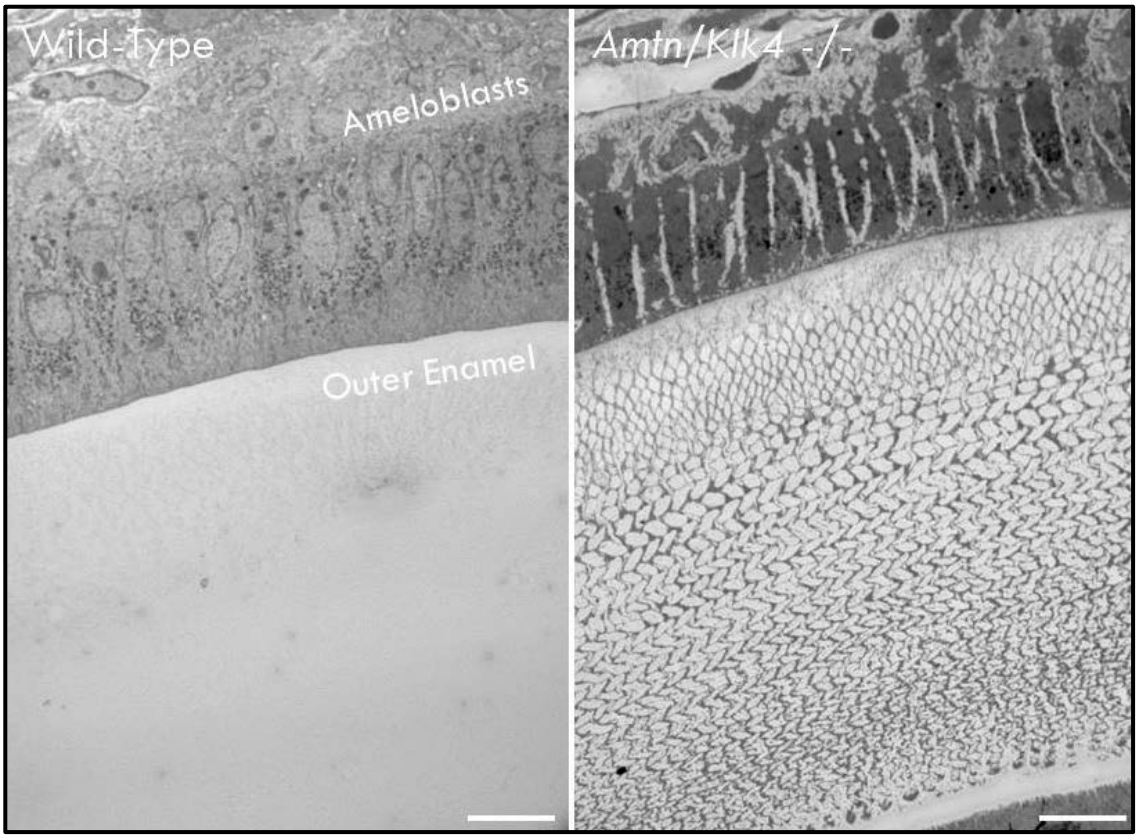

Fig. 6.1. Orientation of tissue sections. Incisor sections were taken at the alveolar crest, just prior to eruption (about 8 mm from the apical loop of the incisor). Ameloblasts are above and border the enamel, which is shown below. At this location ameloblasts are in the very late maturation stage. The location of image sampling, the outer enamel, is labeled in the image. In the wild-type mouse there is almost no remaining protein at this stage in amelogenesis. However, a significant amount of protein is visible in the *Amtn*/*Klk4*-null mouse. ***Left:*** section taken from wild-type incisor. ***Right:*** section taken from *Amtn*/*Klk4*-null incisor. Magnification: 1100X. Bar = 10 μm.

At this location, all ameloblasts are in the maturation stage and alternate between ruffled and smooth membranes (Fig. 6.2). Images of the outer enamel were taken at 19,000X magnification, which allowed for sampling of the largest area possible while still being able to see the gold particles for counting. Three non-overlapping images were taken for each genotype in the outer enamel near the ameloblasts at this magnification (Fig. 6.3). Similar images were taken from samples that were not incubated with the primary antibody. For those negative control samples, very minimal to no gold labeling was noted in the enamel (Fig. 6.4) and other areas of the samples (dentin, stellate reticulum, empty formvar, etc.).

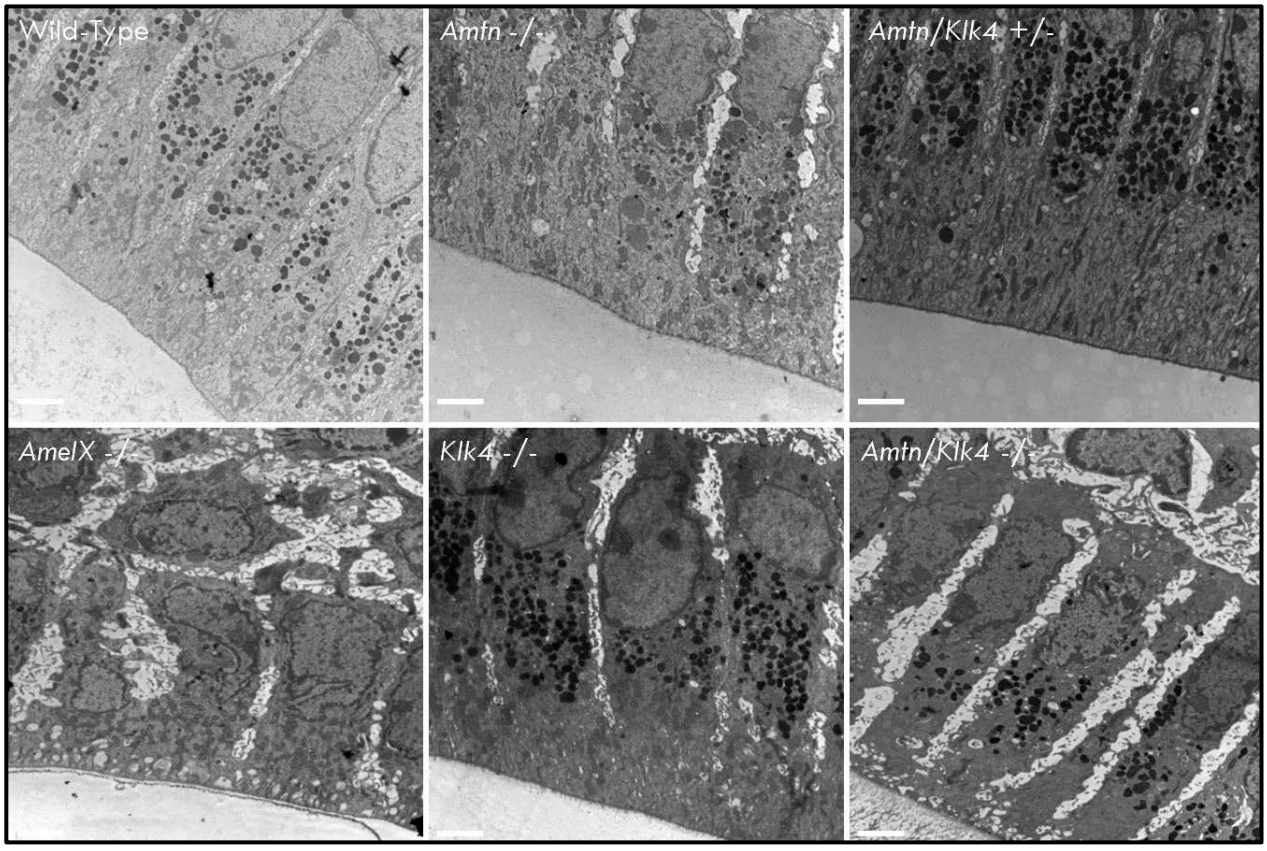

Fig. 6.2. Maturation stage ameloblasts. Maturation ameloblasts observed in sections taken at the level of the alveolar crest. Ameloblasts are above, bordering the outer enamel. Magnification: 4600X, Bar = 2 μm.

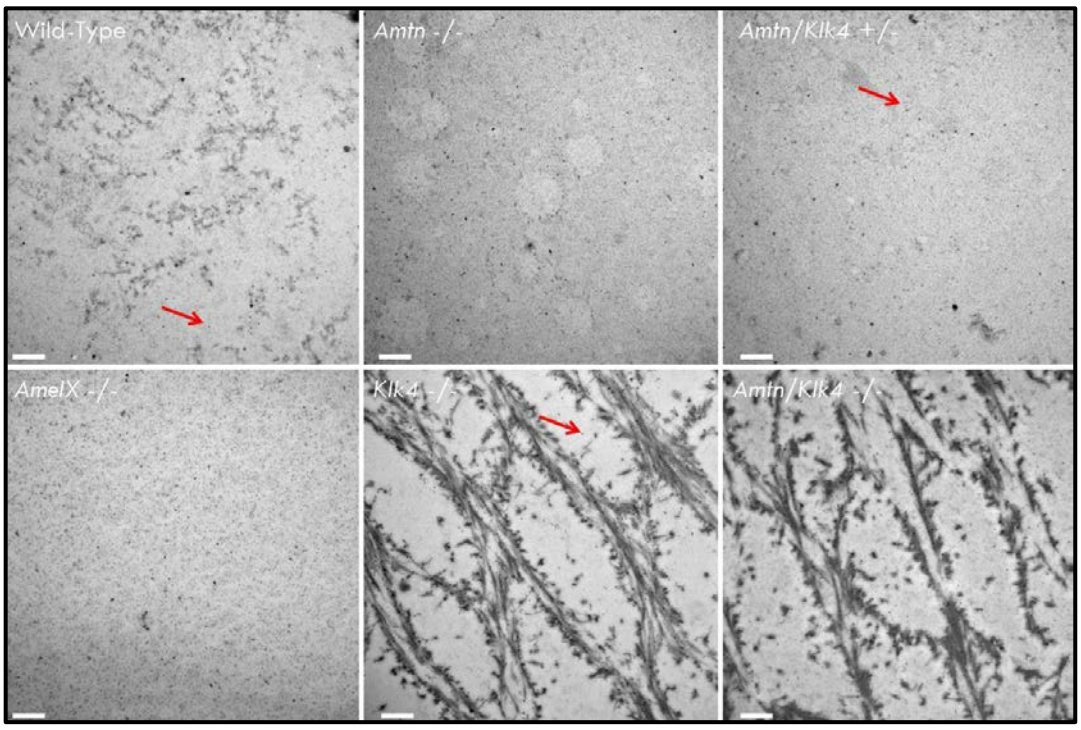

Fig. 6.3. Amelogenin (rM179) immunogold labeling of the outer enamel matrix. These are sequential, non-overlapping images of outer enamel matrix near the enamel-ameloblast interface. Red arrows show location of selected gold particles that were counted. Magnification: 19000X, Bar = 500 nm.

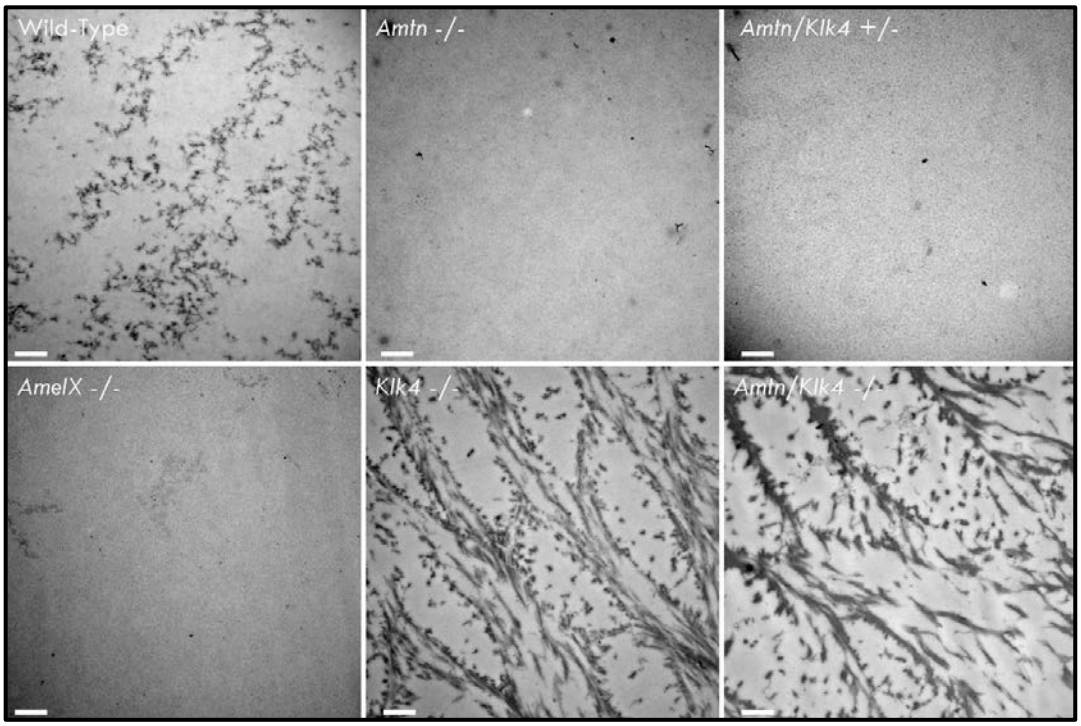

Fig. 6.4. Negative control images of outer enamel immunogold labeling. Sequential, non-overlapping images of the outer enamel matrix were taken in sections that were not incubated with rM179 antibody. Minimal to no labeling was seen. Magnification: 19000X, Bar = 500 nm.

Gold particles were counted in images taken from the outer enamel and averaged for each animal. *AmelX*-null mice were used to determine levels of background. Similar (low) immunogold counts were observed for the wild-type, *Amtn*-null, *Amtn*/*Klk4*-heterozygous, and *AmelX*-null mice (Fig. 6.5, *t*-test, $p>0.05$). No excess protein matrix was observed when AMTN was missing, and for all four genotypes the immunogold particle counts were low. In contrast, abundant immunolabeling was observed in the *Klk4*-null and *Amtn*/*Klk4*-null animals (*t*-test, $p<0.05$) showing that they had more retained amelogenin in the outer enamel matrix. The counts of immunogold particles were similar in *Klk4*-null and *Amtn*/*Klk4*-null sections (*t*-test, $p>0.05$).

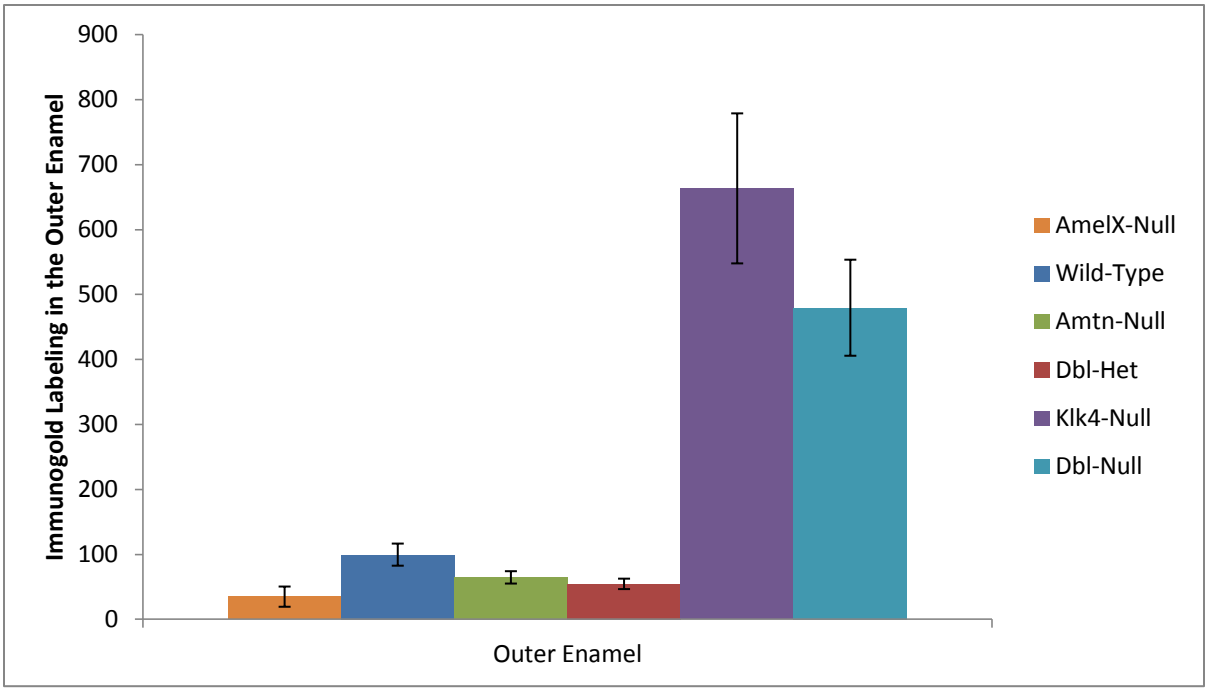

Fig. 6.5. Gold particle counts in the outer enamel by genotype. Gold particles were counted from sequential images of the outer enamel matrix. Background labeling was accounted for using the *AmelX*-null mouse (orange bar). Outer enamel counts were similar between the wild-type (dark blue), *Amtn*-null (green), and *Amtn*/*Klk4*-heterozygous (red) mice (*t*-test, $p>0.05$). While there was significantly more labeling in the *Klk4*-null (purple) and *Amtn*/*Klk4*-null (light blue) mice (*t*-test, $p<0.05$), the labeling density between those groups were similar (*t*-test, $p>0.05$).

DISCUSSION

Here we investigated differences in the density of retained amelogenin in the outer enamel when AMTN, KLK4, or both were missing. Since the enamel protein matrix is primarily composed of amelogenin, a primary antibody against recombinant protein (rM179) was used and labeled with gold-tagged secondary antibody. A series of images were taken of the outer enamel to determine gold labeling density. When we compared gold-particle counts in the outer enamel, no differences in residual amelogenin protein were observed between the wild-type, *Amtn*-null, and *Amtn*/*Klk4*-heterozygous mice. The counts in the outer enamel were similar to those observed for the *AmelX*-null mouse, which was used as a control for background levels of labeling.

In contrast, there was abundant amelogenin found in the outer enamel of both the *Klk4*-null and the *Amtn*/*Klk4*-null animals. However, it is highly likely that the high counts in the *Amtn*/*Klk4*-null animal are primarily a result of the lack of KLK4, especially since the *Amtn*-null mouse was similar to the wild-type mouse. It is therefore unlikely that AMTN is contributing to protein removal in the outer enamel matrix.

Given these findings, we conclude that while KLK4 is required for removal of protein in the outer matrix during the maturation stage. AMTN is not required for removal of protein and thus has a separate function from KLK4 in the outer enamel matrix during the maturation stage.

REFERENCES

Dos Santos Neves, J., Wazen, R.M., Kuroda, S., Francis Zalzal, S., Moffatt, P., and Nanci, A. (2012). Odontogenic ameloblast-associated and amelotin are novel basal lamina components. Histochem Cell Biol *137*, 329-338.

Faulk, W.P., and Taylor, G.M. (1971). An immunocolloid method for the electron microscope. Immunochemistry *8*, 1081-1083.

Kawasaki, K. (2013). Odontogenic ameloblast-associated protein (ODAM) and amelotin: Major players in hypermineralization of enamel and enameloid. J Oral Biosci *55*, 80-85.

Lacruz, R.S., Nakayama, Y., Holcroft, J., Nguyen, V., Somogyi-Ganss, E., Snead, M.L., White, S.N., Paine, M.L., and Ganss, B. (2012). Targeted overexpression of amelotin disrupts the microstructure of dental enamel. PLoS One *7*, e35200.

Moffatt, P., Smith, C.E., St-Arnaud, R., Simmons, D., Wright, J.T., and Nanci, A. (2006). Cloning of rat amelotin and localization of the protein to the basal lamina of maturation stage ameloblasts and junctional epithelium. Biochem J *399*, 37-46.

Nanci, A., McKee, M.D., and Smith, C.E. (1992). Immunolocalization of enamel proteins during amelogenesis in the cat. Anat Rec *233*, 335-349.

Nanci, A., Zalzal, S., and Kogaya, Y. (1993). Cytochemical characterization of basement membranes in the enamel organ of the rat incisor. Histochemistry *99*, 321-331.

Nanci, A., Zalzal, S., and Smith, C.E. (1987). Application of backscattered electron imaging and lectin-gold cytochemistry to visualize the distribution of glycoconjugates in a basal lamina. Scanning Microsc *1*, 1963-1970.

Neiss, W.F. (1984). Electron staining of the cell surface coat by osmium-low ferrocyanide. Histochemistry *80*, 231-242.

Nishio, C., Wazen, R., Moffatt, P., and Nanci, A. (2013). Expression of odontogenic ameloblast-associated and amelotin proteins in the junctional epithelium. Periodontol 2000 *63*, 59-66.

Orsini, G., Lavoie, P., Smith, C., and Nanci, A. (2001). Immunochemical characterization of a chicken egg yolk antibody to secretory forms of rat incisor amelogenin. J Histochem Cytochem *49*, 285-292.

Roth, J., Bendayan, M., and Orci, L. (1978). Ultrastructural localization of intracellular antigens by the use of protein A-gold complex. J Histochem Cytochem *26*, 1074-1081.

Roth, J., Bendayan, M., and Orci, L. (1980). FITC-protein A-gold complex for light and electron microscopic immunocytochemistry. J Histochem Cytochem *28*, 55-57.

Simmer, J.P., and Hu, J.C. (2001). Dental enamel formation and its impact on clinical dentistry. J Dent Educ *65*, 896-905.

Simmer, J.P., Lau, E.C., Hu, C.C., Aoba, T., Lacey, M., Nelson, D., Zeichner-David, M., Snead, M.L., Slavkin, H.C., and Fincham, A.G. (1994). Isolation and characterization of a mouse amelogenin expressed in Escherichia coli. Calcif Tissue Int *54*, 312-319.

Smith, C.E. (1998). Cellular and chemical events during enamel maturation. Crit Rev Oral Biol Med *9*, 128-161.

Smith, C.E., and Nanci, A. (1989). A method for sampling the stages of amelogenesis on mandibular rat incisors using the molars as a reference for dissection. Anat Rec *225*, 257-266.

Somogyi-Ganss, E., Nakayama, Y., Iwasaki, K., Nakano, Y., Stolf, D., McKee, M.D., and Ganss, B. (2012). Comparative temporospatial expression profiling of murine amelotin protein during amelogenesis. Cells Tissues Organs *195*, 535-549.

Weatherell, J.A. (1975). Composition of dental enamel. Br Med Bull *31*, 115-119.

Young, R.A., and Spooner, S. (1970). Neutron difraction studies of human tooth enamel. Arch Oral Biol *15*, 47-63.

Zalzal, S.F., Smith, C.E., and Nanci, A. (2008). Ameloblastin and amelogenin share a common secretory pathway and are co-secreted during enamel formation. Matrix Biol *27*, 352-359.

CHAPTER 7

CONCLUSION

SUMMARY

Optimal oral health is of primary importance for both nutrition and speech and requires the proper development of several dental tissues including enamel, dentin, cementum, and the periodontium. Oral health issues affect over 3.9 billion people worldwide, with untreated caries having the largest prevalence of all diseases (35%) for all ages combined (Marcenes et al., 2013). Some oral health issues include inherited dental defects such as oligodontia, dentinogenesis imperfecta, and amelogenesis imperfecta (AI). In particular, AI ranges in prevalence from 1:700 to 1:14,000 (Backman and Holm, 1986; Sundell and Koch, 1985) and leads to both primary and permanent dentition with malformed enamel (Witkop, 1957). This disease increases their susceptibility to caries and malocclusion and ultimately restoring patients to proper function is incredibly costly, time-consuming, and invasive (Hoods-Moonsammy et al., 2012; Savi et al., 2014). Unlike other tissues of the body, enamel is unable to repair itself, as ameloblasts, the cells responsible for enamel formation, become part of the reduced enamel epithelium that is lost following tooth eruption (Nishio et al., 2013). Therefore, understanding the

molecular genetic basis of tooth development, especially that of enamel formation, will foster a better understanding of the pathology involved in AI and allow for the development of better restorative options that would help improve the public health burden caused by dental caries.

Enamel is formed primarily through two distinct stages: the secretory stage where the full thickness of enamel is established and the maturation stage where the enamel layer reaches its final hardness (Hu et al., 2007; Simmer et al., 2010; Smith, 1998). In both of these stages, ameloblasts secrete a highly specific protein matrix that is required for the deposition of calcium and phosphate ions into hydroxyapatite, so when components of this extracellular protein matrix are missing or non-functional, it leads to aberrations in enamel formation (Bartlett, 2013). To date, only about half of AI cases that are analyzed through mutational analyses have a known genetic etiology with the largest percentage of AI cases being accounted for by FAM83H (Kim et al., 2006; Wright et al., 2011). This suggests that there are other participants involved in amelogenesis that are as of yet unknown.

In this thesis, we focused on protein components specific to the maturation stage of amelogenesis, specifically the recently discovered protein AMTN, the serine protease KLK4, and how these two proteins might potentially facilitate the final steps of enamel mineralization. By using a series of knockout mice (wild-type, *Amtn*-null, *Klk4*-null, *Amtn*/*Klk4*-heterozygote, and *Amtn*/*Klk4*-null) we studied enamel structural defects and

the retention of enamel protein matrix. These mouse models were described in Chapter 2. Compared to wild-type mice, the *Amtn*-null phenotype consists primarily of chalky discoloration of the enamel layer with occasional chipping of the incisal edge at 7 weeks of age. On gross observation of the mandibular incisor, the *Klk4*-null and the *Amtn*/*Klk4*-null mice are indistinguishable from each other and both exhibit a chalky-white enamel layer with significant chipping and wear of the incisal edge. Given the more mild phenotype observed in the *Amtn*-null mice, the bulk of the phenotype in the *Amtn*/*Klk4*-null mice is due to the missing KLK4 protease.

To gain insight into ultrastructural changes that occur in the enamel when AMTN is missing, we used scanning electron microscopy (SEM) and backscatter electron imaging (BEI) to study the thickness, rod decussation pattern, and the mineral density of the enamel layer, which was described in Chapter 3. When incisors were fractured at the alveolar crest and processed for SEM imaging, all five groups of mice showed a normal rod decussation pattern and no difference in enamel thickness, which suggests that the secretory stage is unaffected. This is consistent with AMTN and KLK4 being expressed in the maturation stage of amelogenesis. The enamel of *Klk4*-null and *Amtn*/*Klk4*-null animals tended to fracture near the DEJ and the enamel rods were less closely packed than in wild-type animals, but these two groups were indistinguishable from each other. Again, these defects are consistent with aberrations in the maturation stage rather than the secretory stage. Enamel mineralization was compared between

groups using BEI. This technique, which analyzes mineral density, was unable to distinguish between wild-type, *Amtn*-null, and *Amtn*/*Klk4*-null heterozygote animals. While *Klk4*-null and *Amtn*/*Klk4*-null mice had significantly less mineralized enamel, they were likewise difficult to distinguish using this technique. In addition, when the thickness of the enamel layer was measured, there was no difference between groups suggesting that the secretory stage is unaffected. The observed defects in mineralization in the *Klk4*-null and *Amtn*/*Klk4*-null were also consistent with defects in the maturation stage of amelogenesis. This data taken as a whole suggests that AMTN plays a smaller role than KLK4 in the final mineralization of the enamel layer and that lack of AMTN does not change the mineral density of the enamel layer.

As a quantitative method of measuring enamel mineral density, in Chapter 4 we describe the use of microCT analysis with known-density phantoms to analyze the different groups of mice. Similar to the BEI analysis, no difference in mineral density was observed between the wild-type and *Amtn*-null mice. Likewise, the *Klk4*-null and *Amtn*/*Klk4*-null mice were similar. However, when we analyzed the MIP images, we observed that when AMTN is missing the onset of maturation is delayed which may explain why the outer enamel does not reach its final hardness prior to eruption.

In Chapter 5, we used Knoop microhardness testing to assess differences in the hardness of the enamel layer. Indentations were placed in the outer, middle, and inner enamel as well as the dentin of incisors sectioned at the level of the alveolar crest. Using

this technique, we found that when AMTN is absent, the primary area that is affected is the outer 15 micrometers of enamel near the surface. In the outer enamel, the *Amtn*-null group had a Knoop hardness value of 249.8 ± 45.6, which was significantly softer compared to the wild-type group value of 327.1 ± 19.8 (*t*-test, $p<0.001$). Similarly, at that same location the *Amtn*/*Klk4*-null group had a significantly softer value of 141.4 ± 26.8 than the *Klk4*-null group value of 201.0 ±26.6 (*t*-test, $p<0.001$). No difference was found between *Amtn*/*Klk4*-heterozygote and wild-type mice, suggesting that there is no defect in the heterozygote condition.

Since the hardness of the outer enamel is affected when AMTN is missing, but BEI was unable to show a change in mineral density, we described in Chapter 6 if there was any retained protein matrix in the outer enamel by using a gold-labeled antibody against amelogenin (rM179), which consists of most of the extracellular matrix in developing enamel (Simmer and Hu, 2001). A series of images were taken of the outer enamel from sections sampled at the alveolar crest of wild-type, *Amtn*-null, *Klk4*-null, *Amtn*/*Klk4*-heterozygous, and *Amtn*/*Klk4*-null mice. *AmelX*-null mice were used to determine levels of background labeling. No significant difference in gold labeling was observed between the wild-type, *Amtn*-null, *Amtn*/*Klk4*-heterozygous, and *AmelX*-null mice. While we observed significantly more gold particles in the *Klk4*-null and *Amtn*/*Klk4*-null mice, these two groups were similar to each other. We concluded that AMTN is not involved in protein removal of the outer enamel layer.

In summary, AMTN and KLK4 are maturation stage proteins that are both required for optimal maturation of the outer enamel layer, and neither protein is involved in the secretory stage. KLK4 is a secreted serine protease that is required for removal of the protein matrix in the maturation stage. AMTN is a secreted protein that is related to the SCPP family, localizes to the basal lamina, and is responsible for allowing the outer 15 micrometers of enamel to reach its final hardness. Lack of AMTN and KLK4 does not affect enamel thickness or rod organization, again showing that both are involved in the maturation stage and neither is involved in the secretory stage. When KLK4 is missing, significant amounts of retained protein are observed in the enamel layer. When AMTN is missing, on the other hand, no significant amount of protein is observed in the outer enamel. In addition, lack of AMTN results in a delay of the onset of the early maturation stage. Since lack of AMTN does not result in more retained protein matrix in the outer enamel, and the mineral density appears to be the same as that in wild-type, it is possible that AMTN may be affecting the physical structure of the hydroxyapatite in the outer enamel layer, or the chemical composition of the enamel (increased carbonated apatite rather than hydroxyapatite). This is consistent with the fact that AMTN is part of the SCPP family, a group of proteins that contained a phosphorylated serine that allows them to interact with calcium ions.

FUTURE DIRECTIONS

During this investigation we made several important discoveries that should be followed up to gain further insights into AMTN function. First, our μCT analyses determined that the increase in mineralization that is associated with the onset of enamel maturation is delayed in the *Amtn*-null mouse. This delay could be due to a particularly important function of AMTN at the onset of the maturation stage. We also found that enamel layers with the same mineral density may show significant differences in enamel hardness. Better information about AMTN's role in enamel formation could be learned by performing hardness analyses on enamel cross sections starting in late secretory stage and continuing at 1 mm increments until eruption. This would provide a time course for enamel hardening that could determine if AMTN function is important just at the onset, or if it is important throughout enamel maturation.

The primary question that this study highlights is how the lack of AMTN produces a delay in maturation and softer outer enamel without affecting the mineral density of the outer enamel. A technique that was not used in this study, but might provide further information on the function of AMTN in enamel mineralization, is laser Raman spectroscopy. This technique allows for a quantitative, molecular analysis of the enamel layer, providing information such as the proportion of carbonated apatite versus hydroxyapatite. It would also be possible to use X-ray diffraction and infrared

spectroscopy to determine if the *Amtn*-null mice have a significant increase in the presence of carbonated apatite in the outer enamel layer, or if there is a change in the organization of the traditional hydroxyapatite unit cell in the outer enamel layer. Both of these changes would contribute to a softer enamel structure. Further explorations of the chemical changes that occur may help explain the function of AMTN in the maturation stage of amelogenesis.

REFERENCES

Backman, B., and Holm, A.K. (1986). Amelogenesis imperfecta: prevalence and incidence in a northern Swedish county. Community Dent Oral Epidemiol *14*, 43-47.

Bartlett, J.D. (2013). Dental Enamel Development: Proteinases and Their Enamel Matrix Substrates. ISRN Dent *2013*, 684607.

Hoods-Moonsammy, V.J., Mothopi, M.M., Taruvingira, A.K., Owen, C.P., and Howes, D.G. (2012). Prosthodontic management of patients with amelogenesis imperfecta. SADJ *67*, 409-412.

Hu, J.C., Chun, Y.H., Al Hazzazzi, T., and Simmer, J.P. (2007). Enamel formation and amelogenesis imperfecta. Cells Tissues Organs *186*, 78-85.

Kim, J.W., Simmer, J.P., Lin, B.P., Seymen, F., Bartlett, J.D., and Hu, J.C. (2006). Mutational analysis of candidate genes in 24 amelogenesis imperfecta families. Eur J Oral Sci *114 Suppl 1*, 3-12; discussion 39-41, 379.

Marcenes, W., Kassebaum, N.J., Bernabe, E., Flaxman, A., Naghavi, M., Lopez, A., and Murray, C.J. (2013). Global burden of oral conditions in 1990-2010: a systematic analysis. J Dent Res *92*, 592-597.

Nishio, C., Wazen, R., Moffatt, P., and Nanci, A. (2013). Expression of odontogenic ameloblast-associated and amelotin proteins in the junctional epithelium. Periodontol 2000 *63*, 59-66.

Savi, A., Turillazzi, O., Crescini, A., and Manfredi, M. (2014). Esthetic Treatment of a Diffuse Amelogenesis Imperfecta Using Pressed Lithium Disilicate and Feldspathic Ceramic Restorations: 5-Year Follow Up. J Esthet Restor Dent.

Simmer, J.P., and Hu, J.C. (2001). Dental enamel formation and its impact on clinical dentistry. J Dent Educ *65*, 896-905.

Simmer, J.P., Papagerakis, P., Smith, C.E., Fisher, D.C., Rountrey, A.N., Zheng, L., and Hu, J.C. (2010). Regulation of dental enamel shape and hardness. J Dent Res *89*, 1024-1038.

Smith, C.E. (1998). Cellular and chemical events during enamel maturation. Crit Rev Oral Biol Med *9*, 128-161.

Sundell, S., and Koch, G. (1985). Hereditary amelogenesis imperfecta. I. Epidemiology and clinical classification in a Swedish child population. Swed Dent J *9*, 157-169.

Witkop, C.J. (1957). Hereditary defects in enamel and dentin. Acta Genet Stat Med *7*, 236-239.

Wright, J.T., Torain, M., Long, K., Seow, K., Crawford, P., Aldred, M.J., Hart, P.S., and Hart, T.C. (2011). Amelogenesis imperfecta: genotype-phenotype studies in 71 families. Cells Tissues Organs *194*, 279-283.